To the Graduate Council:

I am submitting herewith a dissertation written by Hye Jung Kang entitled "Neutron scattering studies on magnetism and phonon in the electron-doped $Nd_{2-x}Ce_xCuO_4$ and $Pr_{1-x}LaCe_xCuO_4$." I have examined the final electronic copy of this dissertation for form and content and recommend that it be accepted in partial fulfillment of the requirements for the degree of Doctor of Philosophy, with a major in Physics.

Pengcheng Dai
Major Professor

We have read this dissertation
and recommend its acceptance:

Janice L. Musfeldt

James R. Thompson

Victor Barzykin

David G. Mandrus

Acceptance for the Council:

Anne Mayhew
Vice Chancellor and Dean of
Graduate Studies

(Original signatures are on file with official student records.)

Neutron scattering studies on magnetism and phonon in the electron-doped $Nd_{2-x}Ce_xCuO_4$ and $Pr_{1-x}LaCe_xCuO_4$

A Dissertation
Presented for the
Doctor of Philosophy
Degree
The University of Tennessee, Knoxville

Hye Jung Kang

May 2005

Dedication

This dissertation is dedicated to my husband Joe, my parents, and in-laws. They have been my good friends who are always inspiring me, and encouraging me to give me support.

Acknowledgements

I would like to thank my advisor, Dr. Pengcheng Dai, who has provided many great opportunities for my research. Dr. Dai taught me a lot of skills necessary for using neutron scattering technique, a very useful tool for my work. Due to his patience and guidance, I was able to gather the knowledge required to achieve our goals. He also provided me with the opportunity to attend conferences and meetings where I can present our work and broaden my experience.

I am grateful to have Dr. Thompson, Dr. Mandrus, Dr. Barzykin, and Dr. Musfeldt for my committee. My discussions with them made significant contribution to my understanding of physics and the completion of my work.

I appreciate my collaborators Dr. Lynn and Dr. Lee from NIST, Dr. Mook and Dr. Matsuura from ORNL, and Dr. Argyriou from HMI for all their help in this work. I also thank Dr. Tokura and his group, Dr. Ando and his group, and Dr. Mandrus and Dr. R. Jin for providing excellent samples for us.

I send my thanks to many scientist and technicians at ORNL, NIST, HMI, and ISIS for their assistance. And I would also like to say thanks to Randy at UT for making a lot of sample holders for me.

This work is supported by U.S. NSF DMR-0139882 and the U.S. DOE under Contract No. DE-AC05-00OR22725 with UT-Battelle, LLC.

Abstract

We present comprehensive neutron scattering studies on the electron-doped superconductors $Nd_{2-x}Ce_xCuO_4$ and $Pr_{1-x}LaCe_xCuO_4$ to understand how magnetic properties and phonon are related to superconductivity. For superconducting $Nd_{1.85}Ce_{0.15}CuO_4$, a *c*-axis magnetic field enhances the commensurate antiferromagnetic order, while an *ab*-plane magnetic field induces spin-flop transition from a noncollinear to a collinear magnetic structure. The *c*-axis field-induced effect is absent in both the parent Nd_2CuO_4 and the as-grown nonsuperconducting $Nd_{1.85}Ce_{0.15}CuO_4$ samples. These results, combined with those on the hole-doped $La_{2-x}Sr_xCuO_4$ suggest that the antiferromagnetism competes with superconductivity.

In the $Pr_{1-x}LaCe_xCuO_4$ system, we find that quasi-2 dimensional commensurate antiferromagnetism coexists with superconductivity and 3 dimensional antiferromagnetism. To determine whether the antiferromagnetic order is the competing order in the high temperature superconductors, regardless of hole-doping or electron-doping, we performed field-induced experiments on the electron-doped superconductor $Pr_{0.88}LaCe_{0.12}CuO_{4\pm\delta}$ by applying magnetic fields along the *c*-direction and in the *ab*-plane direction. The anisotropy of the field-induced moment demonstrates the competing nature of these two order parameters.

We find that the spin-flop transition induced by an *ab*-plane magnetic field in the lightly electron-doped $Pr_{1.29}La_{0.7}Ce_{0.01}CuO_4$ affects significantly both in-plane and out-of-plane resistivity. No magnetoresistance anomaly is observed when a *c*-axis magnetic field is applied, consistent with the absence of a spin-flop transition for such field direction. This anisotropic magnetoresistance effect suggests that there is spin-charge coupling in the electron-doped superconductors as well as in the hole-doped ones.

Inelastic neutron scattering has been performed to study the generalized phonon density of states (GDOS) of electron-doped $Nd_{2-x}Ce_xCuO_4$ with various levels of doping. Upon doping,

the softening of phonon around 70 meV has been observed. However, most of the softening occurs within a few percent of Ce doping, and it is not related to the doping induced nonsuperconducting-superconducting transition. Therefore, the electron-lattice coupling in the electron-doped $Nd_{2-x}Ce_xCuO_4$ is different from that in the hole-doped materials.

Table of contents

List of tables

Chapter 2

Chapter 3

List of figures

Chapter 1

Chapter 2

Chapter 3

Chapter 4

Chapter 5

Chapter 1: Introduction

1.1 History of superconductors

Superconductors are one of the most fascinating materials in the world of scientific discovery. A superconductor is matter in a state where the electrical current can flow without resistance below a certain temperature (superconducting transition temperature T_c). This phenomenon was first observed by Kamerlingh Onnes in 1911 while he was investigating the electrical resistivity of mercury at extremely cold temperatures [1]. He observed that the resistance of a mercury wire vanished, when it was cooled to the temperature of liquid helium (4.2 K).

In the beginning, most superconductors were discovered in metals and intermetallic compounds. This is because the resistance of metals decreases with decreasing temperature. Meissner and Ochsenfeld discovered a dramatic magnetic property in superconductors in 1933 [2]. They observed that the magnetic flux was completely expelled from a superconducting material until it reached a critical field (B_c), the so-called Meissner effect. These materials are categorized as type-I superconductors. The origin of superconductivity in these materials is explained well by the BCS theory [3]. The central idea in the BCS theory is a Cooper pair. The Cooper pair contains two loosely paired electrons with opposite momentum. Since these pairs with spin zero can be considered as bosons, they can condense into a single quantum state resulting in superconductivity. The attractive interaction between two electrons required to overcome Coulomb repulsion is mediated by lattice vibration, “phonon”. The phonon-mediated superconductors have low transition temperature T_c, and the maximum T_c is thought to be around 30 K. In conventional low temperature superconductors, the electrons pair to have zero angular momentum (s-wave state), therefore superconductivity is isotropic.

The discovery of high transition temperature (high-T_c) superconductors in 1986 was a breakthrough in the field of superconductivity. Bednorz and Müller discovered the superconductors in La-Ba-Cu-O system with highest onset T_c = 30 K [4]. One of the striking features is the fact that these ceramic compounds are normally insulators; therefore they were not considered as possible candidates for superconductors. The discovery of superconductivity in ceramic compounds spurred many scientists to find new types of superconductors. Soon another superconductor was discovered in Y-Ba-Cu-O system with higher T_c = 93 K above the temperature of liquid nitrogen [5]. This discovery received much attention from the public, as well as physics community, because of its possible practical applications. Currently the highest T_c is 133 K in Hg-Ba-Ca-Cu-O system and T_c can reach up to 160 K with pressure [6].

A lot of high-T_c superconductors have been discovered in many families of ceramics since 1986. However, in spite of a great number of materials, all have a few features in common. First, all of them have 2 dimensional (2D) CuO_2 planes. Because of this, they are called cuprates and the term high-T_c superconductivity is reserved for these cuprates. These CuO_2 planes are connected with block layers as shown in Fig. 1.1(a). The charge transport measurement shows that charges are confined in the CuO_2 plane, and the coherent charge transport between planes is blocked. As expected, the superconductivity in all high-T_c cuprates is highly anisotropic, being much stronger within the CuO_2 planes than perpendicular to the planes. Superconductivity can be achieved when the CuO_2 planes are doped with holes or electrons. Second, all of the parent compounds are half-filled antiferromagnetic Mott insulators because of strong on-site Coulomb repulsion between electrons (Fig. 1.1(b)). Last, all high-T_c cuprates are type-II superconductors, which can expel completely the magnetic flux below a lower critical field (B_{c1}) and can partially expel the magnetic flux up to an upper critical field (B_{c2}). In the region between B_{c1} and B_{c2} the magnetic flux can penetrate as flux lines (vortices) threaded in the superconductor allowing superconductivity and magnetism to coexist.

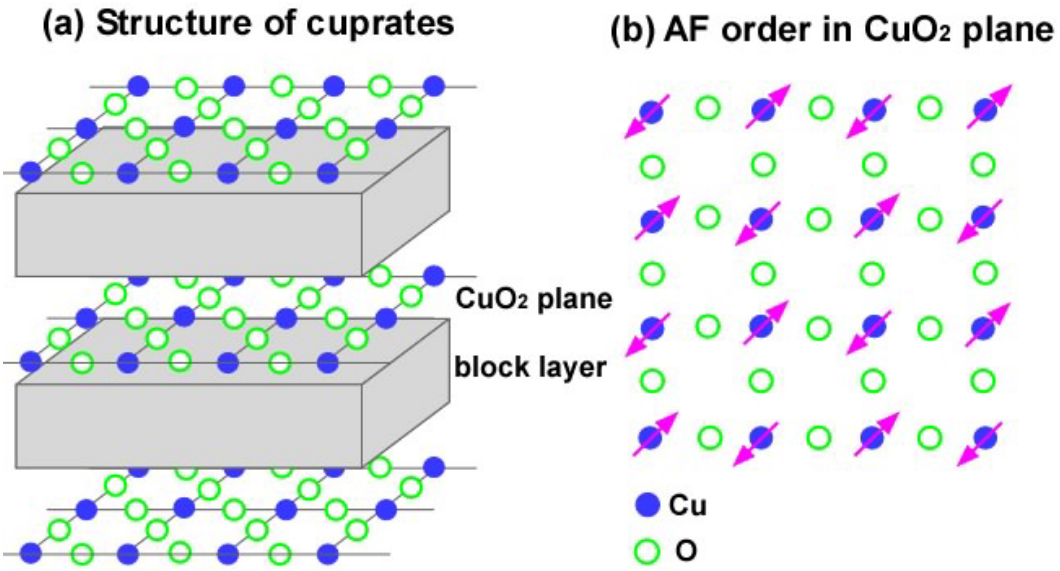

Fig. 1.1 The common structure of high-T_c cuprates and spin arrangement in the CuO_2 plane. (a) The 2D CuO_2 planes are coupled by block layers, which give charges to the CuO_2 planes when the system is doped. All high-T_c cuprates have the CuO_2 planes. (b) Each Cu^{2+} ion has one electron of spin ½ on its lattice site because of strong on-site Coulomb interaction. The spins of Cu^{2+} order antiferromagnetically below certain temperature. When charges are doped into this CuO_2 planes, this antiferromagnetic order is destroyed and the system becomes metallic.

The discovery of high-T_c superconductivity has created one of the biggest challenges in condensed matter physics. A lot of effort has been made to understand the mechanism of high-T_c superconductivity. However, there is little consensus. It is accepted that in high-T_c superconductors electrons form Cooper pairs by overcoming the Coulomb repulsive force. The phonon-mediated pairing mechanism by itself does not explain high-T_c superconductivity. The T_c is too high to arise from electron-phonon coupling only. Then what is responsible for a pairing that would allow such a high transition temperature? Is it magnetic attraction, still phonons, or something else? Almost 20 years after the discovery of high-T_c superconductors, we still do not have an answer to this question. There are too many experimental results on a wide variety of samples. And there are many theories explaining these results.

The main purpose of my research is to search for the most fundamental phenomena that can be responsible for high-T_c superconductivity. For this, it is better to start with the simplest samples, because the underling physics must exist in all of the cuprates regardless of their structures. The ideal examples are single layer crystal structure compounds $La_{2-x}Sr_xCuO_4$ for hole-doped superconductor, $Nd_{2-x}Ce_xCuO_4$ and $Pr_{1-x}LaCe_xCuO_4$ for electron-doped ones. The crystal structures of these materials are shown in Fig. 1.2.

Magnetism is one of the strong candidates believed to play an important role in the mechanism of superconductivity in high-T_c superconductors. This is mainly because superconductivity in all of the cuprates is achieved by doping a small amount of holes or electrons into antiferromagnetic insulators. The magnetic properties in hole-doped $La_{2-x}Sr_xCuO_4$ have been studied extensively. Neutron scattering experiments show some interesting features in this material. When the parent compound La_2CuO_4 is doped with Sr^{2+}, the 3D antiferromagnetic order is dramatically destroyed and replaced by spin-glass regime in range $0.02 < x < 0.05$. The superconductivity dome appears in range $0.05 < x < 0.3$ [7]. Recent elastic neutron scattering experiments on $La_{2-x}Sr_xCuO_4$ show that two incommensurate magnetic peaks coexist with the

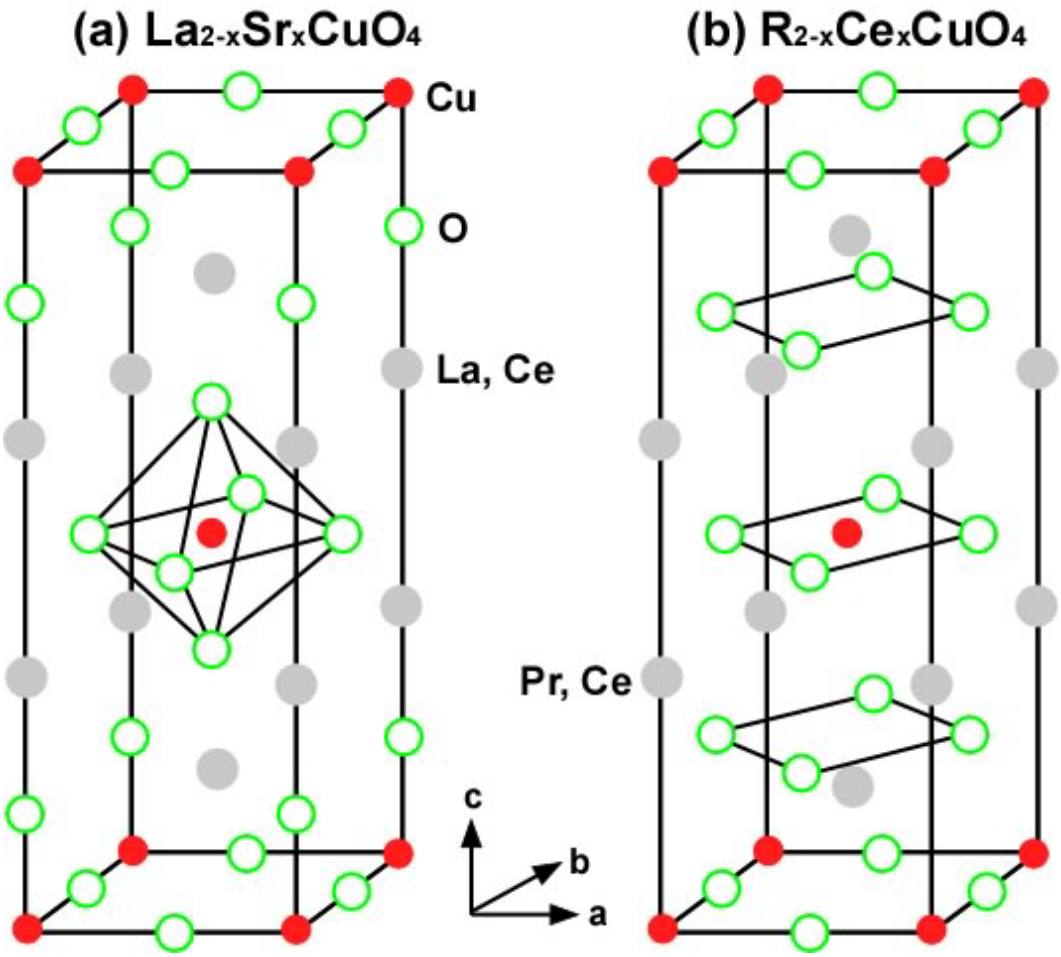

Fig. 1.2 Crystal structures of single layer high-T_c families. (a) Hole-doped $La_{2-x}Sr_xCuO_4$ has orthorhombic T structure at low temperature, which each Cu ion is surrounded by an octahedron of oxygen. The oxygen atoms above and below Cu ion are called apical oxygen. (b) Electron-doped $R_{2-x}Ce_xCuO_4$ (R = Nd or Pr) has a tetragonal T´ structure, where apical oxygen ions are absent.

3D antiferromagnetic order in the lightly doped region and survive in the insulating phase with Sr^{2+} doping [8, 9, 10, 11]. These peaks correspond to 1D spin density wave along the diagonal direction (Cu-Cu direction). At the transition to a superconducting phase, an additional two pairs of magnetic peaks appear with their direction parallel to the Cu-O direction and coexist with superconductivity in the underdoped regime [11, 12, 13]. These spin density waves disappear in the optimally doped superconductors [12]. And, it's the optimally doped superconductors that have the highest T_c.

Lake *et al.* conducted an experiment using $La_{2-x}Sr_xCuO_4$ to look at the magnetic field effect [14]. In this experiment, the *c*-axis magnetic field enhanced the spin density wave below the T_c of a zero-magnetic field in the underdoped region. This result seems to suggest that the spin density wave may be a competing ground state to superconductivity. The magnetic field effect on optimally doped $La_{2-x}Sr_xCuO_4$ does not induce the spin density wave; instead it enhances incommensurate spin fluctuations [15].

The interplay between the competing phases has been one of the important issues in solving the pairing mechanism of high-T_c superconductivity since the observation of enhancement of the spin density wave in hole-doped $La_{2-x}Sr_xCuO_4$. One of the theories, SO(5), is based on the existence of these two competing phases [16, 17].

Therefore, an investigation of electron-doped superconductors is required to prove or disprove this possibility. I focused on the magnetic properties of the electron-doped superconductors $Nd_{2-x}Ce_xCuO_4$ and $Pr_{1-x}LaCe_xCuO_4$. I wanted to find the similar and different properties when compared to hole-doped superconductors.

Even though a lot of studies on high-T_c superconductors have been focused on magnetism, the role of phonons cannot be ignored as a possible pairing mechanism. The key evidence for electron-lattice coupling is a sudden change of electron velocity at energies around 50~80 meV as seen in the electronic dispersion of the hole-doped $Bi_2Sr_2CaCu_2O_8$ (Bi2212), Pb-

doped Bi2212 (Pb-Bi2212), Pb-doped $Bi_2Sr_2CuO_6$ (Pb-doped Bi2201), and $La_{2-x}Sr_xCuO_4$ from the angle resolved photoemission spectroscopy (ARPES) measurements [18]. Since this excitation energy range (50~80 meV) is very different from the gap energies of these materials, the superconducting gap origin is ruled out. However, this energy range is very close to the in-plane oxygen-half breathing phonon mode of ~70 meV in $La_{2-x}Sr_xCuO_4$ observed in inelastic neutron scattering experiment [19]. This lattice vibration also develops near the doping-induced metal-insulator transition in the generalized phonon density of states of $La_{2-x}Sr_xCuO_4$.

In the case of the electron-doped superconductor $Nd_{1.85}Ce_{0.15}CuO_4$, this sudden change of electron velocity in dispersion curve is not observed [20]. Therefore, the authors suggest much weaker electron-lattice coupling in electron-doped superconductors. These experimental results made us wonder if the phonon density of states is related to the nonsuperconducting to superconducting transition. Consequently, we performed inelastic neutron scattering on $Nd_{2-x}Ce_xCuO_4$ powders with different doping levels that ranged from an undoped insulator to optimally doped superconductors (x = 0.15).

In this dissertation I will describe my research, focusing on the roles of magnetism and phonons in high-T_c superconductivity using neutron scattering techniques. This dissertation is organized as follows. Chapter 1 has the introduction and neutron scattering theories. Chapter 2 describes magnetic field effects on electron-doped $Nd_{1.85}Ce_{0.15}CuO_4$. Chapter 3 shows the evolution of magnetism and superconductivity in the phase diagram of $Pr_{1-x}LaCe_xCuO_4$ and their magnetic field effect. Chapter 4 describes spin-charge coupling in lightly doped $Pr_{1.29}LaCe_{0.01}CuO_4$. Chapter 5 concerns the role of phonons in $Nd_{2-x}Ce_xCuO_4$ as a function of doping level. Chapter 6 is the conclusion.

1.2 Neutron scattering technique

The neutron scattering technique is one of the most invaluable and ideal microscopic probes in condensed matter. This is due to several unique properties of a neutron. First, the relatively large mass of a neutron allows thermal neutrons of energy range 5 to 100 meV to have a wavelength of 1 to 3 Å, which is comparable to an atomic spacing in solids. The energy of thermal neutrons is of the same order of many excitations in solids, allowing studying dynamical phenomena in solids using inelastic scattering. Second, a neutron can penetrate deeply into the bulk and come close to the nuclei, since it has zero charge. Third, it has a magnetic moment. This means that neutrons interact with the unpaired electrons in magnetic atoms. This property is perfect for the research of magnetic structure and dynamics in high-T_c cuprates. Elastic scattering from this interaction gives information on the arrangement of electron spins and the density distribution of unpaired electrons. Inelastic magnetic scattering gives the energies of magnetic excitations.

Below is a brief summary of neutron scattering theories [21, 22, 23]. The two basic laws of momentum and energy conservation govern scattering experiments.

$$\vec{Q} = \vec{k}_f - \vec{k}_i \qquad \text{momentum conservation} \qquad (1\text{-}1)$$

$$\hbar\omega = E_i - E_f = \frac{\hbar^2}{2m_n}(k_i^2 - k_f^2) \quad \text{energy conservation} \qquad (1\text{-}2)$$

The subscripts *i* and *f* refer to incident and final neutron, respectively. The magnitude of wave vector $k = 2\pi / \lambda$, where λ is the neutron wavelength of the neutron, and m_n is the mass of neutron.

In neutron scattering, we measure the number of neutron scattered per second into a given solid angle $d\Omega_f$, in the direction of the wave vector k_f, with a final energy between E_f and $E_f + dE_f$. This is given by the partial differential cross section, $d^2\sigma/d\Omega_f dE_f$. It is expressed as a sum of coherent and incoherent parts. The coherent part provides information about the cooperative effects among different atoms, such as elastic Bragg scattering or inelastic scattering by phonons

or magnons, while the incoherent part is proportional to the time correlation of an atom with itself and provides information about individual particle motion.

The partial differential cross section due to magnetic interaction V_m for unpolarized neutrons is given by

$$\frac{d^2\sigma}{d\Omega_f dE_f} = \frac{k_f}{k_i}\left(\frac{m_n}{2\pi\hbar^2}\right)^2 |<\vec{k}_f\sigma_f \mid \mathrm{V_m} \mid \vec{k}_i\sigma_i>|^2 \ \delta(\hbar\omega + E_i - E_f) \qquad (1\text{-}3)$$

The interaction between the neutron and an unpaired electron is written as

$$\mathrm{V_m}(\vec{\mathrm{r}}) = -\vec{\mu}_n \cdot \vec{B}(\vec{\mathrm{r}}) \qquad (1\text{-}4)$$

Here $\vec{\mu}_n$ is the magnetic dipole moment of the neutron and $\vec{B}(\vec{\mathrm{r}})$ is the magnetic field due to the magnetic dipole moment of an unpaired electron. Magnetic field due to the magnetic dipole moment of an electron is written as

$$\vec{\mathrm{B}}(\vec{\mathrm{r}}) = \vec{\nabla}\times\vec{\mathrm{A}} = \vec{\nabla}\times\frac{\vec{\mu}_e\times\hat{\mathrm{r}}}{\mathrm{r}^2} \qquad (1\text{-}5)$$

, where $\vec{\mu}_e$ is the magnetic dipole moment of an electron. By using these expressions, the partial differential cross section of localized spins (1-3) can be expressed as

$$\frac{d^2\sigma}{d\Omega_f dE_f} = \frac{k_f}{k_i} p^2 f^2(\vec{\mathrm{Q}}) e^{-2W} \sum_{\alpha,\beta}(\delta_{\alpha,\beta} - \hat{Q}_\alpha\hat{Q}_\beta) S^{\alpha\beta}(\vec{\mathrm{Q}},\omega), \quad p = \frac{\gamma e^2}{2m_e c^2} \qquad (1\text{-}6)$$

where α, β = x, y, z, and $f(\vec{\mathrm{Q}})$ is the magnetic form factor, which is the Fourier transform of the spin density. p is the neutron-electron coupling constant, e^{-2W} is Debye-Waller factor and the scattering function $S^{\alpha\beta}(\vec{\mathrm{Q}},\omega)$ is defined as

$$S^{\alpha\beta}(\vec{\mathrm{Q}},\omega) = \frac{1}{2\pi}\sum_{\vec{\mathrm{r}}}\int_0^\infty \mathrm{dt}\ \mathrm{e}^{i\vec{\mathrm{Q}}\cdot\vec{\mathrm{r}}-\omega t} < S_0^\alpha(0) S_{\vec{\mathrm{r}}}^\beta(t) > \qquad (1\text{-}7)$$

, where $< S_0^\alpha(0) S_{\vec{\mathrm{r}}}^\beta(t) >$ is the time-dependent spin-spin correlation function describing how the α component at position 0 correlates with β component of another spin at position $\vec{\mathrm{r}}$ after time t.

Since the scattering function is the Fourier transform in space and time of spin-spin correlation function, the evolution of the system of spins in space and time can be directly measured in a neutron scattering.

In a paramagnetic state, all spin-spin correlations become zero after long times for all α- and β-components of any pair of spins at all 0 and $\vec{r}$ sites. In zero-magnetic field, there is no energy barrier for spin fluctuations, so the scattering is completely elastic. When the system of spins enters an ordered magnetic state, the spins have average value in certain directions for all time. There is at least one pair value of α- and β-components of any pair of spins at all 0 and $\vec{r}$ sites. Then the spin-spin correlation function can be divided into two parts.

$$< S_0^{\alpha}(0) S_{\vec{r}}^{\beta}(t) >=< S_0^{\alpha}(0) S_{\vec{r}}^{\beta}(\infty) > + < S_0^{\alpha}(0)(S_{\vec{r}}^{\beta}(t) - S_{\vec{r}}^{\beta}(\infty)) > \qquad (1\text{-}8)$$

The first part gives elastic cross section and the second part gives inelastic or diffuse cross section.

When the system orders magnetically, the differential cross section for coherent elastic scattering (Bragg scattering) can be written as

$$\frac{d\sigma}{d\Omega} = N_{\mathrm{M}} \frac{(2\pi)^3}{\mathrm{v}_{\mathrm{M}}} \sum_{\vec{\mathrm{G}}_{\mathrm{M}}} \delta(\vec{\mathrm{Q}} - \vec{\mathrm{G}}_{\mathrm{M}}) \,|\, \vec{\mathrm{F}}_{\mathrm{M}}(\vec{\mathrm{G}}_{\mathrm{M}}) \,|^2 \qquad (1\text{-}9)$$

, where v_{M}, N_{M}, and $\vec{\mathrm{G}}_{\mathrm{M}}$ are the volume of the magnetic unit cell, the number of such cells in the sample, and the reciprocal lattice vector of the magnetic unit cell. The magnetic structure factor $\vec{\mathrm{F}}_{\mathrm{M}}$ is defined as

$$\vec{\mathrm{F}}_{\mathrm{M}}(\vec{\mathrm{G}}_{\mathrm{M}}) = p \sum_j f_j \hat{\mathrm{G}}_{\mathrm{M}} \times (< \vec{\mathrm{M}}_j > \times \hat{\mathrm{G}}_{\mathrm{M}}) e^{i\vec{\mathrm{G}}_{\mathrm{M}} \cdot \vec{\mathrm{r}}} e^{-W_j} \qquad (1\text{-}10)$$

, where f_j and $< \vec{\mathrm{M}}_j >$ are the magnetic form factor and the thermal-averaged magnetic moment of j-th ion, respectively. The sum in equation (1-10) is over all sites within the magnetic unit cell. The integrated intensity of a magnetic Bragg peak for unpolarized neutrons is given by

$$I = C \frac{|\vec{F}_M(\vec{G}_M)|^2}{\sin 2\theta} \qquad (1\text{-}11)$$

, where C is a constant depending on the incident neutron flux, sample volume, and counting time and θ is the scattering angle. Therefore, the magnetic spin structure can be determined from the elastic magnetic peak intensity measurement. The equation (1-10) and (1-11) tell that only the spin component perpendicular to $\vec{G}_M$ contribute to the integrated intensity of a magnetic peak. This property is very useful to establish the ordered spin direction. The ordered spin moment can be estimated from the magnetic intensity measurement, since the integrated intensity is proportional to $< \vec{M}_j >^2$.

Chapter 2: Magnetic field effect on the electron-doped $Nd_{2-x}Ce_xCuO_4$

2.1 Review of magnetic field effect on the hole-doped superconductors

The coexistence and competition of magnetism and superconductivity is one of the most important questions to be answered in understanding the mechanism of the high-T_c superconductivity in cuprates [24, 25]. In general, magnetism and superconductivity do not coexist in conventional superconductors. However, many experimental results in hole-doped cuprates show that the antiferromagnetic order coexists with superconductivity. For example, recent elastic neutron scattering experiments confirm that a static incommensurate spin density wave (SDW) coexists with superconductivity in hole-doped superconductors $La_{2-x}Sr_xCuO_4$ (LSCO) and La_2CuO_{4+y} [12, 26]. This quasi-2D SDW has long-range order in the CuO_2 planes and short-range correlation between CuO_2 layers. In underdoped superconducting region, four incommensurate magnetic peaks appear at (0.5±δ, 0.5, 0) and (0.5, 0.5±δ, 0) in the tetragonal unit cell notation, where the antiferromagnetic Bragg peak appears at (0.5, 0.5, 0) in the CuO_2 plane. These magnetic peaks correspond to 2D spin modulation along the Cu-O direction. At optimal doping (with highest T_c), the static SDW order in LSCO vanishes and is replaced by the appearance of a spin gap and incommensurate spin fluctuations at energies above the gap [27].

On the other hand, experiments on insulating (x = 0.01, 0.02, 0.03, 0.04, 0.05) and underdoped superconducting LSCO have shown that two incommensurate magnetic peaks coexist with the 3D antiferromagnetic order in the lightly doped region and survive in the insulating phase. These peaks originate from 1D spin modulation along the diagonal direction (Cu-Cu direction) [8, 9, 10, 11]. But, intriguingly, the four incommensurate peaks are only observed with the establishment of the bulk superconductivity in the underdoped superconducting samples ($0.06 \leq x \leq 0.12$) [11, 12, 13]. Therefore, the insulating-to-superconducting phase transition induced

by increasing hole doping is associated with the appearance of a static quasi-2D SDW modulation.

The experiments on LSCO at a zero-magnetic field show that the antiferromagnetic order coexists with superconductivity in the underdoped region. To determine whether these two coexisting phases compete with each other, many experiments have explored the effects of a magnetic field. This is because the magnetic field is an excellent tool to control the strength of magnetism and superconductivity without changing the samples. High-T_c cuprates are type II superconductors. An applied magnetic field creates vortices along to the field direction in the superconductor. The antiferromagnetic order in the vortex core has been predicted as a competing order in the underdoped superconductors by the SO(5) theory [16, 17].

Neutron scattering experiments on hole-doped LSCO compound show that the application of a magnetic field along the *c*-axis not only suppresses superconductivity, but also enhances the SDW order in the underdoped regime [14, 28]. For optimally doped LSCO without the static SDW order, a *c*-axis magnetic field induces spin fluctuations below the spin-gap energy and does not induce the static antiferromagnetic order [15]. A similar field applied in the CuO_2 plane has little effect on superconductivity and the SDW order [29]. These results strongly suggest that the antiferromagnetic order that coexists with superconductivity is also competing with superconductivity [16, 17, 30, 31, 32, 33, 34]. A similar magnetic field effect is also observed in oxygen-doped $LaCuO_{4+y}$ by neutron scattering studies [35, 36]. The antiferromagnetic order in the vortex cores of the underdoped YBCO family has been reported by Muon spin rotation measurement [37]. Further, nuclear magnetic resonance experiments conducted by Mitrovic *et al.* show the enhanced antiferromagnetic order in the vortex cores of this compound in an applied high magnetic field [38, 39].

If suppression of superconductivity in hole-doped LSCO indeed drives the system toward an antiferromagnetic ordered state, it is important to determine the universality of such a feature

in other cuprates, especially electron-doped cuprates. Compared to hole-doped cuprates, electron-doped materials offer a unique opportunity for studying the magnetic field-induced effect for two reasons. First, electron-doped materials generally have upper critical fields less than 15 T [40, 41, 42], a value reachable in neutron scattering experiments. Second, electron-doped materials can be transformed from as-grown nonsuperconducting antiferromagnetic insulators to full superconductivity by simply annealing the samples at different temperatures to modify the charge carrier density [43, 44, 45, 46, 47]. This unique property allows the possibility of studying the nonsuperconducting to superconducting transition in electron-doped cuprates without the complications of structural and/or chemical disorder induced by chemical substitution in hole-doped materials.

In this chapter, I will describe the magnetic field effect on parent Nd_2CuO_4, nonsuperconducting, and superconducting $Nd_{1.85}Ce_{0.15}CuO_4$.

2.2 Sample preparation and experimental setup

We grew a single crystal of Nd_2CuO_4 and crystals of $Nd_{1.85}Ce_{0.15}CuO_4$ using the traveling solvent floating zone technique [48]. The Nd_2CuO_4 crystal used in the experiments is an as-grown sample. Unlike hole-doped superconductors, as-grown samples of electron-doped materials are not superconducting. To achieve superconductivity, an as-grown $Nd_{1.85}Ce_{0.15}CuO_4$ was annealed in a flowing Ar/O_2 gas mixture with a partial oxygen pressure of $\sim 10^{-5}$ atm at 1000° C for 100 h.

The samples were characterized by resistivity and magnetic susceptibility measurements, as shown in Fig. 2.1. In-plane resistivity ρ_{ab} at zero field and magnetic susceptibility are measured on a small piece of superconducting crystal (~200 mg) cut from the sample used for neutron experiments. Figure 2.1(a) and (b) show the onset temperature for bulk superconductivity at T_c = 25 K and a transition width of 3 K. With a *c*-axis aligned field of 10 Gauss, magnetic susceptibility data in zero-field-cooled shows a complete screening of the flux. In the field-cooled

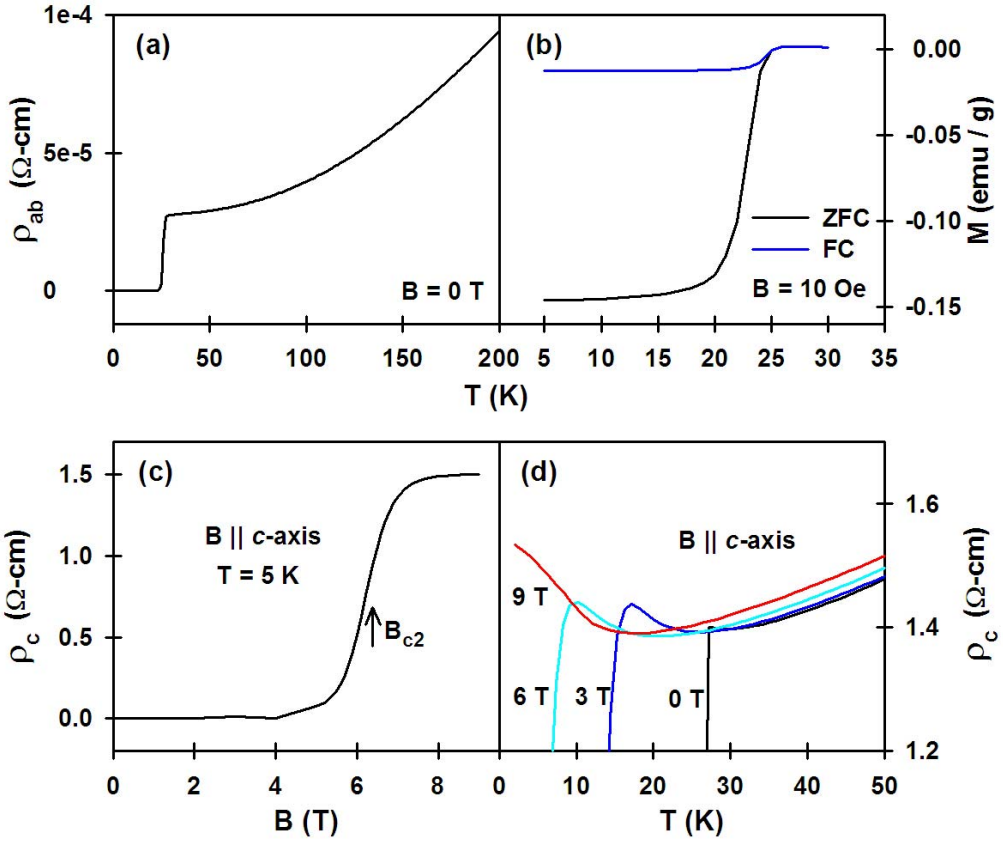

Fig. 2.1 Transport measurements of $Nd_{1.85}Ce_{0.15}CuO_4$ as a function of temperature. (a) In-plane resistivity $\rho_{ab}(T)$ at 0 T. (b) Magnetic susceptibility measurement M(T). Zero-field-cooled data and field-cooled data in 10 Oe field are shown. (c) Out-of-plane resistivity $\rho_c(T)$ as a function of a magnetic field. (d) Temperature dependence of $\rho_c(T)$ at different magnetic fields.

case, the crystal expels 18% of the flux, indicating that the bulk superconductivity has at least 18% of the volume fraction. The sharpness of the magnetic susceptibility measurement suggests that the crystal is homogeneous with bulk superconductivity. The out-of-plane resistivity (ρ_c) measurement on a superconducting $Nd_{1.85}Ce_{0.15}CuO_4$ (T_c = 25 K) shows that at 5 K, a *c*-axis aligned field induces superconducting to normal state transition at B_{c2} = 6.2 T (Fig. 2.1(c)). Figure 2.1(d) displays ρ_c as a function of temperature for several applied magnetic fields. In a field of 9 T that exceeds B_{c2}, ρ_c initially decreases when temperature decreases but shows an anomalous upturn for temperatures T < 12 K, similar to $Pr_{1.85}Ce_{0.15}CuO_4$ [41, 49].

The magnetic susceptibility of superconducting $Nd_{2-x}Ce_xCuO_4$ in the CuO_2 planes is several times larger than the magnetic susceptibility in the plane perpendicular to the CuO_2 plane. The large magnetic anisotropy means that a *c*-axis aligned field acting on the magnetic moments of Nd^{3+} and Cu^{2+} produces a large torque on the sample. To prevent the samples from rotating under the influence of a magnetic field **B** || *c*-axis, they were clamped on solid aluminum brackets.

Our experiments were performed on the BT-2 and BT-9 triple-axis spectrometers at the NIST Center for Neutron Research and on the E4 two-axis diffractometer at the Berlin Neutron Scattering Center, Hahn-Meitner-Institute (HMI). For experiments at NIST, the bracket was inserted inside a He filled aluminum can mounted on a standard 7-T superconducting magnet. For HMI experiments, the sample assembly was mounted on a mini-goniometer and inserted directly to the sample chamber of the HM2 magnet.

We measure the momentum transfer (q_x ,q_y ,q_z) in units of $Å^{-1}$ and specify the reciprocal space positions (*H, K, L*) = (q_x *a*/2π, q_y *a*/2 π, q_z *c*/2 π) in reciprocal lattice units (r.l.u.) appropriate for the tetragonal unit cells of Nd_2CuO_4 (space group I4/mmm, *a* = 3.944 and *c* = 12.169 Å) and $Nd_{1.85}Ce_{0.15}CuO_4$ (space group I4/mmm, *a* = 3.945 and *c* = 12.044 Å), where *a* and *c* are in-plane and out-of-plane lattice parameters, respectively.

For NIST experiments, the collimations were, proceeding from the reactor to the detector, 40′-46′-sample-40′-80′ (fullwidth at half-maximum), and the final neutron energy was fixed at E_f = 14.7 meV. The monochromator, analyzer and filters were all pyrolytic graphite. For magnetic field experiments, we first aligned the CuO_2 planes in the horizontal [*H K* 0] scattering plane and applied the vertical magnetic field along the *c*-axis (**B** || *c*-axis). In this geometry, we can access reciprocal space at any (*H, K,* 0). Next, to determine the anisotropy of the field-induced effect, we also performed experiments in the [*H H L*] scattering plane where the applied vertical fields are along the [-1 1 0] direction (**B** || *ab*-plane).

For E4 measurements at HMI, we used a 40′-40′-sample-40′ collimation with a fixed incident neutron energy of E_i = 13.6 meV. A pyrolytic graphite filter was placed in front of the sample to eliminate higher order contamination. The 4-T horizontal field magnet (HM2) was used to apply a *c*-axis aligned magnetic field while probing the *L* modulation of the scattering. Although these measurements are crucial in determining the field-induced magnetic structure, the highly restricted access angles of the magnet limit the regions of reciprocal space that can be probed. In horizontal field measurements on $Nd_{1.85}Ce_{0.15}CuO_4$, the crystal was aligned in the [*H H L*] zone and the magnetic field was applied along the *c*-axis.

2.3 Magnetic structure

To determine the influence of a magnetic field on the antiferromagnetic order of electron-doped superconductor $Nd_{2-x}Ce_xCuO_4$, it is helpful to know the magnetic structure of its parent compound. Nd_2CuO_4 has a body-centered tetragonal structure with space group I4/mmm (Fig. 1.2 (b)). The spins of Cu^{2+} ions have antiferromagnetic ordering in the CuO_2 plane due to strong in-plane exchange interaction. Since exchange field on each copper ion by neighboring planes is canceled out due to body-centered tetragonal crystal symmetry, its spin direction is frustrated.

Therefore, the orientation of spins in adjacent planes is governed by weak pseudo-dipolar interaction between planes, which prefers the noncollinear spin structure [50, 51, 52].

When the temperature is cooled below the Néel temperature T_{N1} = 275 K, the Cu^{2+} spins in Nd_2CuO_4 order into the noncollinear structure of type-I shown in Fig. 2.2(a). With further cooling, the Cu^{2+} spins reorient into the type-II structure at T_{N2} = 75 K (Fig. 2.2(b)) and the type-III structure at T_{N3} = 30 K (Fig. 2.1(a)). All the Cu^{2+} spins rotate by 90° about the *c*-axis at the spin reorientation transition from the type-I to type-II, and they rotate back to their original direction below T_{N3} [50, 53, 54, 55]. The ordered Cu^{2+} sublattice induces a staggered field at the Nd^{3+} site. This causes Nd^{3+} spins to order antiferromagnetically in much lower temperature at 1.5 K. The directions of Cu^{2+} and Nd^{3+} spins are in the *ab*-plane. They are coupled along the *c*-axis ferromagnetically in phase-I/III and antiferromagnetically in phase-II.

We performed neutron scattering measurements on a parent compound Nd_2CuO_4 to check previous results on the magnetic structures. Figure 2.3 shows the temperature dependent scattering at antiferromagnetic positions. The intensity change of (0.5, 0.5, 0) and (0.5, 1.5, 0) as a function of temperature shows clear magnetic structure phase transitions at T_{N1}, T_{N2}, and T_{N3} marked by the arrows in Fig. 2.3, confirming previous work. The large intensity increase of the (0.5, 1.5, 0) peak below ~20 K is associated with staggered moments of Nd^{3+} ions induced by Cu-Nd exchange coupling.

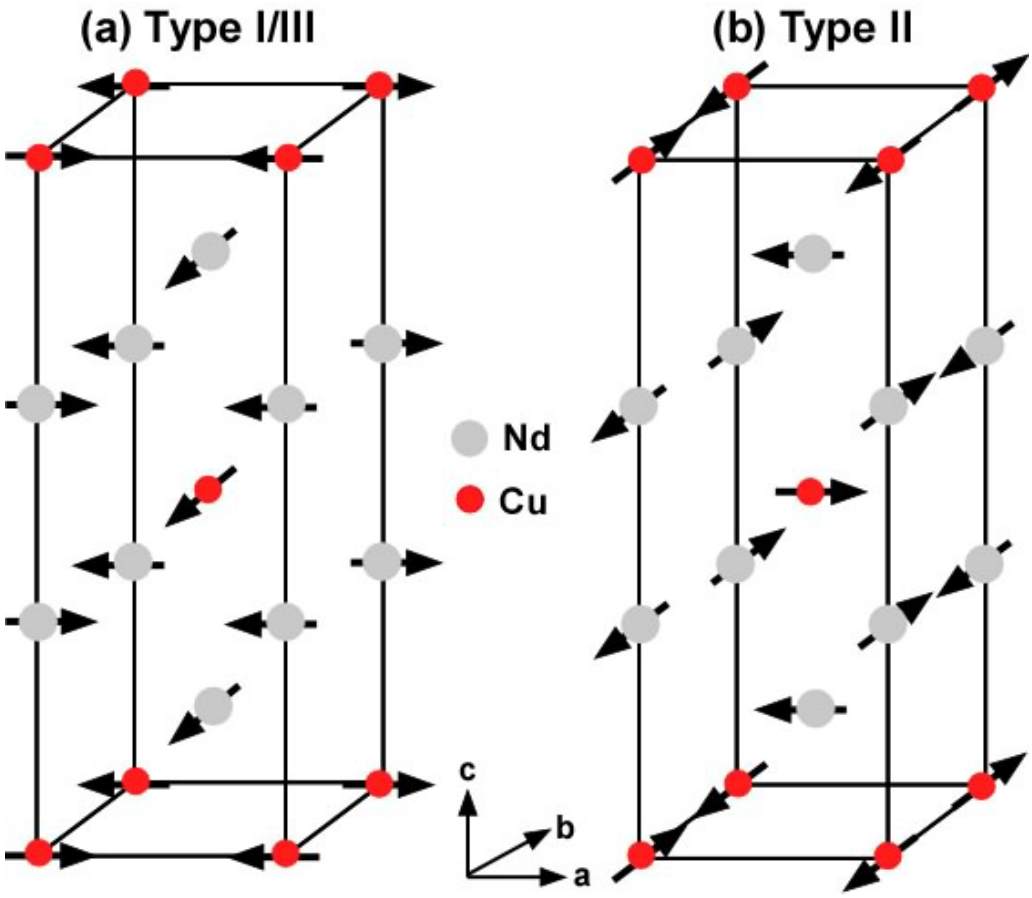

Fig. 2.2 Noncollinear spin structures of Nd_2CuO_4. (a) type-I (75 K < T < 275 K) and type-III (T < 30 K) phases, and (b) type-II (30 K < T < 75 K) phase. Nonmagnetic oxygen atoms are omitted for the simplicity.

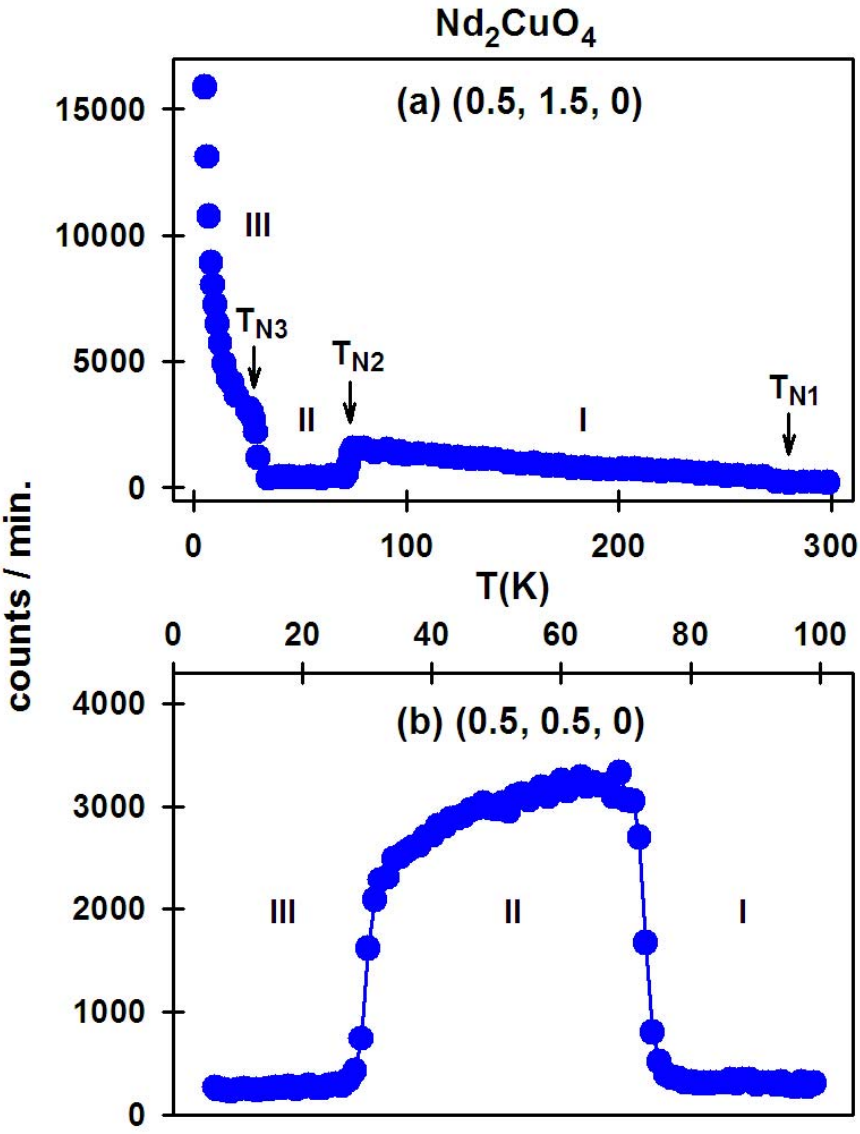

Fig. 2.3 Intensity of antiferromagnetic peaks as a function of temperature. (a) The (0.5, 1.5, 0) peak and (b) the (0.5, 0.5, 0) peak show the phase transition with decreasing temperatures.

Table 2.1 Magnetic structure factor calculations for the noncollinear type-I/III and type-II phases of Nd_2CuO_4. $f_{cu,nd}$ and $M_{cu,nd}$ are magnetic form factors and ordered magnetic moments for Cu^{2+} and Nd^{3+} ions, respectively. Here neutron-electron coupling $p = \gamma e^2/(2m_e c^2) = 0.2695\times10^{-12}$ cm.

(H, K, L)	$\lvert F_{I/III}\rvert^2$	$\lvert F_{II}\rvert^2$
(0.5, 0.5, 0)	0	$32\, p^2\, (f_{cu} M_{cu} + 2 f_{nd} M_{nd})^2$
(0.5, 1.5, 0)	$25.6\, p^2\, (f_{cu} M_{cu} + 2 f_{nd} M_{nd})^2$	$6.4\, p^2\, (f_{cu} M_{cu} - 2 f_{nd} M_{nd}{}^2$

Table 2.1 shows the magnetic structure factor calculations of antiferromagnetic Bragg peaks for the noncollinear type-I/III and type-II phases of Nd_2CuO_4. It shows that the (0.5, 0.5, 0) reflection has a vanishing intensity in the type-I/III phases and becomes finite in the type-II phase. The large intensity jumps of (0.5, 0.5, 0) at T_{N2} and T_{N3} shown in Fig. 2.3(b) clearly bear this out. The peak at (0.5, 1.5, 0) is allowed in all three phases. It has smaller values in type-II phase because of negative Nd^{3+} moment contribution. This is shown in the decrease of intensity of (0.5, 1.5, 0) in the temperature range from 30 K to 75 K (Fig. 2.3(a)).

To estimate the magnetic moments of Cu^{2+} and Nd^{3+} ions in different phases of Nd_2CuO_4, we normalized the intensity of antiferromagnetic peaks at (0.5, 0.5, 0) and (0.5, 1.5, 0) to that of the weak (1, 1, 0) or strong (2, 0, 0) nuclear Bragg peak. Table 2.2 shows the estimated Nd^{3+} and Cu^{2+} moments for both cases. The estimated Cu^{2+} and Nd^{3+} moments differ dramatically depending on the chosen Bragg peaks. This is due primarily to the extinction, but there is also Nd^{3+} absorption of the large crystal. In particular, the intensities of the strong peaks such as (2, 0, 0) are severely extinction limited, which overestimates the magnitude of the ordered moment.

Table 2.2 Calculated magnetic moments of Cu^{2+} and Nd^{3+} ions in Nd_2CuO_4. The intensity of (0.5, 0.5, 0) and (0.5, 1.5, 0) is normalized to that of weak (1, 1, 0) or strong (2, 0, 0) structural Bragg reflection. The powder diffraction measurements on Nd_2CuO_4 in ref. 54 show that the estimated Cu^{2+} moment is 0.46 μ_B at 80 K and Nd^{3+} moment is 0.46 μ_B at 5 K. In our calculations of Cu^{2+} and Nd^{3+} moments, we assume that the Nd^{3+} moment does not contribute to the magnetic scattering above 50 K and that the Cu^{2+} moment does not change below 50 K.

Normalized to (*H, K, L*)	Moments in μ_B	At 5 K	At 55 K	At 100 K
(1, 1, 0)	M_{cu} M_{nd}	0.1 0.16 ± 0.01	0.1 ± 0.01 0	0.12 ± 0.04 0
(2, 0, 0)	M_{cu}	1.2	1.2 ± 0.2	1.0 ± 0.2

Ce^{4+} doping may influence the magnetic structure of these samples. To check this, we measured intensity at (0.5, 1.5, 0) and (0.5, 0.5, 0) positions in an as-grown $Nd_{1.85}Ce_{0.15}CuO_4$ sample. Figure 2.4(a) and (b) show intensities of the (0.5, 1.5, 0) and (0.5, 0.5, 0) as a function of temperature. The intensity of (0.5, 1.5, 0) peak increases with decreasing temperature, while the (0.5, 0.5, 0) peak intensity is independent of temperature. This confirms that an as-grown nonsuperconducting sample orders antiferromagnetically in type-I/III phase. Note that the continuous increase of (0.5, 1.5, 0) intensity shows that an as-grown sample does not have a spin orientation transition. This is different from the parent Nd_2CuO_4 compound.

The magnetic structure of superconducting $Nd_{1.85}Ce_{0.15}CuO_4$ sample is also studied. Figure 2.4(c) and (d) are the measurements at (0.5, 1.5, 0) and (0.5, 0.5, 0) as a function of temperature. Although antiferromagnetism in the heat-treated $Nd_{1.85}Ce_{0.15}CuO_4$ is greatly reduced, it could not be completely eliminated, and the residual antiferromagnetic order coexists with superconductivity for even the highest T_c = 25 K material [56, 57]. The superconducting sample

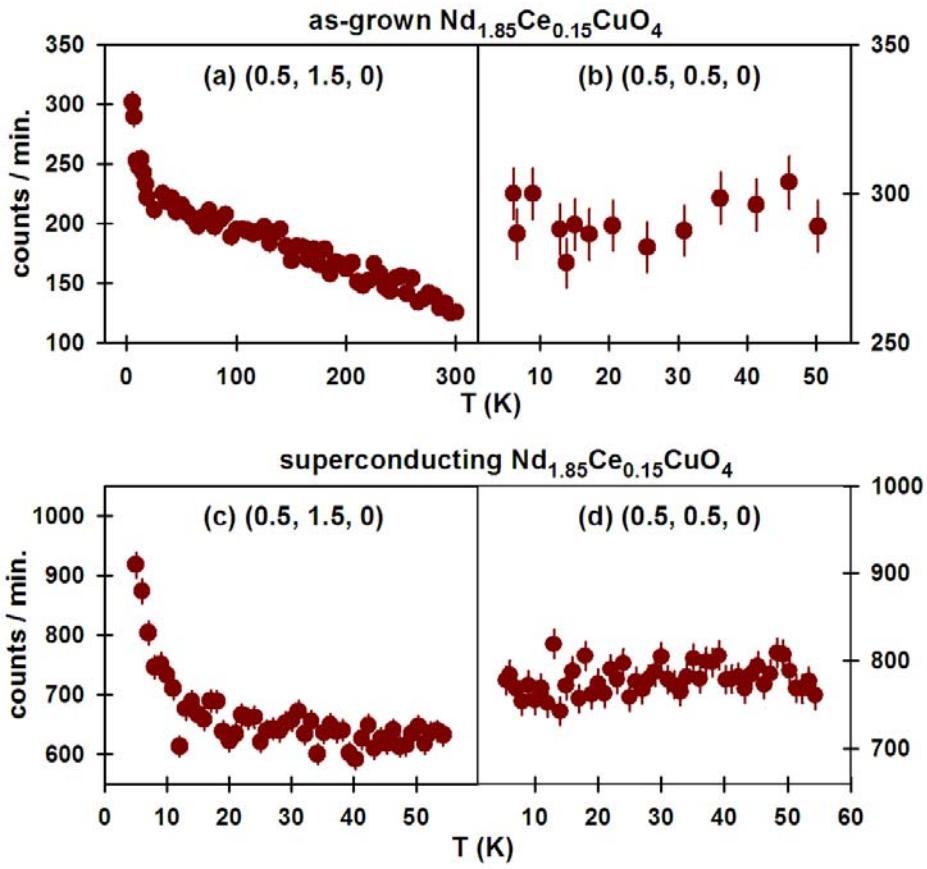

Fig. 2.4 Intensities of (0.5, 1.5, 0) and (0.5, 0.5, 0) as a function of temperature. (a)-(b) the temperature dependence of (0.5, 1.5, 0) and (0.5, 0.5, 0) in an as-grown $Nd_{1.85}Ce_{0.15}CuO_4$ sample, and (c)-(d) the same measurements in the superconducting $Nd_{1.85}Ce_{0.15}CuO_4$ sample.

shows similar temperature dependence at (0.5, 1.5, 0) and (0.5, 0.5, 0) positions to that in an as-grown nonsuperconducting sample with much lower T_N. Therefore, the superconducting sample also has type-I/III phase.

2.4 A *c*-axis magnetic field effect on the parent Nd_2CuO_4

The neutron scattering experiment on Nd_2CuO_4 has shown that a magnetic field **B** || [-1 1 0] (*ab*-plane) induces a second order spin-flop transition from the noncollinear type-I/III to a collinear structure domain-I shown in Fig. 2.5 [55]. The critical field for such a spin-flop transition is 0.8 T at 5.6 K [55]. This is because the interplane pseudodipolar interaction energy does not change when the spin sublattices of adjacent CuO_2 planes rotate in opposite directions [51, 52, 58]. Such a continuous spin rotation can be induced by a magnetic field parallel to Cu-Cu direction, which easily converts the noncollinear structure into the collinear one with spins along the [1 1 0] direction.

However, a *c*-axis magnetic field effect on the antiferromagnetic order in Nd_2CuO_4 has not been studied yet. A *c*-axis magnetic field effect on parent compounds can be very important in studying the relationship between antiferromagnetism and superconductivity in cuprates.
To study a *c*-axis magnetic field effect on type-III antiferromagnetic order, we measured peaks at (0.5, 1.5, 0) and (0.5, 0.5, 0) at 5 K with and without a magnetic field. Figure 2.6(a)-(c) show scans around the antiferromagnetic positions (0.5, 1.5, 0), (0.5, 0.5, 0), and structural and ferromagnetic Bragg reflection (1,1,0). At a zero-field, we observe a resolution-limited magnetic peak at (0.5, 1.5, 0), but not in (0.5, 0.5, 0). This is expected from the type-III spin structure. These peaks are not affected by a *c*-axis aligned magnetic field up to 7 T. The lack of intensity changes between 0- and 7-T data at (0.5, 1.5, 0) and (0.5, 0.5, 0) positions indicates that the applied magnetic field neither enhances the type-III antiferromagnetic order nor induces a new antiferromagnetic spin structure. On the other hand, the application of a 7-T **B** || *c*-axis

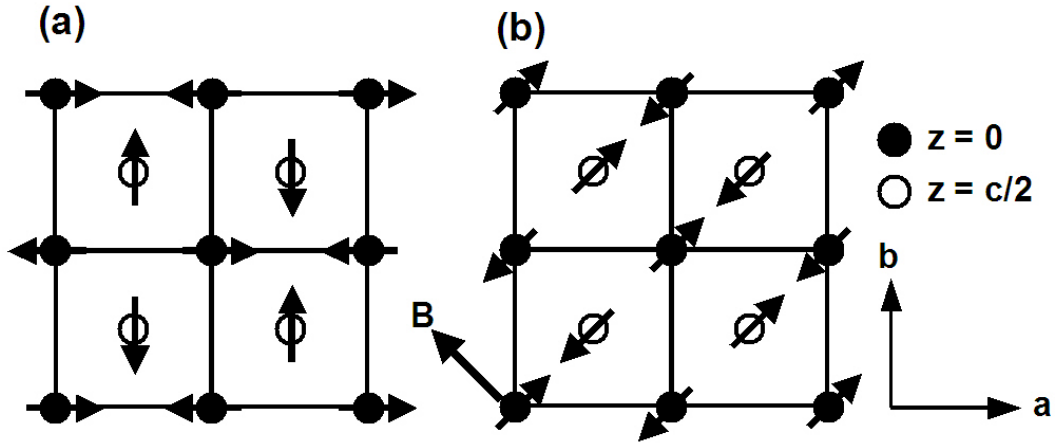

Fig. 2.5 Magnetic structures of Cu^{2+} ions in Nd_2CuO_4. (a) Noncollinear type-I/III structure at a zero-magnetic field. (b) Collinear structure domain-I transformed by a magnetic field applied along the [-1 1 0] direction. In the collinear structure, the spins are antiparallel. In the spin-flopped state, the spins are perpendicular to a magnetic field.

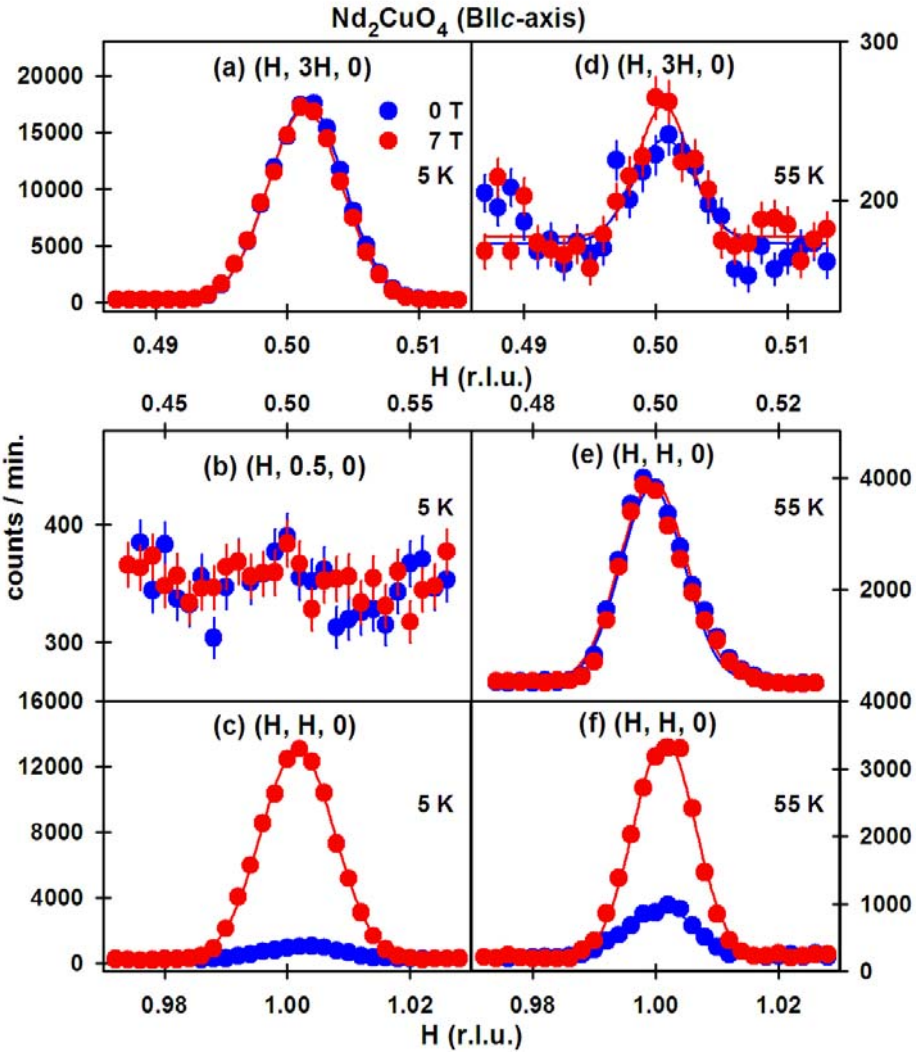

Fig. 2.6 A *c*-axis magnetic field effect on the antiferromagnetic and ferromagnetic peaks of Nd_2CuO_4. (a)-(c) Scans around (0.5, 1.5, 0), (0.5, 0.5, 0), and (1, 1, 0) in type-III phase and (d)-(f) Similar scans around (0.5, 1.5, 0), (0.5, 0.5, 0) and (1, 1, 0) in type-II phase. A *c*-axis magnetic field has no effect on the antiferromagnetic peaks at (0.5, 1.5, 0) and (0.5, 0.5, 0), while it induces ferromagnetic peak at (1, 1, 0).

induces long-range ferromagnetic ordering as seen by the added magnetic intensity to the (1, 1, 0) structural Bragg peak intensity (Fig. 2.6(c)). Such an enhancement is most likely due to the polarization of the Nd^{3+} moment in the sample.

To determine the effect of a 7-T magnetic field on the type-II phase, we repeated the measurements around (0.5, 1.5, 0), (0.5, 0.5, 0), and (1, 1, 0) positions at 55 K. The outcome of the experiments plotted in Fig. 2.6(d)-(f). Note that the (0.5, 0.5, 0) reflection that is forbidden in the type-III spin structure appears in type-II phase. The data clearly shows that a 7-T magnetic field only induces ferromagnetic ordering at (1, 1, 0) and has negligible effect on the intensities of type-II antiferromagnetic Bragg reflections at (0.5, 1.5, 0) and (0.5, 0.5, 0). Comparing Fig. 2.6(c) to Fig. 2.6(f), we find that the ferromagnetic enhancement of the (1, 1, 0) reflection is smaller in the type-II phase than type-III phase. This is because the magnetic moment disorders with increasing temperature.

Since the high temperature type-I phase has the same magnetic structure as the type-III phase but without the complication of significantly polarized Nd^{3+} moments, measurements there should provide information concerning the magnetic field effect on only the Cu^{2+} moments. Figure 2.7 summarizes a *c*-axis magnetic field effect on antiferromagnetism and ferromagnetism in the type-I phase at 100 K and in the paramagnetic state at 300 K. Figure 2.7(a) and (d) show that a *c*-axis magnetic field of 7 T does not enhance the antiferromagnetic order at (0.5, 1.5, 0) in the type-I phase and the paramagnetic state. The absence of peak at (0.5, 0.5, 0) shows that a *c*-axis magnetic field does not induce new magnetic structure, neither type-I nor type-II (Fig. 2.7(b) and (e)). The enhancement of ferromagnetism at (1, 1, 0) by a magnetic field is still present at 100 K, but is too small to observe in the paramagnetic state at 300 K (Fig. 2.7(c) and (f)). The disappearance of (0.5, 1.5, 0) and (0.5, 0.5, 0) peaks at 300 K indicates that these peaks at low temperature are magnetic peaks.

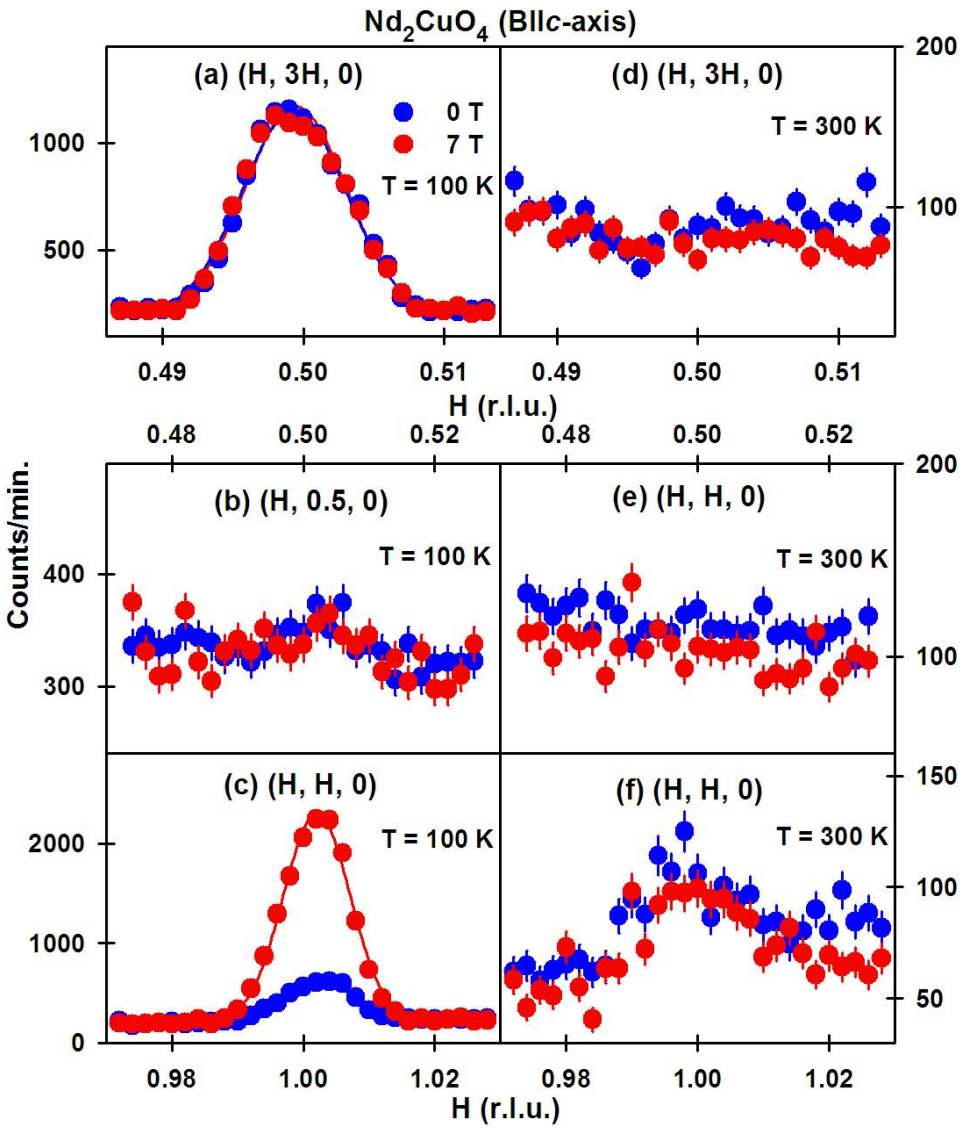

Fig. 2.7 A *c*-axis magnetic field effect on antiferromagnetism and ferromagnetism in type-I phase at 100 K and in the paramagnetic state at 300 K. (a)-(c) Scans around (0.5, 1.5, 0), (0.5, 0.5, 0), and (1, 1, 0) at 100 K (type-I). (d)-(f) Similar scans around same peaks at 300 K (paramagnetic state).

Figure 2.8 summarizes the effects of magnetic field on the antiferromagnetic and ferromagnetic ordering in all phases of Nd_2CuO_4. The integrated intensity of antiferromagnetic peak (0.5, 1.5, 0) changes negligibly with a *c*-axis magnetic field in all phases (Fig. 2.8(a)-(c)), and (0.5, 0.5, 0) shows no magnetic field dependence, either (Fig. 2.8(e)). The quadratic increase of (1, 1, 0) integrated intensities in Fig. 2.8(d) and (f) indicates that the field-induced Cu/Nd ferromagnetic moments increase linearly with increasing magnetic field, since the measured integrated intensity is proportional to square of the magnetic moment (Eq. 1-10 and 1-11 in chapter 1). The coefficient of quadratic curve in the (1, 1, 0) integrated intensity is decreased in the type-I phase compared to that in the type-III phase. Such a decrease is expected due to the reduced magnetic moment of the Nd^{3+} contribution to the field-induced ferromagnetism at higher temperatures.

Figure 2.9 shows the measurements of temperature dependence at (0.5, 1.5, 0), (1, 1, 0), and (0.5, 0.5, 0) under a *c*-axis aligned magnetic field to determine its influence across different antiferromagnetic phase transitions and ferromagnetism. The increasing intensity of (1, 1, 0) with decreasing temperature indicates that long-range ferromagnetic ordering is induced below ~250 K by a 7-T magnetic field (Fig. 2.9(b)). A 7-T magnetic field thus induces ferromagnetic moments on Cu/Nd sites not far below T_{N1}. On the other hand, there is very little intensity change between 0- and 7-T at (0.5, 1.5, 0) and (0.5, 0.5, 0) positions across T_{N2} and T_{N3} (Fig. 2.9(a) and (c)). Therefore, it becomes clear that a magnetic field applied along a *c*-axis has no effect on antiferromagnetism in all three phases of Nd_2CuO_4 and it does not induce magnetic structure transition.

2.5 A *c*-axis magnetic field effect on the as-grown $Nd_{1.85}Ce_{0.15}CuO_4$

Although our results show conclusively that a 7-T magnetic field has no effect on the long-range antiferromagnetic order in all phases of Nd_2CuO_4, one still needs to determine the

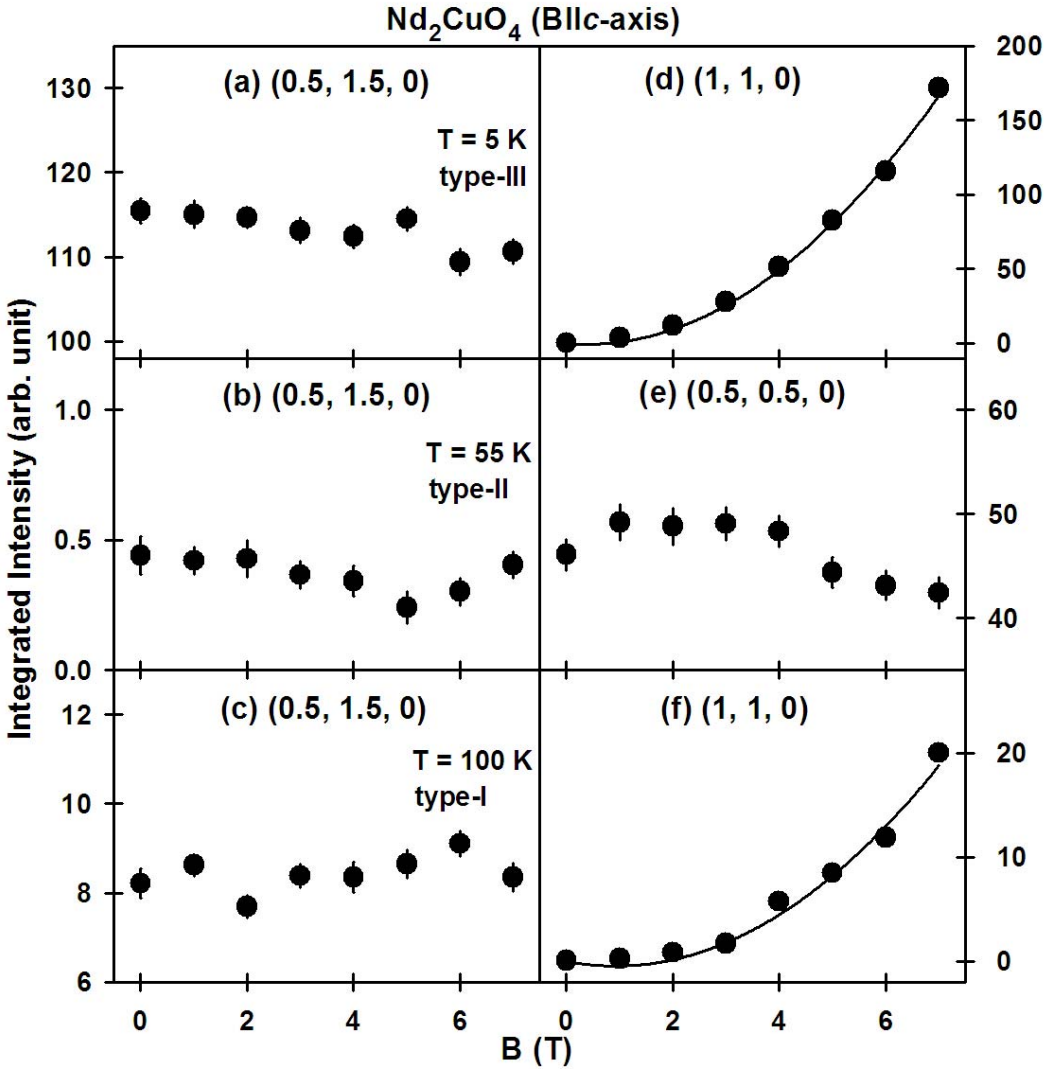

Fig. 2.8 A *c*-axis magnetic field effect on antiferromagnetism and ferromagnetism in all phases of Nd_2CuO_4. (a)-(c) Integrated intensity of (0.5, 1.5, 0) as a function of magnetic field in all phases. Integrated intensity of (d) (1, 1, 0) in type-III, (e) (0.5, 0.5, 0) in type-II, (f) (1, 1, 0) in type-I as a function of magnetic field.

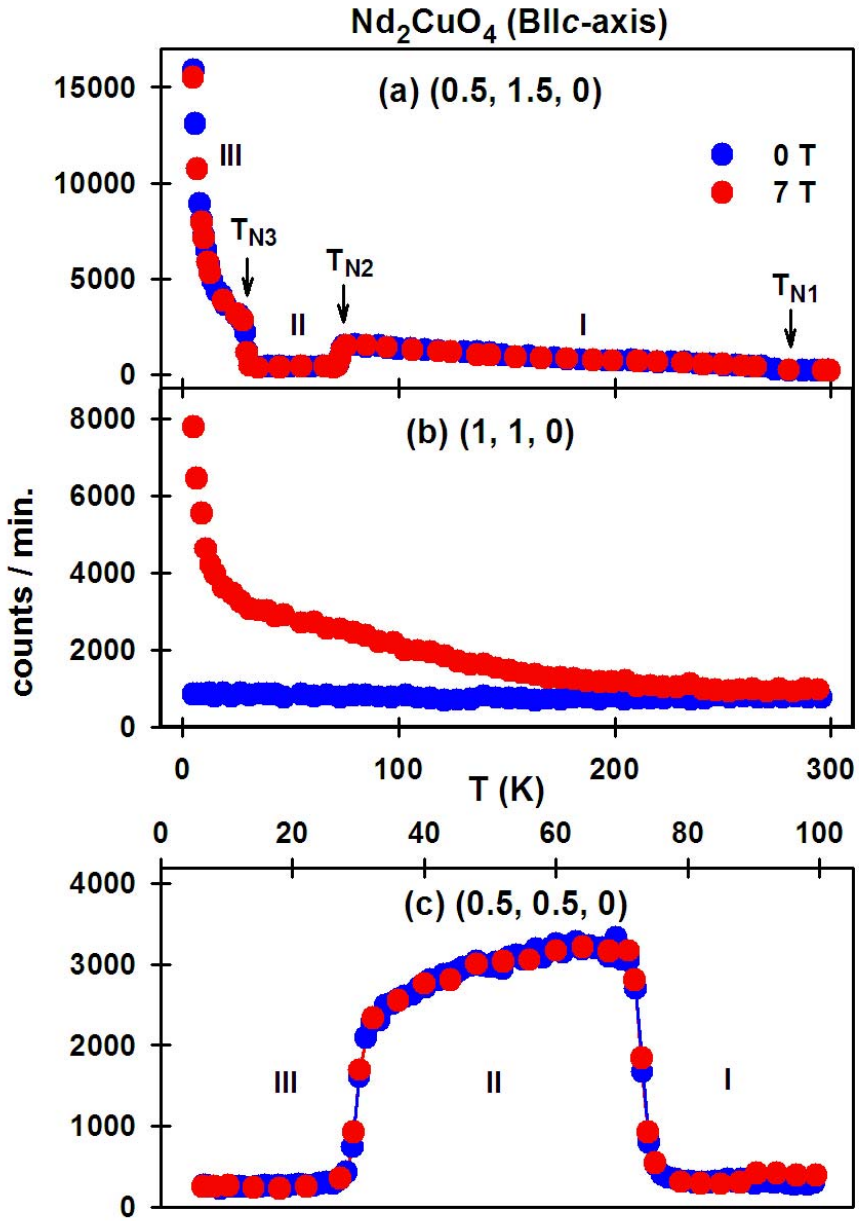

Fig. 2.9 Temperature dependence at (0.5, 1.5, 0), (1, 1, 0), and (0.5, 0.5, 0) under a *c*-axis magnetic field in all magnetic phases. Intensity of (a) (0.5, 1.5, 0), (b) (1, 1, 0), and (c) (0.5, 0.5, 0) as a function of temperature at 0 T and 7 T.

magnetic field effect on the as-grown nonsuperconducting $Nd_{1.85}Ce_{0.15}CuO_4$ because Ce^{4+} doping may influence the magnetic response of the system to a *c*-axis aligned magnetic field. In section 2.3 we find that the as-grown $Nd_{1.85}Ce_{0.15}CuO_4$ orders antiferromagnetically with the type-I/III structure.

We aligned an as-grown $Nd_{1.85}Ce_{0.15}CuO_4$ in [*H K* 0] scattering plane and applied a magnetic field along a *c*-axis. Figure 2.10 summarizes the magnetic field effect on antiferromagnetism and ferromagnetism in the as-grown $Nd_{1.85}Ce_{0.15}CuO_4$. A *c*-axis magnetic field of 6.9-T has no effect on the antiferromagnetic peak at (0.5, 1.5, 0) observed at zero-magnetic field and 5 K (Fig. 2.10(a)). We also find that a magnetic field does not induce the antiferromagnetic peak at (0.5, 0.5, 0), but it enhances the ferromagnetic order at (1, 1, 0) dramatically (Fig. 2.10(b) and (d)). On warming the system to room temperature, the antiferromagnetic peak at (0.5, 1.5, 0) disappears. This indicates that the intensity of (0.5, 1.5, 0) at low temperature is entirely magnetic in origin. Since the (0.5, 1.5, 0) reflection has the same temperature dependence as (0.5, 0.5, 3) [54], the absence of a field-induced effect at (0.5, 1.5, 0) is a direct evidence of no field-induced effect at (0.5, 0.5, 3) in the as-grown nonsuperconducting $Nd_{1.85}Ce_{0.15}CuO_4$. Therefore, we conclude that a 7-T *c*-axis aligned magnetic field has negligible effect on the antiferromagnetic order of the system.

2.6 A *c*-axis magnetic field effect on the superconducting $Nd_{1.85}Ce_{0.15}CuO_4$

A competing ground state to superconductivity can be revealed by the application of a magnetic field. Unlike hole-doped superconductors, the electron-doped superconductors give a unique opportunity to reveal the quantum phase transition from the superconducting state to the normal state because of their reachable upper critical field (B_{c2}) [40]. Our superconducting $Nd_{1.85}Ce_{0.15}CuO_4$ sample has B_{c2} = 6.2 T at 5 K (Fig. 2.1(c)).

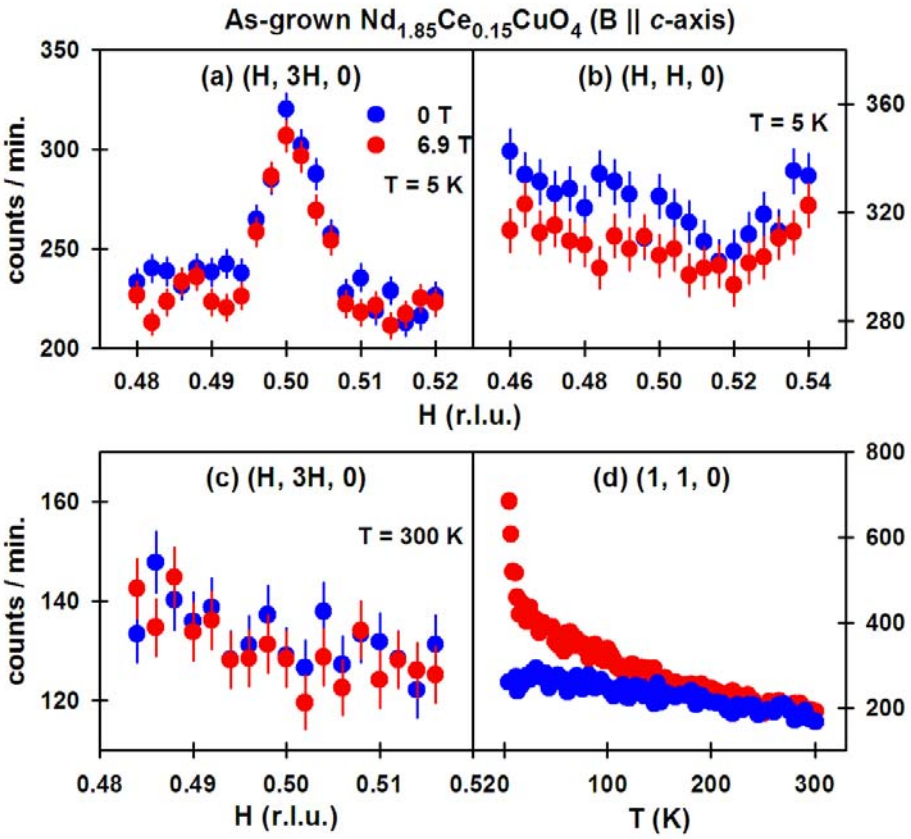

Fig. 2.10 A *c*-axis magnetic field effect on antiferromagnetism and ferromagnetism of as-grown $Nd_{1.85}Ce_{0.15}CuO_4$. (a) Scans at (0.5, 1.5, 0) at 5 K. (b) Scans at (0.5, 0.5, 0) at 5 K. (c) Scans at (0.5, 1.5, 0) at 300 K. (d) Intensity of (1, 1, 0) as a function of temperature. Blue circles are zero field data and red circles are 6.9 T data.

For neutron scattering measurements, we aligned the crystal in the [*H K* 0] scattering plane and applied a magnetic field along a *c*-axis. Figure 2.11 summarizes the results of a *c*-axis magnetic field effect. In section 2.3, we find that a superconducting sample has the antiferromagnetic order with type-I/III structure below the Néel temperature (< 40 K) (Fig. 2.4(c)). From Fig. 2.11, we observe peaks at (0.5, 0.5, 0) and (0.5, 1.5, 0) at 55 K above the Néel temperature. These are structural peaks originating from the superstructure and the impurity phase [59, 60]. Note that these structural peaks do not exist in the as-grown sample (section 2.3). On cooling to 5 K at zero-field, the magnetic scattering develops at (0.5, 1.5, 0), but not at (0.5, 0.5, 0), which is expected in type-I/III phase. The application of a *c*-axis magnetic field at 5 K enhances the magnetic scattering of both the antiferromagnetic peaks at (0.5, 0.5, 0) and (0.5, 1.5, 0). However the field does not induce the static antiferromagnetic order at high temperature of 55 K.

Figure 2.12 shows the scans around (0.5, 0.5, 0) and (1, 1, 0) and their integrated intensities as a function of magnetic field at 5 K. The maximum magnetic field 14.5 T is well above B_{c2}. The integrated intensity of (0.5, 0.5, 0) shows that the field-induced moment increases with increasing field up to B_{c2} (~6.2 T), and it starts to decrease above B_{c2} (Fig. 2.12(c)). The decrease of field-induced signal is due to the canting of antiferromagnetism. The change of field-induced effect around 6.2 T is the indication of a quantum phase transition from the superconducting state to the antiferromagnetic ordered state. While the field-induced ferromagnetism at (1, 1, 0) continues to rise for magnetic fields above B_{c2}, and it does not saturate for fields up to 14.5 T (Fig. 2.12(d)). We believe that the *c*-axis field-induced antiferromagnetic signal arises from the suppression of superconductivity by the *c*-axis aligned field.

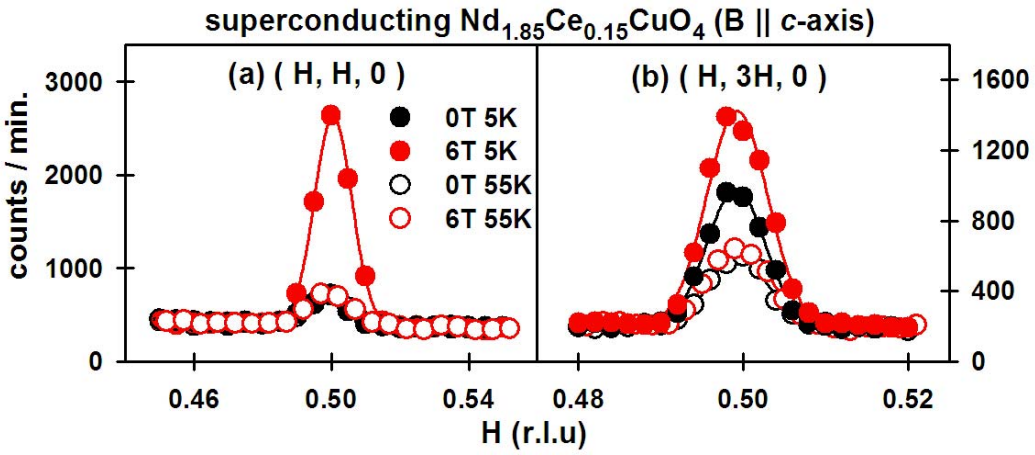

Fig. 2.11 A *c*-axis magnetic field effect on the antiferromagnetic peaks in the superconducting $Nd_{1.85}Ce_{0.15}CuO_4$. Scans of at (a) (0.5, 0.5, 0) and (b) (0.5, 1.5, 0).

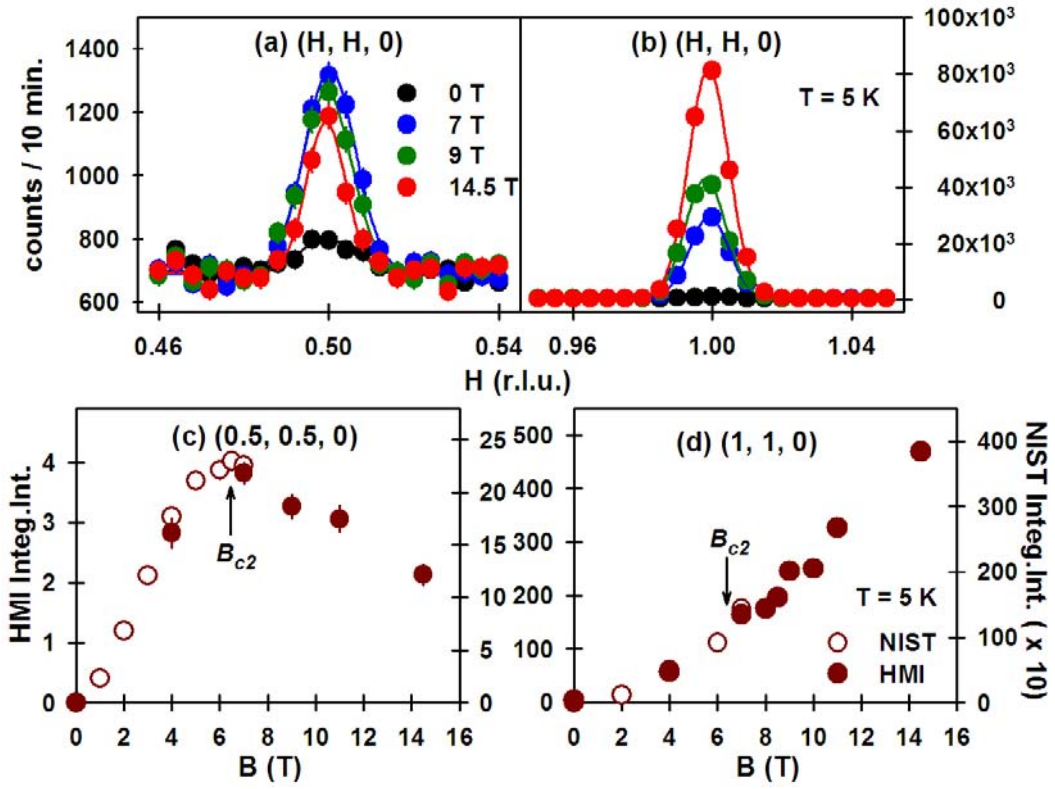

Fig. 2.12 Antiferromagnetic and ferromagnetic peaks as a function of magnetic field at 5 K. (a)-(b) Scans of (0.5, 0.5, 0) and (1, 1, 0) with different magnetic fields. (c)-(d) Integrated intensities of (0.5, 0.5, 0) and (1, 1, 0) as a function of magnetic field.

2.7 In-plane magnetic field effect on the superconducting $Nd_{1.85}Ce_{0.15}CuO_4$

In this section, we describe the *ab*-plane magnetic field effect to compare the results of a *c*-axis magnetic field effect on the superconducting $Nd_{1.85}Ce_{0.15}CuO_4$. This is because a magnetic field **B** || *c*-axis suppresses superconductivity much more strongly than a magnetic field **B** || *ab*-plane in highly anisotropic layered superconductors.

To check the *ab*-plane magnetic field effect on a superconducting $Nd_{1.85}Ce_{0.15}CuO_4$, we aligned the sample in the [*H H L*] scattering plane and measured several antiferromagnetic peaks at (0.5, 0.5, *L* = 1, 2, 3, 4) under a magnetic field along [-1 1 0] direction. These peaks are allowed in the noncollinear type-I/III structure. Figure 2.13 shows the observed *L* dependence of these peaks with and without a magnetic field at 5 K. With application of a 7-T magnetic field, the zero-field intensities of (0.5, 0.5, 1) and (0.5, 0.5, 3) disappear. This indicates that the magnetic structure of a superconducting $Nd_{1.85}Ce_{0.15}CuO_4$ is transformed from the noncollinear structure type-I/III to the collinear structure domain-I by a magnetic field applied along [-1 1 0] direction, just as it does in the parent Nd_2CuO_4 (Fig. 2.5). The allowed magnetic peaks in the collinear domain-I satisfy the condition $H+K+L$ = odd, for example (0.5, 0.5, 2) and (0.5, 0.5, 4). The critical magnetic field for the spin-flop transition is determined by the field dependence of integrated intensity at (0.5, 0.5, 3), which is marked by an arrow in Fig. 2.13(f). We can also determine the Néel temperature of this sample using this spin-flop transition. Figure 2.13(e) shows the temperature dependence of the scattering at (0.5, 0.5, 3) at a zero-field and 7 T. At 7 T, the intensity shows no temperature dependence below 65 K, indicating that this scattering is nonmagnetic. Comparison of a zero-field and 7-T data gives the Néel temperature of ~ 38 K at 0 T, a value larger than T_c but substantially smaller than that of other $Nd_{2-x}Ce_xCuO_4$ samples [56, 57].

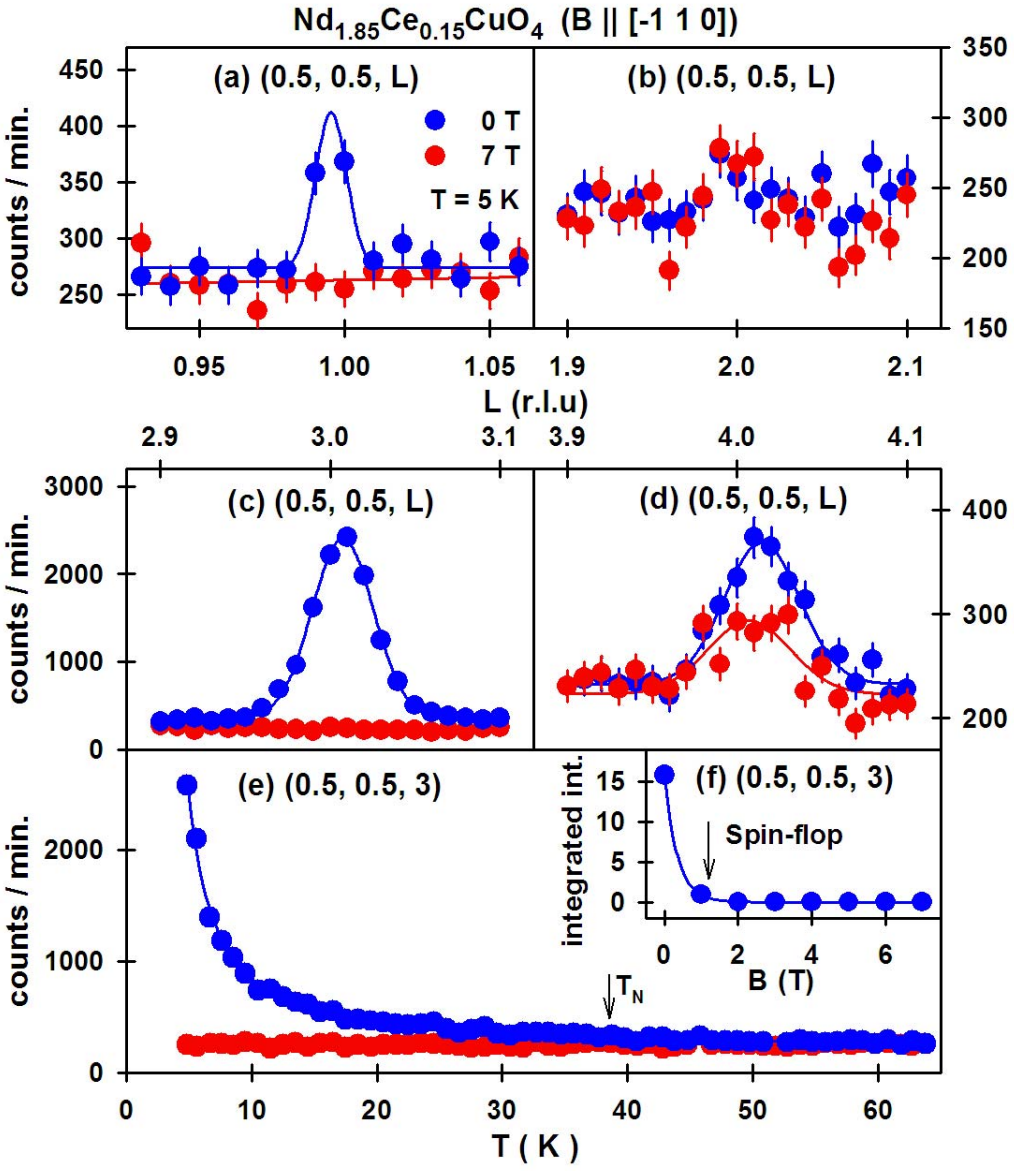

Fig. 2.13 Effect of a **B** || *ab*-plane on (0.5, 0.5, *L*) antiferromagnetic Bragg peaks. (a)-(d) Scans along *L* direction of (0.5, 0.5, *L* = 1, 2, 3, 4) with 0 T and 7 T at 5 K. (e) Intensity of (0.5, 0.5, 3) as a function of temperature with 0 T and 7 T. (f) Integrated intensity of (0.5, 0.5, 3) as a function of field.

Table 2.3 Magnetic structure factor calculations for the noncollinear type-I/III and the collinear domain-I structure in $Nd_{1.85}Ce_{0.15}CuO_4$. F_{nc} and F_c are noncollinear and collinear structure factor, respectively.

$(H\ K\ L)$	$\lvert F_{nc}\rvert^2$	$\lvert F_c\rvert^2$
(0.5, 0.5, 1)	$32.0\ p^2\ (f_{cu} M_{cu} - 1.1015\ f_{nd} M_{nd})^2$	0
(0.5, 0.5, 2)	$14.6\ p^2\ (f_{cu} M_{cu} - 0.5384\ f_{nd} M_{nd})^2$	$29.2\ p^2\ (f_{cu} M_{cu} - 0.5384\ f_{nd} M_{nd})^2$
(0.5, 0.5, 3)	$32.0\ p^2\ (f_{cu} M_{cu} + 1.7426\ f_{nd} M_{nd})^2$	0
(0.5, 0.5, 4)	$24.6\ p^2\ (f_{cu} M_{cu} - 1.5366\ f_{nd} M_{nd})^2$	$49.2\ p^2\ (f_{cu} M_{cu} - 1.5366\ f_{nd} M_{nd})^2$

The magnetic structure factor calculations for the noncollinear type-I/III structure and the collinear domain-I in $Nd_{1.85}Ce_{0.15}CuO_4$ are compared in Table 2.3. It shows that the magnetic intensity in the collinear domain-I would be twice that in the noncollinear type-I/III structure, if there were no change in Cu^{2+} and Nd^{3+} moments. However, Fig. 2.13(b) and (d) show that (0.5, 0.5, 2) peak does not change with a field of 7 T, but (0.5, 0.5, 4) peak decreases with a field of 7 T. This indicates that the Nd^{3+} moments are polarized by a magnetic field, since the Nd^{3+} moments contribute negatively to the Cu^{2+} moments in the magnetic structure factor calculation. The intensity decrease at (0.5, 0.5, 4) is much bigger than that at (0.5, 0.5, 2), consistent with much bigger coefficient of Nd^{3+} at (0.5, 0.5, 4).

Even though the magnetic field effect results indicate that the Nd^{3+} moments are polarized by a *ab*-plane magnetic field, we believe that the enhancement of antiferromagnetic order by a *c*-axis magnetic field is the consequence of the suppression of superconductivity. This conclusion is based on the *c*-axis field effect on the parent Nd_2CuO_4 and as-grown $Nd_{1.85}Ce_{0.15}CuO_4$. Both samples show no field effect on the antiferromagnetic order.

2.8 Magnetic field effect on the impurity phase of cubic $(Nd,Ce)_2O_3$ and its separation from the field effect on the superconducting $Nd_{1.85}Ce_{0.15}CuO_4$ using a horizontal field magnet

To demonstrate that the field-induced effect on the antiferromagnetic order indeed arises from the suppression of superconductivity, we not only need to show that similar field-induced effects are not there in the parent compound and as-grown nonsuperconducting $Nd_{1.85}Ce_{0.15}CuO_4$, but we also have to rule out other spurious effects. One of spurious effects is the formation of cubic $(Nd,Ce)_2O_3$ as an impurity phase due to the annealing process [60]. Unlike hole-doped materials, the as-grown samples of electron-doped ones are nonsuperconducting. To achieve superconductivity, the annealing process is necessary in electron-doped superconductors. The annealing process also induces a cubic $(Nd,Ce)_2O_3$ as an impurity phase [60].

In general, the impurity phases resulting from a heat treatment should create powder lines unrelated to the original underlying lattice. However, the cubic $(Nd,Ce)_2O_3$ stabilizes as an oriented crystalline lattice in $Nd_{1.85}Ce_{0.15}CuO_4$ crystal because of its close lattice parameter match to the tetragonal planes of $Nd_{1.85}Ce_{0.15}CuO_4$. The lattice constant of impurity is about $2\sqrt{2}$ larger than the planner lattice constant of tetragonal $Nd_{1.85}Ce_{0.15}CuO_4$. This lattice match with $Nd_{1.85}Ce_{0.15}CuO_4$ in the CuO_2 plane gives reflections at (*H, K,* 0) of $Nd_{1.85}Ce_{0.15}CuO_4$. Since $(Nd,Ce)_2O_3$ has a cubic crystal structure, its lattice parameter is ~10 % smaller than the *c*-axis lattice parameter of $Nd_{1.85}Ce_{0.15}CuO_4$. This lattice mismatch of impurity gives incommensurate peaks along *L* direction. The reflections of $(Nd,Ce)_2O_3$ $(h, k, l)_c$ can be expressed in $Nd_{1.85}Ce_{0.15}CuO_4$ notation by the relation $(H, K, L) = ((h-k)/4, (h+k)/4, 1.1l)_c$. The relationship of the Miller indices between $Nd_{1.85}Ce_{0.15}CuO_4$ and $(Nd,Ce)_2O_3$ is described in Fig. 2.14(a) and (b) using real space and reciprocal space. Therefore, looking along the *L* direction is the only way to separate the impurity peaks from the $Nd_{1.85}Ce_{0.15}CuO_4$ peaks.

To identify the structural impurity peaks, we aligned the superconducting crystal in [*H* 0 *L*] and [*H H L*] zones. Figure 2.14(c) and (d) show the *c*-axis scans along [0.5 0 *L*] and [1.5 1.5 *L*]

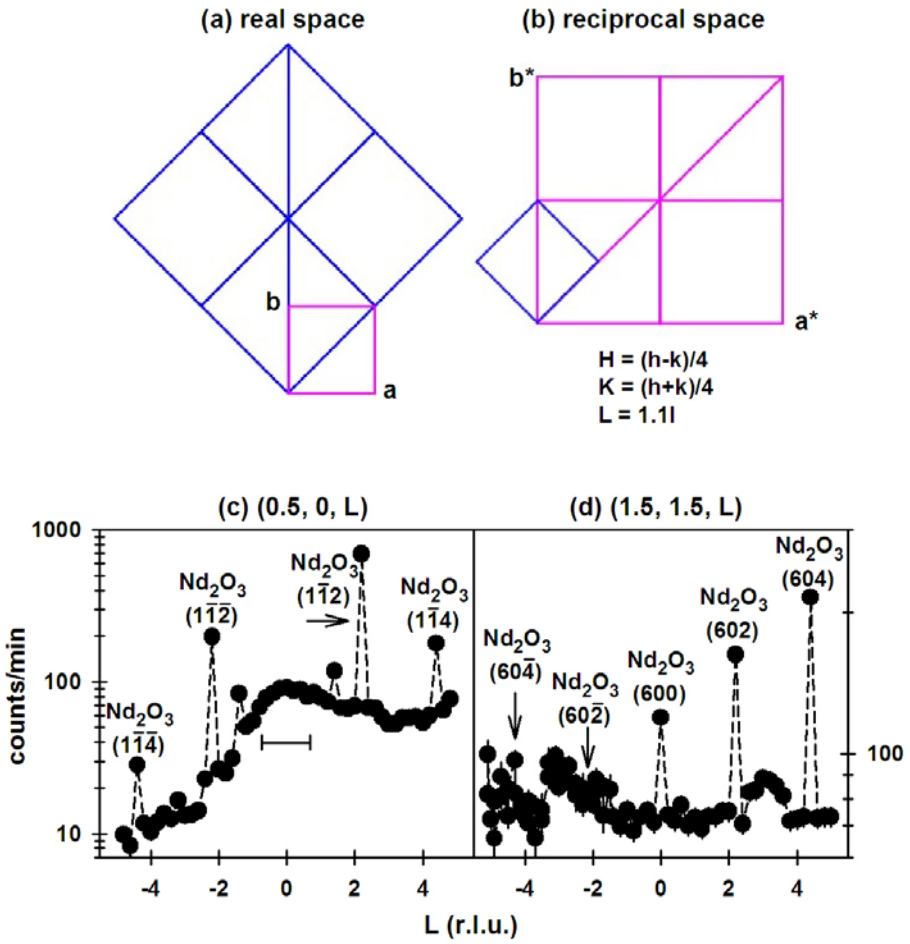

Fig. 2.14 The relationship of the Miller indices between $Nd_{1.85}Ce_{0.15}CuO_4$ and $(Nd,Ce)_2O_3$ and *L* scans. (a)-(b) Real space and reciprocal space of $Nd_{1.85}Ce_{0.15}CuO_4$ and $(Nd,Ce)_2O_3$. The pink is unit cell for $Nd_{1.85}Ce_{0.15}CuO_4$ and the blue is for $(Nd,Ce)_2O_3$. (c) *L* scan along [0.5 0 *L*] direction at room temperature. In addition to the well marked $(Nd,Ce)_2O_3$ peaks, a broad diffusive peak with a fullwidth at half-maximum of $\Delta L = 1.1$ (r.l.u.) is observed at $L = 0$. This diffusive peak is coming from the superstructure similar to (0.5, 0.5, 0) peak. (d) *L* scan along [1.5 1.5 *L*] direction at room temperature. $(Nd,Ce)_2O_3$ peaks are marked by arrows. Since no broad diffusive peak is found at $L = 0$, most of the intensity at (1.5, 1.5, 0) is due to $(Nd,Ce)_2O_3$.

directions at room temperature. Both scans show sharp Bragg peaks of the impurity incommensurate with $Nd_{1.85}Ce_{0.15}CuO_4$, indicating that the impurity forms a 3D long range order in the matrix of $Nd_{1.85}Ce_{0.15}CuO_4$. Bragg intensity comparison shows that the volume fraction of the impurity is 0.1~1 %.

Since Nd^{3+} in $(Nd,Ce)_2O_3$ has a magnetic ground state, the application of a magnetic field will induce paramagnetic scattering from the impurity phase at antiferromagnetic positions of $Nd_{1.85}Ce_{0.15}CuO_4$. Therefore, it is important to check the field-induced antiferromagnetism in the superconducting sample (section 2.6) is related to the suppression of superconductivity, not from the impurity effect. The 2D antiferromagnetic order gives magnetic scattering centered at (0.5, 0.5, 0) and its equivalent positions. We also found the magnetic scattering at (0.5, 0, 0) type positions. The (0.5, 0, 0) peak comes from the impurity $(1, 1, 0)_c$ reflection, while the (0.5, 0.5, 0) peak comes from both antiferromagnetism of $Nd_{1.85}Ce_{0.15}CuO_4$ and paramagnetic scattering of the impurity. We applied a magnetic field along a *c*-axis to study how these two types of peaks behave in a magnetic field. Figure 2.15 shows the **Q** scans and its integrated intensities of these peaks as a function of magnetic field. The (0.5, 0, 0) peak increases up to 8 T and then it saturates at higher fields, while the (0.5, 0.5, 0) peak increases up to B_{c2} and then it decreases above B_{c2}. The field-dependent behavior of (0.5, 0, 0) is consistent with field-induced paramagnetic scattering from the impurity $(Nd,Ce)_2O_3$. In general, rare-earth oxides such as Nd_2O_3 and Er_2O_3 have a bixbyite structure with 32 rare-earth ions in a cubic unit cell, and order antiferromagnetically at low temperature [61]. Since the scattering at (0.5, 0.5, 0) is temperature independent at 5 K (Fig. 2.11(a)), it is safe to assume that the $(Nd,Ce)_2O_3$ impurity is in the paramagnetic state at this temperature. In the paramagnetic state of $(Nd,Ce)_2O_3$, a magnetic field will induce a net moment given by a Brillouin function, and the field-induced moment should saturate in the high magnetic field limit. The decrease of field-induced magnetic scattering of (0.5, 0.5, 0) above B_{c2} can be explained by canting of Cu/Nd moments towards the field direction.

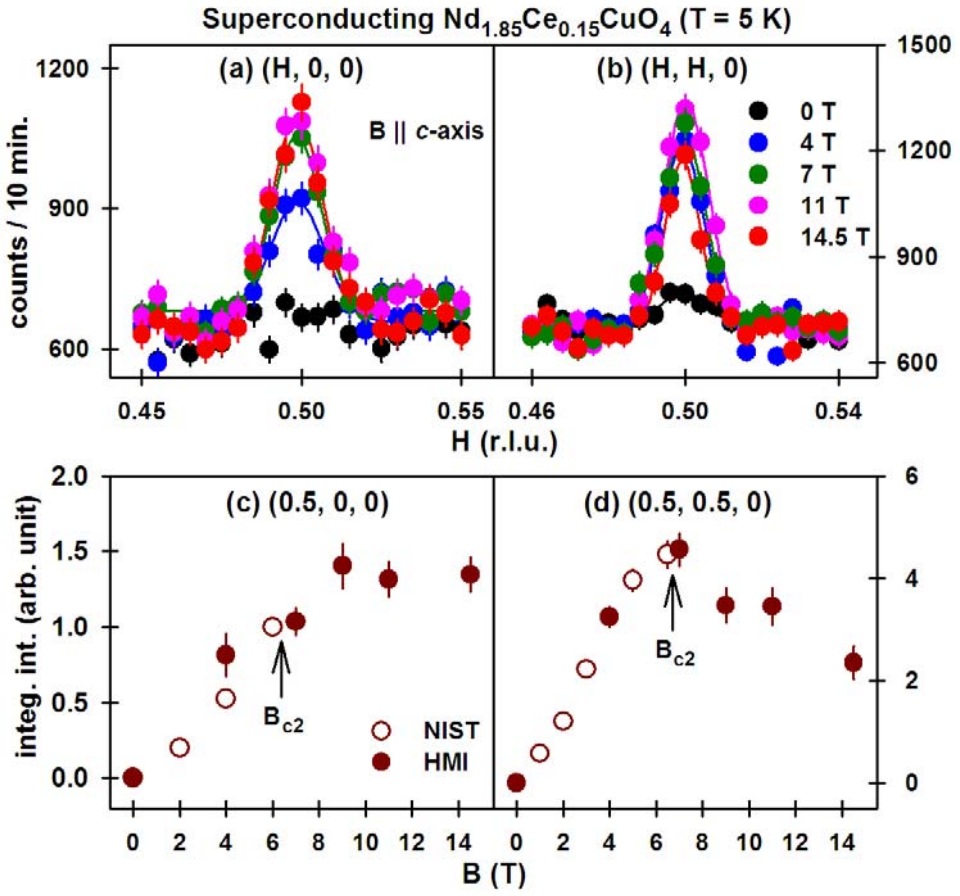

Fig. 2.15 The magnetic field effect on (0.5, 0, 0) and (0.5, 0.5, 0) peaks. (a)-(b) **Q** scans around (0.5, 0, 0) and (0.5, 0.5, 0) with different magnetic fields at 5 K. (c)-(d) Integrated intensities of (0.5, 0, 0) and (0.5, 0.5, 0) as a function of magnetic field at 5 K. The upper critical field B_{c2} is marked by arrow.

In conclusion, even though (0.5, 0.5, 0) has a paramagnetic scattering contribution from the impurity phase, its different field-induced behavior from (0.5, 0, 0) which has impurity contribution only supports that the field-induced antiferromagnetism in section 2.6 is a generic property of $Nd_{1.85}Ce_{0.15}CuO_4$ and is not from impurity effect.

There is another way to separate the impurity effect from the $Nd_{1.85}Ce_{0.15}CuO_4$ magnetic field effect. Even though the lattice parameters of the cubic impurity $(Nd,Ce)_2O_3$ are lattice matched with $Nd_{1.85}Ce_{0.15}CuO_4$ in the *ab*-plane, its *c*-axis lattice constant is about 10 % smaller than that of $Nd_{1.85}Ce_{0.15}CuO_4$. This lattice constant mismatch gives incommensurate scattering in $Nd_{1.85}Ce_{0.15}CuO_4$ at positions such as (0.5, 0.5, *L*) *L* = 2.2, 4.4, and so on. Therefore, one can separate the impurity scattering by simply performing a *c*-axis aligned magnetic field experiment at non-zero integer *L* positions, such as *L* = 1, 2, and 3, since such scattering can only arise from $Nd_{1.85}Ce_{0.15}CuO_4$. To do this, we performed an experiment at HMI using the HM2 horizontal field magnet to probe the antiferromagnetic order at (0.5, 0.5, 3) position. The sample is aligned in the [*H H L*] zone and a magnetic field is applied along a *c*-axis. Figure 2.16 shows the *c*-axis magnetic field effect on the antiferromagnetic position of $Nd_{1.85}Ce_{0.15}CuO_4$ at (0.5, 0.5, 3) and the impurity reflection at $(2, 0, 4)_c$, which is at (0.5, 0.5, 4.4) in $Nd_{1.85}Ce_{0.15}CuO_4$. The antiferromagnetic reflection (0.5, 0.5, 3) of $Nd_{1.85}Ce_{0.15}CuO_4$ shows clearly the field-induced effect (Fig. 2.16(a), (c) and (d)), while the impurity phase at (0.5, 0.5, 4.4) shows no observable field-induced effect (Fig. 2.16(b)). These results unambiguously demonstrate that the application of a *c*-axis aligned magnetic field enhances the residual antiferromagnetic order.

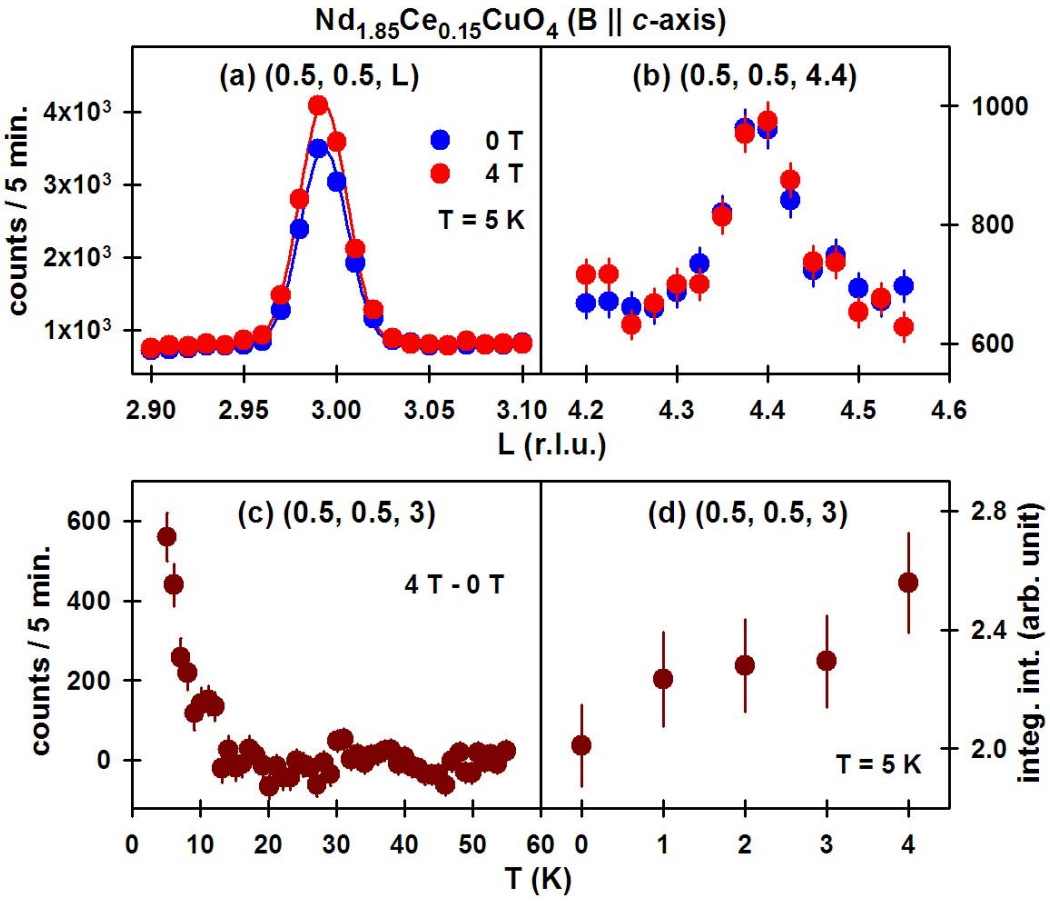

Fig. 2.16 A *c*-axis field effect on the antiferromagnetic order of $Nd_{1.85}Ce_{0.15}CuO_4$ and impurity $(Nd,Ce)_2O_3$. (a) The *L* scan at antiferromagnetic position (0.5, 0.5, 3) of $Nd_{1.85}Ce_{0.15}CuO_4$ shows that a *c*-axis magnetic field enhances the antiferromagnetic order. (b) The impurity reflection $(2, 0, 4)_c$, which is at (0.5, 0.5, 4.4) in $Nd_{1.85}Ce_{0.15}CuO_4$ shows no field effect. (c) The net field induced magnetic intensity of (0.5, 0.5, 3) as a function of temperature. (d) Integrated intensity of (0.5, 0.5, 3) as a function of field at 5 K.

Chapter 3: Magnetic field effect on the electron-doped $Pr_{0.88}LaCe_{0.12}CuO_{4\pm\delta}$

3.1 Introduction

The neutron scattering experiments on the electron-doped $Nd_{1.85}Ce_{0.15}CuO_4$ described in chapter 2 confirm that the enhancement of antiferromagnetic order by a *c*-axis magnetic field is related to the suppression of superconductivity. These results combined with the field-induced effects on the hole-doped LSCO [14, 15, 28] suggest that antiferromagnetism competes with superconductivity in high-T_c cuprates.

However, the electron-doped superconductor $Nd_{1.85}Ce_{0.15}CuO_4$ has a complication because of the rare earth Nd^{3+} moment contribution. Therefore to determine whether antiferromagnetism is the competing order in high-T_c cuprates, it is necessary to do systematic studies in another electron-doped system (where the rare earth magnetic moment is negligible) for two reasons. First, the impurity phase from the annealing process would show no observable field-induced effect. Second, we can study the inherent nature of field dependence of Cu^{2+} spin correlation without the significant contribution from the rare earth moment at low temperature. The single crystals of $Pr_{0.88}LaCe_{0.12}CuO_{4\pm\delta}$ (PLCCO) are perfect for this purpose, since Pr^{3+} has nonmagnetic singlet ground state.

Recent neutron scattering studies on LSCO reveal that two diagonal SDW peaks around (0.5, 0.5, 0) coexist with the 3D antiferromagnetic order in the lightly doped region and survive in the insulating region [8, 9, 10, 11]. At the transition to the superconducting phase, four incommensurate SDW peaks appear with directions parallel to the Cu-O bond direction and coexist with superconductivity in the underdoped region ($0.06 \le x \le 0.12$) [11, 12, 13]. Figure 3.1(b) shows the established phase diagram of LSCO. To study the nature of SDW to superconductivity, several magnetic field experiments have been performed on the hole-doped

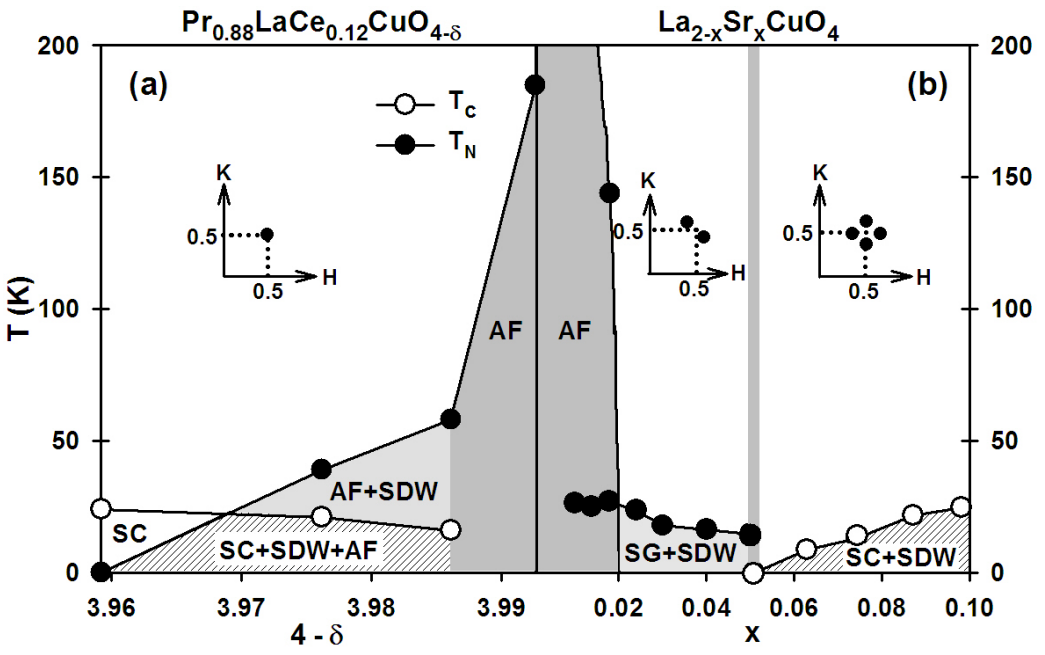

Fig. 3.1 Comparison of phase diagrams between hole-doped LSCO and electron-doped PLCCO. (a) Properties of PLCCO samples investigated in this work. Since the exact oxygen concentrations in our samples are unknown the values of 4-δ are obtained using Fig. 8 of Ref. [45] by assuming that PLCCO samples with the same T_c's as those of $Nd_{1.85}Ce_{0.15}CuO_{4-\delta}$ have the same oxygen content. When superconductivity is first established in PLCCO, a commensurate quasi-2D antiferromagnetic order (SDW) also appears. The data are presented in section 3.4. (b) Phase diagram of LSCO as a function of Sr doping levels. In the insulating phase for $0.02 \leq x \leq 0.05$, two diagonal SDW are observed around (0.5, 0.5, 0). With the appearance of superconductivity at $x \geq 0.05$, two pairs of incommensurate SDW peaks appear around (0.5, 0.5) in the Cu-O direction. The data are from Ref. [8, 9, 10, 11].

LSCO and La_2CuO_{4+y}. The *c*-axis magnetic field enhances the SDW order in the underdoped regime by suppressing superconductivity [14, 15, 28, 35, 36]. However, an *ab*-plane magnetic field does not affect the SDW order and superconductivity [29]. This anisotropic magnetic field effects on the SDW order strongly suggest that antiferromagnetism is a competing order to superconductivity.

To establish whether the role of the SDW is universal feature in the mechanism of high-T_c cuprates, we search for a similar SDW and its magnetic field effect in the electron-doped PLCCO. First we perform systematic studies on the evolution of magnetic and superconducting properties in PLCCO to investigate how superconductivity develops from the antiferromagnetic insulating state in the electron-doped superconductors. For this purpose, we choose a different approach from conventional chemical doping. Instead, we control magnetism and superconductivity by annealing at different temperature at fixed doping level. Since the annealing process, which is required to achieve superconductivity in the electron-doped superconductors, also changes the content of oxygen, we have two parameters. The first parameter is the chemical doping (in this case Ce^{4+} doping), and the oxygen content is the second parameter. Our experiments on PLCCO at a zero-field reveal that the commensurate quasi-2D antiferromagnetic order coexists with superconductivity in the underdoped region and disappears when full superconductivity is achieved. The phase diagram of PLCCO is shown in Fig. 3.1(a) and compared to that of LSCO.

The purpose of this chapter is to describe how we find the quasi-2D antiferromagnetic order and to study its magnetic field effects in the electron-doped PLCCO to establish the universal role of antiferromagnetism in high-T_c cuprates, regardless of hole doping or electron doping.

3.2 Sample preparation and experimental setup

We grew high quality PLCCO single crystals (cylindrical rods weight 0.8~1.5 grams with mosaic < 1°) using the traveling solvent floating zone technique and annealed the samples in pure argon at different temperatures to control the superconducting transition temperatures. The partial substitution of Pr^{3+} with La^{3+} was used to stabilize the crystal growth without introducing significant lattice distortions [62]. We obtained three superconducting PLCCO samples with the onset temperature for bulk superconductivity at T_c = 24 K, 21 K, and 16 K from the magnetic susceptibility measurements (Fig. 3.2(a)). The T_c = 24 K, and 21 K samples are obtained by annealing the as-grown single crystals in pure argon at 970°C and 940°C for 24 hours, respectively. To obtain the T_c = 16 K crystal, the as-grown sample was annealed in pure argon at 915°C for 1 week. The superconducting PLCCO of T_c = 21 K and 16 K are near the phase boundary between the antiferromagnetic and superconducting phases and the T_c = 24 K sample is in the optimally doped regime. We also obtained a nonsuperconducting sample by annealing one of the superconducting T_c = 16 K samples in air at 900°C for 24 hours.

One of the open questions in the electron-doped superconductors is the role of the annealing process to superconductivity [43]. In earlier works, it was postulated that the as-grown nonsuperconducting samples have excess oxygen atoms above copper sites (apical oxygen). These extraneous oxygen atoms have been believed to induce a local disordered potential that localizes doped electrons and therefore prohibits superconductivity [63]. When the annealing process removes these defect oxygen atoms at apical sites, the electrons will not be localized and superconductivity appears. The magnitude of the Hall coefficient in the annealed $Nd_{1.85}Ce_{0.15}CuO_4$ decreases dramatically below T < 100 K, very differently from the as-grown sample [63]. This suggests that the annealing process changes the mobile charge density.

To understand what the annealing process does to our PLCCO samples, we have performed thermogravimetric analysis (TGA) of our samples under the different annealing

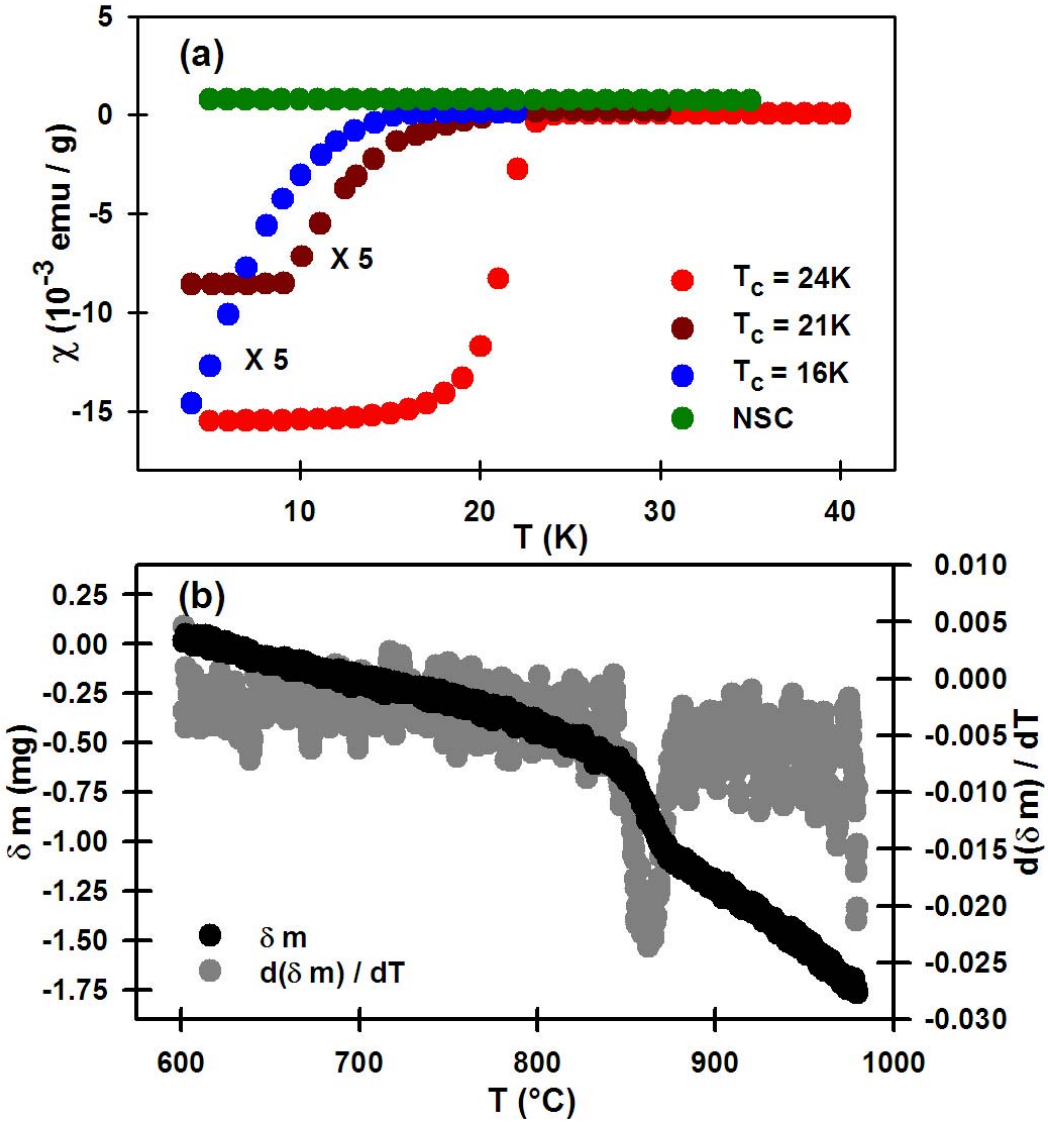

Fig. 3.2 Magnetic susceptibility measurements and mass change of PLCCO samples. (a) Magnetic susceptibility measurements of $Pr_{0.88}La\ Ce_{0.12}CuO_{4\pm\delta}$ single crystals under a small (5~10 Gauss) field in the CuO_2 plane. (b) Temperature dependence of weight change and its derivative of a $Pr_{1.18}La_{0.7}Ce_{0.12}CuO_{4\pm\delta}$ sample in the annealing process.

conditions. Figure 3.2(b) shows the temperature dependence of the weight change for a $Pr_{1.18}La_{0.7}Ce_{0.12}CuO_{4\pm\delta}$ sample during the annealing process. The large drop in weight change shows up as a kink in the data and a sharp dip in its derivative. We interpret this kink to be indicative of the point where the oxygen content becomes the closest to stoichiometry, namely $\delta \approx 0$ [62]. In any case, the TGA data give the most direct evidence that the oxygen content of the sample is reduced during the annealing process.

While TGA analysis indicates the decrease of oxygen content after the reduction process, it is still unclear whether the apical oxygen is removed [64, 65]. Indeed, recent Raman and crystal-field infrared transmission results suggest that instead of removing apical oxygen as originally thought, reduction of optimally doped $Pr_{2-x}Ce_xCuO_{4\pm\delta}$ and $Nd_{2-x}Ce_xCuO_4$ samples actually involves only oxygen in the CuO_2 plane [66, 67]. Clearly, the exact oxygen content and their arrangements in the crystal before and after the reduction need to be sorted out by future studies.

Another issue to be noted regarding the PLCCO material is the relevance of the $(Pr,La,Ce)_2O_3$ impurity phase, which plays the same role in PLCCO as the $(Nd,Ce)_2O_3$ phase in $Nd_{1.85}Ce_{0.15}CuO_4$. To understand the effect of the annealing process on this impurity phase, we have performed systematic synchrotron X-ray diffraction on the as-grown nonsuperconducting, superconducting, and re-oxygenated nonsuperconducting PLCCO samples at the Advanced Photon Source, Argonne National Laboratory. We confirm that the $(Pr,La,Ce)_2O_3$ impurity phase can be produced by the annealing process, but it vanishes after the reoxygenation process [46]. Such a behavior is rather strange, but is understandable if the host PLCCO crystals are slightly Cu deficient. To confirm this possibility, inductively-coupled plasma atomic-emission spectroscopy (ICP-AES) analysis was performed on a batch of crystals that are nominally $Pr_{1.18}La_{0.7}Ce_{0.12}CuO_{4\pm\delta}$. The reference solution is prepared by diluting commercial standard solutions not by the volume but by the weight, which enables us to calculate the cation

concentration of the reference with a high resolution. A piece of the $Pr_{1.18}La_{0.7}Ce_{0.12}CuO_{4\pm\delta}$ crystal (1 mg) is dissolved into a 30 cm^3 of HNO3 (1 Mol/Liter). The analyzed cation ratio of the nominally $Pr_{1.18}La_{0.7}Ce_{0.12}CuO_{4\pm\delta}$ sample was Pr : La : Ce : Cu = 1.20 : 0.68 : 0.12 : 0.97, with a relative error of less than 1 % for each element. This result shows that Cu is indeed deficient by about 3 % in the $Pr_{1.18}La_{0.7}Ce_{0.12}CuO_{4\pm\delta}$ crystal, which is probably also true for PLCCO.

Assuming that the as-grown PLCCO samples are slightly Cu deficient as $Pr_{1.18}La_{0.7}Ce_{0.12}CuO_{4\pm\delta}$, the effect of annealing is then to remove oxygen in PLCCO to form the $(Pr,La,Ce)_2O_3$ impurity and make the remaining crystal structure more perfect for superconductivity. This analysis can potentially explain why the $(Pr,La,Ce)_2O_3$ impurity phase can be reversibly produced [46].

Our neutron scattering measurements were performed on the HB-1A, HB-1, and HB-3 triple-axis spectrometers at the high-flux-isotope reactor (HFIR), Oak Ridge National Laboratory (ORNL) and on the E4 two-axis diffractometer and E1 triple-axis spectrometer at the Berlin Neutron Scattering Center, Hahn-Meitner-Institute (HMI). The magnetic field effect experiments on the superconducting samples of T_c = 24 K, 21 K, and 16 K and the nonsuperconducting sample (T_N = 186 K) were carried out at HFIR using a 7-T vertical field superconducting magnet. The collimations were 48′-40′-sample-40′-102′ (full-width at half-maximum) from the reactor to the detector and the final neutron energies were fixed at either E_f = 14.6 meV or 13.5 meV. For high magnetic field experiments, we used the 14.5-T vertical field superconducting magnet (VM1) at HMI. The collimations were a 40′-40′-sample-40′ collimation, and a fixed neutron final energy was 13.6 meV. A pyrolytic graphite (PG) monochromator and PG analyzer were used, and PG filters were placed in front of the sample to remove higher order contaminations from the incident beam.

We use elastic neutron scattering to probe the antiferromagnetic order and label the momentum transfer $\mathbf{Q} = (q_x, q_y, q_z)$ in $Å^{-1}$ and specify the reciprocal space positions (H, K, L) =

(q_x $a/2\pi$, q_y $a/2\ \pi$, q_z $c/2\ \pi$) in reciprocal lattice units (r.l.u.) appropriate for the tetragonal unit cells of PLCCO (space group I4/mmm, $a = b = 3.98$ and $c = 12.27$ Å). Here a and c are in-plane and out-of -plane lattice constants, respectively.

The crystals were aligned in two different geometries, [*H K 0*] and [*H H L*] scattering planes. A vertical magnetic field was applied along a *c*-axis direction in the former scattering plane, and it was applied along the [-1 1 0] direction (**B** || ab-plane) in the later case. The [*H H L*] geometry was also used to search for the quasi-2D antiferromagnetic order at a zero-field using a two-axis energy integrated mode. This geometry is also used in the studies of a field-induced effect on the impurity phase and a field-induced spin-flop transition. In the [*H K 0*] geometry, we study a *c*-axis magnetic field-induced effect on the superconducting and nonsuperconducting PLCCO. The anisotropy of the field-induced effects can be determined by comparing the results in these two geometries, since the magnetic field along a *c*-axis suppresses superconductivity much more strongly than that for the same field in the *ab*-plane.

3.3 Magnetic structure

The parent compound Pr_2CuO_4 has a body-centered tetragonal structure with space group I4/mmm [68]. The spins of Cu^{2+} ions have the antiferromagnetic ordering in the CuO_2 plane due to the strong in-plane exchange interaction. The orientation of Cu^{2+} spins in adjacent planes is noncollinear governed by weak pseudo-dipolar interaction between planes, since the exchange field on each copper ion by neighboring planes is canceled out due to the body-centered tetragonal crystal symmetry [51, 68]. The spins at (0, 0, 0) and (0.5, 0.5, 0.5) positions are along the [1 0 0] and [0 -1 0] directions, respectively (Fig. 3.3(a)). In this magnetic structure, the antiferromagnetic Bragg peak at (0.5, 0.5, 0) is disallowed. The allowed magnetic Bragg peaks are at (0.5, 0.5, L) (L = 1, 2, 3, ···) and (0.5, 1.5, L) (L = 0, 1, 2, 3, ···) marked as solid dots in Fig.

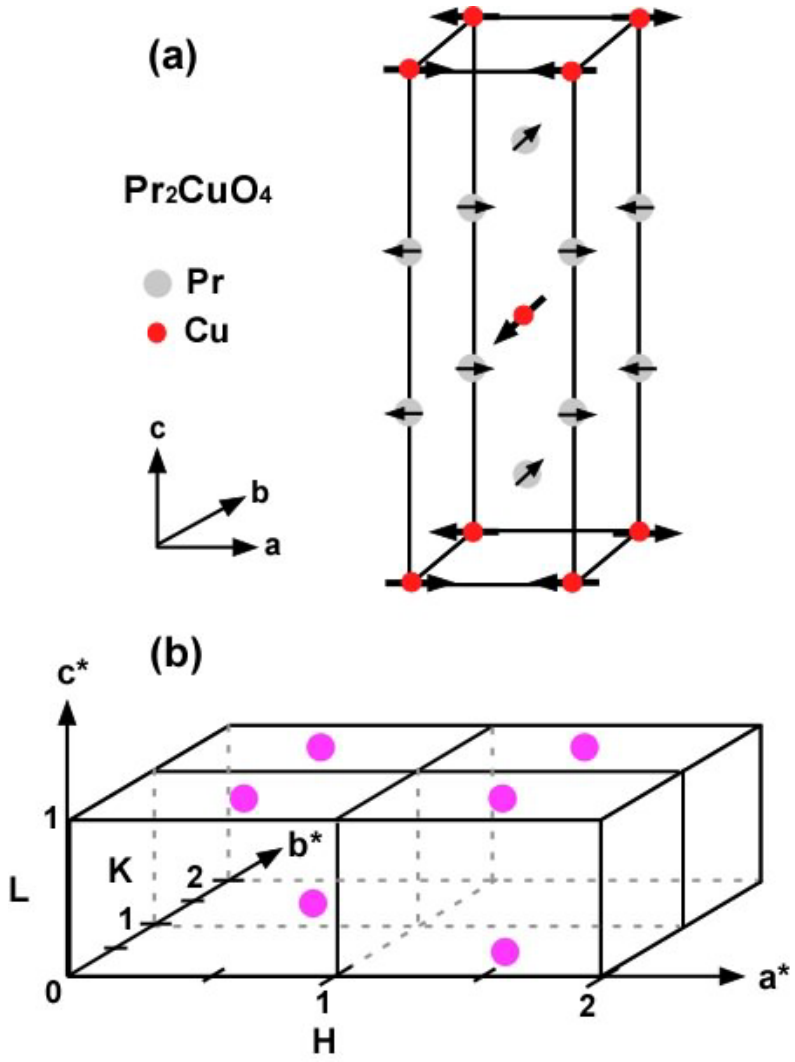

Fig. 3.3 Magnetic structure and expected antiferromagnetic peaks in Pr_2CuO_4. (a) The noncollinear spin structure of Pr_2CuO_4. Oxygen atoms are omitted for simplicity. Small moments at Pr^{3+} ions induced by the Cu^{2+} moment ordering at low temperature have antiferromagnetic coupling with neighboring Cu^{2+} moments along the *c*-axis. (b) Allowed antiferromagnetic Bragg peaks from the noncollinear magnetic structure in (a). Note that (0.5, 0.5, 0) peak is not allowed.

3.3(b).

We performed neutron diffraction measurements at a zero-field on the antiferromagnetic Bragg peaks (0.5, 0.5, *L*) to determine the magnetic structure of the superconducting PLCCO sample with T_c = 16 K. In principle, one cannot uniquely determine the spin structure of PLCCO based on the magnetic intensities at (0.5, 0.5, *L*) alone. However, since the spin structure of $Pr_{2-x}Ce_xCuO_4$ at all Ce^{4+} doping levels is noncollinear as depicted in Fig. 3.3(a) [68], one would expect a similar magnetic structure in PLCCO because substitution of La^{3+} for Pr^{3+} will weaken the pseudo-dipolar interactions but not diminish it.

Figure 3.4 shows the integrated intensities at (0.5, 0.5, *L*) (*L* = 1, 2, 3, 5) as a function of temperature. The integrated magnetic intensities of these peaks increase with decreasing temperature below Néel temperature of 58 K and saturate at low temperature. The saturation of magnetic intensities of (0.5, 0.5, *L*) reflections indicates that the Pr^{3+} moment contribution at low temperature is negligible in the superconducting PLCCO sample. For the superconducting $Nd_{1.85}Ce_{0.15}CuO_4$ case the intensity of (0.5, 0.5, 3) increases dramatically at low temperature due to Nd^{3+} moment contribution (chapter 2). Therefore, we can study inherent Cu^{2+} spin behavior in an applied magnetic field without the rare earth moment contribution.

In order to check if the magnetic integrated intensities of (0.5, 0.5, *L*) is consistent with the intensity calculations of proposed noncollinear structure in Fig. 3.3(a), we calculated the magnetic structure factor. Table 3.1 shows the magnetic structure factor calculation at (0.5, 0.5, *L*) reflections for the noncollinear structure and the collinear domain-I in PLCCO. The integrated intensities of magnetic Bragg peaks are proportional to $|F_{nc}|^2$ (Eq. 1-11 in chapter 1). The induced Pr^{3+} moment contributes positively to the intensity of (0.5, 0.5, 1) and (0.5, 0.5, 2), but negatively to the intensity of (0.5, 0.5, 3) (Table 3.1). Therefore, the temperature dependent measurements of (0.5, 0.5, *L*) should show deviations from the power law fits when the induced Pr^{3+} moment becomes significant [68]. In addition, the (0.5, 0.5, 5) peak should exhibit only the temperature

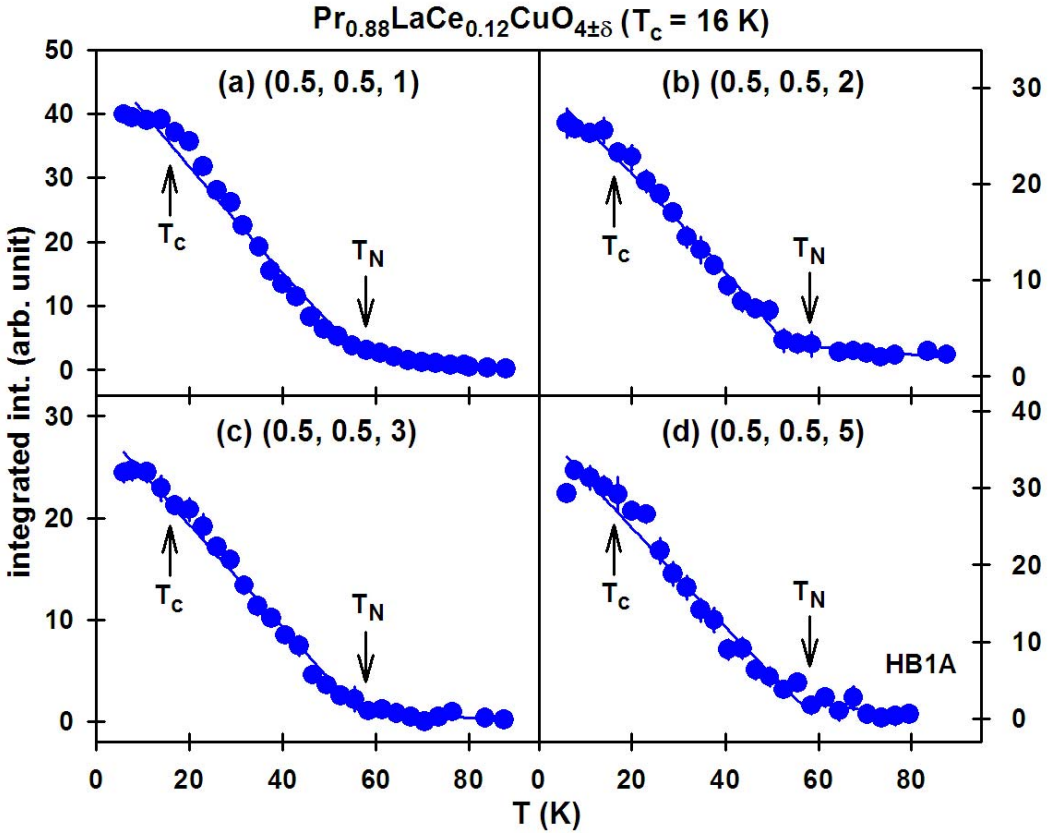

Fig. 3.4 Integrated intensities at (0.5, 0.5, L) for the T_c = 16 K superconducting PLCCO sample as a function of temperature. The solid lines are power law fit. The arrows indicate T_c and T_N, respectively.

Table 3.1 Magnetic structure factor calculations for the noncollinear structure $|F_{nc}|^2$ and the collinear domain-I structure $|F_c|^2$ in PLCCO. $f_{cu,pr}$ and $M_{cu,pr}$ are magnetic form factors and ordered magnetic moments for Cu^{2+} and Pr^{3+} ions, respectively.

(*H, K, L*)	$\|F_{nc}\|^2$	$\|F_c\|^2$
(0.5, 0.5, 0)	0	0
(0.5, 0.5, 1)	$32.0\, p^2\, (f_{cu} M_{cu} + 0.5310\, f_{pr} M_{pr})^2$	0
(0.5, 0.5, 2)	$14.6\, p^2\, (f_{cu} M_{cu} + 0.2391\, f_{pr} M_{pr})^2$	$29.2\, p^2\, (f_{cu} M_{cu} + 0.2391\, f_{pr} M_{pr})^2$
(0.5, 0.5, 3)	$32.0\, p^2\, (f_{cu} M_{cu} - 0.8196\, f_{pr} M_{pr})^2$	0
(0.5, 0.5, 4)	$24.6\, p^2\, (f_{cu} M_{cu} + 0.7500\, f_{pr} M_{pr})^2$	$49.2\, p^2\, (f_{cu} M_{cu} + 0.7500\, f_{pr} M_{pr})^2$
(0.5, 0.5, 5)	$32.0\, p^2\, (f_{cu} M_{cu} - 0.0856\, f_{pr} M_{pr})^2$	0

dependence of the Cu^{2+} moment, because there is essentially no Pr^{3+} moment contribution to this reflection (Table 3.1). Since all magnetic integrated intensities at (0.5, 0.5, *L*) show similar temperature dependence as (0.5, 0.5, 5) (Fig. 3.4), we conclude that the induced Pr^{3+} moment is negligible above 4 K in the T_c = 16 K PLCCO. The integrated intensity comparison of (0.5, 0.5, *L*) peaks to the calculated intensities confirms that the superconducting sample has the same noncollinear spin structure as that of the parent Pr_2CuO_4.

3.4 Evolution of magnetic and superconducting properties at a zero-field

To investigate how superconductivity develops from the antiferromagnetic insulating state in the electron-doped superconductors, we perform systematic studies on the evolution of magnetic and superconducting properties in PLCCO. Fujita *et al*. studied the phase transition from the antiferromagnetic to superconducting phase in $Pr_{1-x}LaCe_xCuO_4$ by changing the Ce^{4+}

doping level [47]. However, the annealing process required to achieve superconductivity in the electron-doped superconductors also change the oxygen content. The study on the electron-doped $Nd_{1.85}Ce_{0.15}CuO_{4-\delta}$ has shown that the variation of oxygen content can transform from the as-grown nonsuperconducting phase to full superconducting phase [45].

We do not want to change two parameters at the same time in establishing the phase diagram in PLCCO. Therefore, we fixed Ce doping level at x = 0.12, which is close to the phase boundary between the antiferromagnetic and superconducting phases and changed only oxygen content by annealing at different temperatures. The manipulation of the annealing process allows us to control the strength of antiferromagnetism and superconductivity. This approach also avoids additional complications such as disorder associated with conventional chemical substitution. We aligned four crystals (an optimally doped superconductor with T_c = 24 K, two underdoped samples with T_c = 21 K, 16 K, and a nonsuperconductor) in the [*H K 0*] scattering plane. Figure 3.5 shows the **Q** scans around (0.5, 0.5, 0) and (0.5, 1.5, 0) in four samples at different temperatures. For optimally doped sample, neither peak shows any temperature dependence, suggesting no magnetic component (Fig. 3.5(a) and (e)). The structural peaks at these two positions are coming the superstructure and the impurity phase induced by the annealing process [46, 60, 69]. For underdoped and nonsuperconducting samples, the intensity of (0.5, 1.5, 0) increases at low temperature 5 K. The peak at (0.5, 1.5, 0) is expected magnetic peak from the 3D ordered noncollinear structure. The temperature dependence of the (0.5, 1.5, 0) peak shows that the magnetic component is increasing with decreasing T_c (Fig. 3.5(f)-(h)).

To make sure that there is no magnetic scattering in the optimally doped sample, we scan the antiferromagnetic Bragg peaks at (0.5, 0.5, 1) and (0.5, 0.5, 3). The absence of peaks at these positions in Fig. 3.6(a) and (b) confirms this. We also determine the Néel temperature T_N's of underdoped samples and a nonsuperconducting sample from the integrated intensity of (0.5, 1.5, 0) as a function of temperature (Fig. 3.6 (d), (f), and (g)). The relationship between T_N's and T_c's

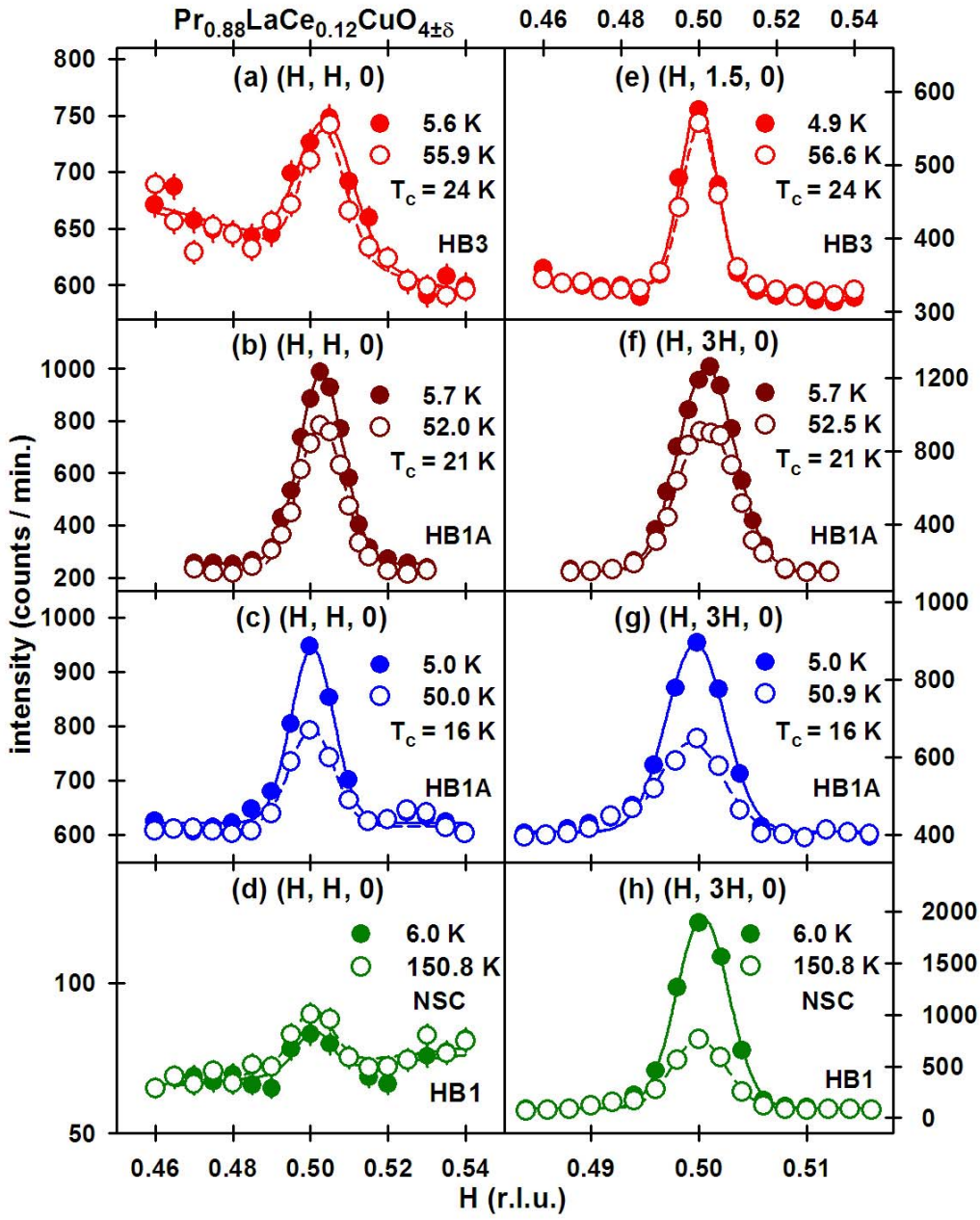

Fig. 3.5 **Q** scans in the [*H K* 0] zone at low and high temperature for the T_c = 24 K, 21 K, 16 K, and nonsuperconducting PLCCO samples. (a)-(d) Scans along the [*H H* 0] direction around (0.5, 0.5, 0). (e)-(h) Similar scans along the [*H* 3*H* 0] direction around (0.5, 1.5, 0). The fitted lines are Gaussian fits to the peaks on the sloping backgrounds.

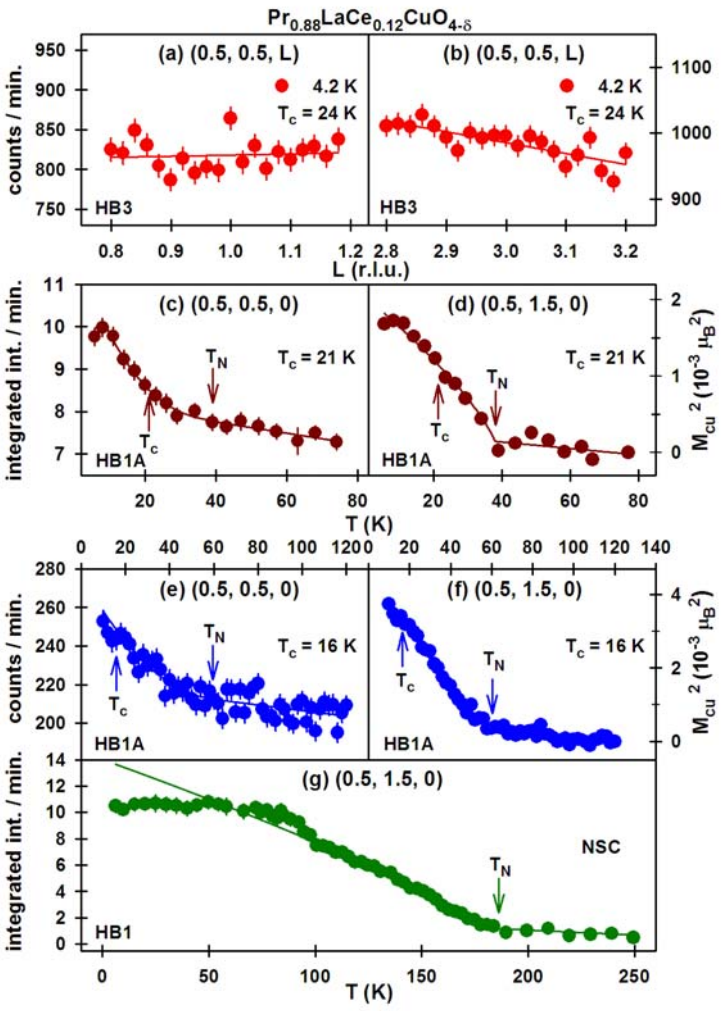

Fig. 3.6 *L* scans and temperature dependence of antiferromagnetic peaks in PLCCO. (a)-(b) *L* scans around (0.5, 0.5, 1) and (0.5, 0.5, 3) for T_c = 24 K at 4.2 K. Temperature dependence of scattering at (0.5, 0.5, 0) and (0.5, 1.5, 0) in the [*H K* 0] plane for (c)-(d) T_c = 21 K, (e)-(f) T_c = 16 K, and (g) nonsuperconducting samples. The solid lines in (d), (f), and (g) are power law fits describing the contribution of Cu^{2+} spins. (d) and (f) show that no measurable Pr^{3+} moment is induced in a superconducting samples. (g) shows that Pr^{3+} moment is induced below 95 K in a nonsuperconducting sample. The decrease of intensity at low temperature is due to the negative contribution of Pr^{3+} moment in magnetic structure factor (See Table 2.1).

of PLCCO crystals is plotted in Fig. 3.7. The T_N decreases linearly with increasing T_c, and it becomes zero when full superconductivity is established. This result indicates that the electron-doped copper oxides are close to a quantum critical point, where the delicate energetic balance between different competing states leads to microscopic inhomogeneity.

It should be noted that the magnetic intensity of (0.5, 1.5, 0) in a nonsuperconducting sample starts to deviate from the power law fitted line at low temperature. This is the indication that the Pr^{3+} moment is induced at low temperature. However, this behavior is missing in the superconducting samples. Since there is no Pr^{3+} moment contribution in the superconducting samples, we can estimate Cu^{2+} moment from the integrated intensity of (0.5, 1.5, 0) by normalizing to the weak structural peak (1, 1, 0). Figure 3.6(d) and (f) show the M_{cu}^2 as a function of temperature in T_c = 21 K and 16 K. The M_{cu} at 5 K increases from 0.04 μ_B to 0.06 μ_B when T_c decreases from 21 K to16 K. In a nonsuperconducting sample M_{cu} is 0.12 μ_B at 97 K above the Pr^{3+} moment ordering temperature.

We also observe the magnetic intensity at (0.5, 0.5, 0) in the underdoped samples in the [*H K 0*] scattering geometry (Fig. 3.5(b)-(c), Fig. 3.6 (c) and (e)). The temperature dependence of this peak is very similar to that of (0.5, 1.5, 0) peak (Fig. 3.6(c) and (e)). We are very interested in this surprising result, because the magnetic scattering at (0.5, 0.5, 0) is forbidden from the noncollinear magnetic structure of PLCCO. This is shown in the temperature independence at this position in the nonsuperconducting sample (Fig. 3.5(d)). More surprisingly, the intensity gain at (0.5, 0.5, 0) is absent in the [*H H L*] scattering plane (Fig. 3.8(a)). A long scan along [0.5 0.5 *L*] direction find no appreciable differences between 6 K and 60 K except at (0.5, 0.5, 1), where the long-range 3D antiferromagnetic order develops (Fig. 3.8(c)). Therefore, the peak at (0.5, 0.5, 0) has different origin from the 3D antiferromagnetic order.

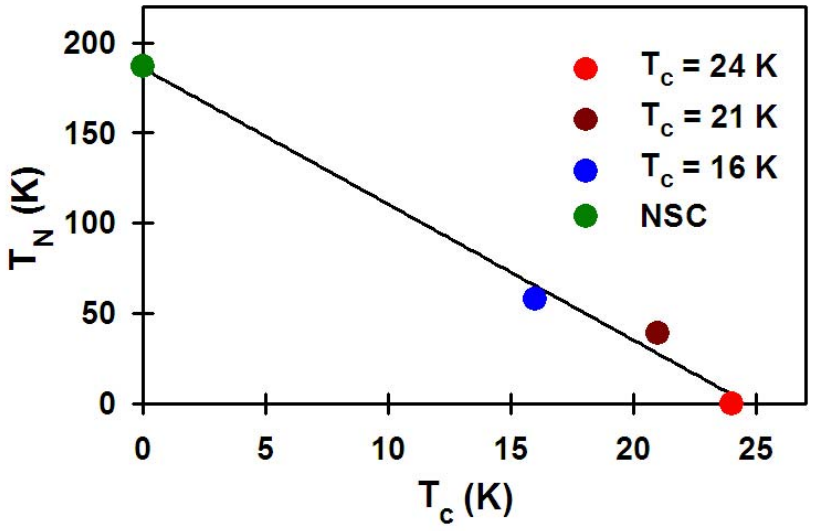

Fig. 3.7 The relationship between T_N and T_c for the PLCCO samples investigated. The T_N is decreasing when the T_c is increasing and it disappears at maximum T_c.

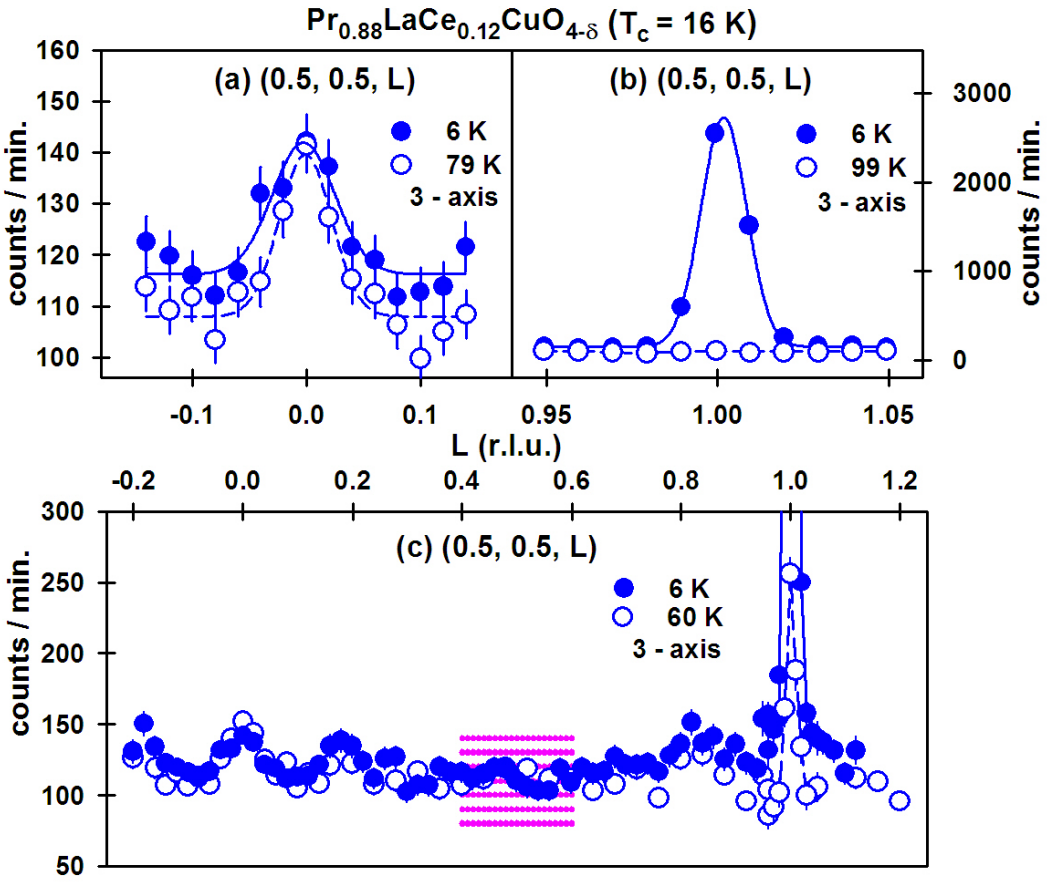

Fig. 3.8 Measurements in the [*H H L*] scattering plane on the T_c = 16 K superconducting sample. *L* scans around (a) (0.5, 0.5, 0) and (b) (0.5, 0.5, 1) at low and high temperatures. (c) Scan along the [0.5 0.5 *L*] direction at 6 K (closed circles) and 60 K (open circles). The pink area is the *L* range probed in the two-axis energy integration mode in Fig. 3.10.

One possible explanation for this behavior of magnetic scattering at (0.5, 0.5, 0) is that the underdoped PLCCO has a quasi-2D antiferromagnetic modulation with strong correlation in the CuO_2 plane but weak coupling along the *c*-axis. Figure 3.9 shows the simplified antiferromagnetic model in real space and expected magnetic scattering in reciprocal space from the model. The quasi-2D magnetic signal is more easily observable in the [*H K* 0] zone than the [*H H L*] zone. This is because the coarse vertical resolution of the triple-axis spectrometer will integrate a much larger region of the *c*-axis magnetic rod in the [*H K* 0] plane than that in the [*H H L*] zone.

The presence of a quasi-2D antiferromagnetic order can be tested using the two-axis energy integrated mode by aligning the outgoing wave vector k_f parallel to the 2D magnetic rod direction (*c*-axis). The two-axis energy integrated mode is depicted in Fig. 3.10(a). In this geometry, we measure the wave-vector-dependent susceptibility that includes the elastic scattering around (0.5, 0.5, *L*) with $0.4 < L < 0.6$ (see pink area in Fig. 3.8(c)). The temperature dependent scattering around (0.5, 0.5, *L*) in the underdoped PLCCO (T_c = 21 K and 16 K) suggests the presence of quasi-2D antiferromagnetic modulation (Fig. 3.10(b) and (c)).

To summarize the results of electron-doped PLCCO at a zero-field, we find that the underdoped superconductors have the quasi-2D antiferromagnetic order in addition to the 3D antiferromagnetic order and superconductivity. The quasi-2D antiferromagnetic order does not exist in an optimally doped superconductor or a nonsuperconductor. The existence of quasi-2D antiferromagnetic order is very similar to the SDW in the hole-doped LSCO. These results have significant importance in searching for universal properties in high-T_c cuprates. To find the role of quasi-2D antiferromagnetic order, the magnetic field effect is studied in section 3.7.

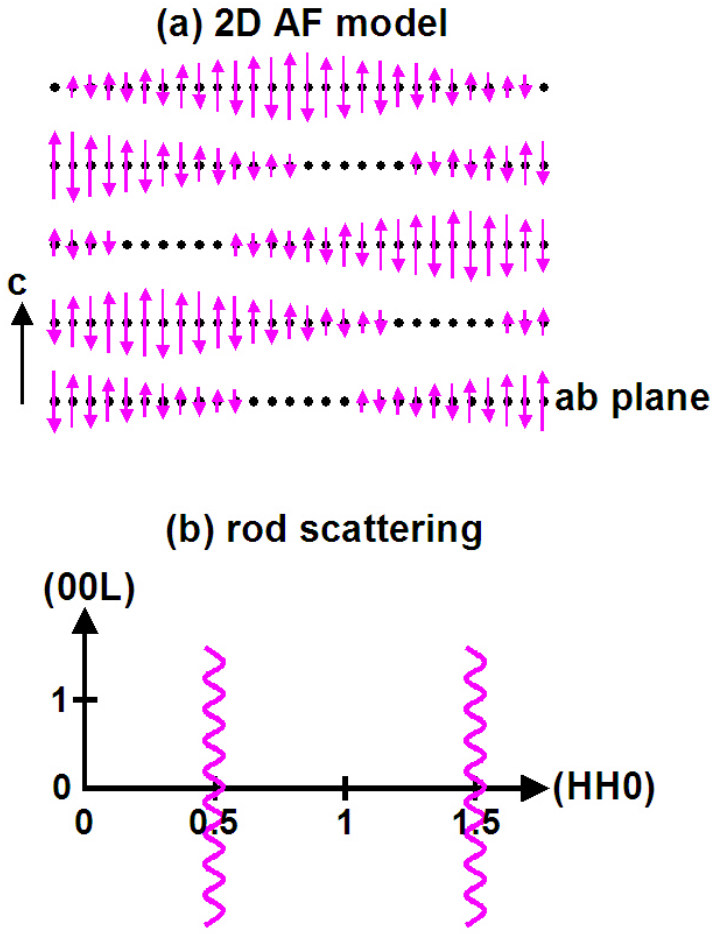

Fig. 3.9 The quasi-2D antiferromagnetic model and its expected magnetic scattering. (a) The simplified quasi-2D antiferromagnetic model in real space. The antiferromagnetic order in the CuO_2 plane is weakly correlated along the *c*-axis. (b) The expected magnetic scattering in the reciprocal space from the model (a).

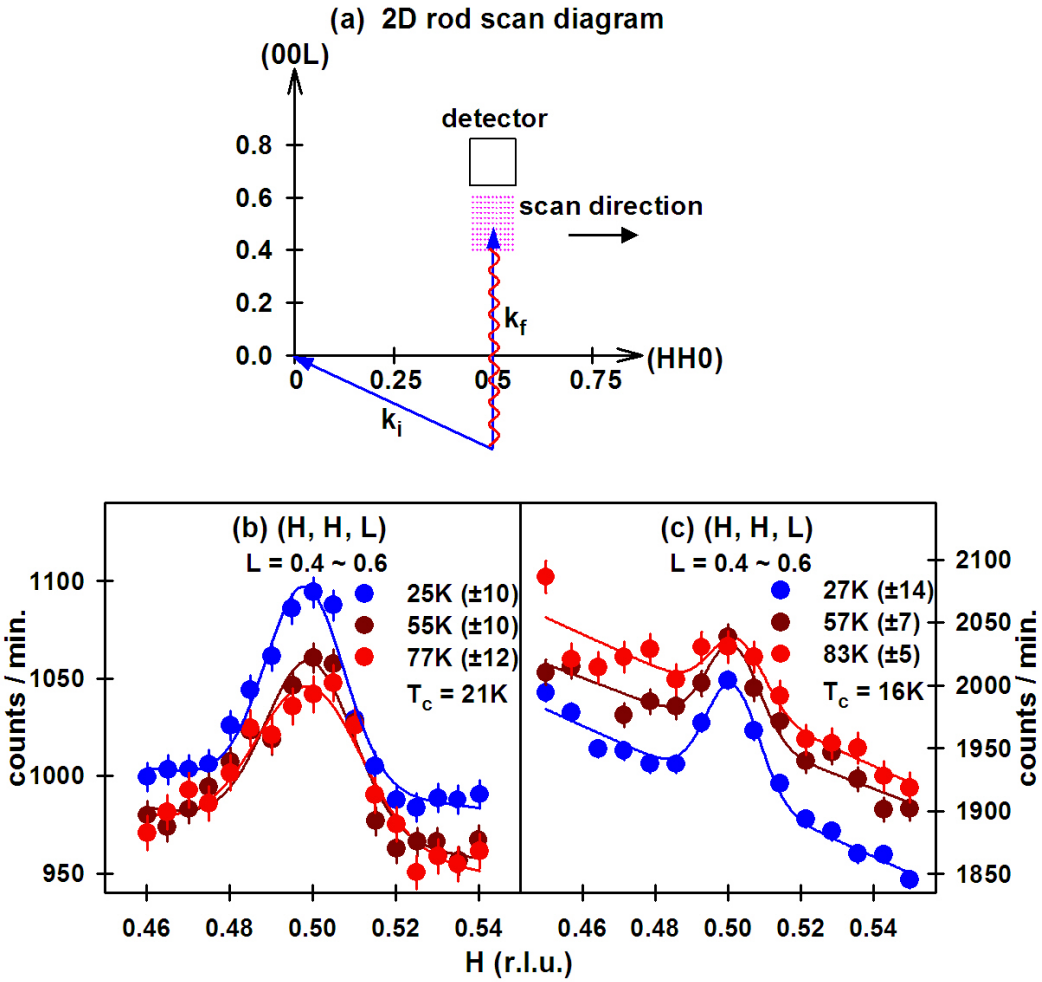

Fig. 3.10 Two-axis energy integrated mode and 2D scans of the underdoped superconductors. (a) The experimental geometry in the two-axis energy integrated mode. (b)-(c) Scans along [H H 0] direction around (0.5, 0.5, L) ($0.4 < L < 0.6$) at different temperatures for underdoped T_c = 21 K and 16 K sample, respectively. The magnetic scattering decreases with increasing temperature for both samples.

3.5 Spin-flop transition on the superconducting and nonsuperconducting $Pr_{0.88}LaCe_{0.12}CuO_{4\pm\delta}$

A magnetic field applied in the [-1 1 0] direction of the CuO_2 planes induces a spin-flop transition from the noncollinear to the collinear spin structure in the electron-doped parent compounds Nd_2CuO_4 and Pr_2CuO_4 (Fig. 2.5) [55, 58]. For the lightly electron-doped $Pr_{1.29}La_{0.7}Ce_{0.01}CuO_{4\pm\delta}$, Lavrov *et al*. discovered that the spin-flop transition is intimately related to the magnetoresistance effect [70]. Similar spin-charge coupling was also found in a separate study on lightly doped $Nd_{1.975}Ce_{0.025}CuO_4$ [71]. The critical magnetic field from the noncollinear to the collinear structure increases with decreasing temperature. For the lightly electron-doped $Pr_{1.29}La_{0.7}Ce_{0.01}CuO_{4\pm\delta}$, the critical magnetic field increases from 0.5 T at 150 K to 2 T at 5 K [70].

To investigate the effect of an in-plane magnetic field on the spin structure of PLCCO, we aligned samples in the [*H H L*] zone and applied a magnetic field along the [-1 1 0] direction. The magnetic structure factor calculation in Table 3.1shows that the magnetic peaks are not allowed at (0.5, 0.5, *L*) with *L* = odd integer in the collinear domain-I spin structure. Therefore, to study spin-flop transition, we probed (0.5, 0.5, 1) and (0.5, 0.5,2) magnetic peaks as a function of field at low temperature. Figure 3.11 summarizes the effect of a magnetic field **B** || [-1 1 0] on (0.5, 0.5, 1) and (0.5, 0.5, 2) magnetic peaks in different samples of PLCCO at 5 K. For the T_c = 21 K sample, a 1-T applied magnetic field diminishes (0.5, 0.5, 1) peak and enhances (0.5, 0.5, 2) magnetic reflection. This indicates that the magnetic structure has been transformed from the noncollinear to the collinear structure by the magnetic field (Fig. 3.11(a) and (d)). This sharp, first-order-like, transition in the T_c = 21 K sample is surprising because the spin-flop transitions for a magnetic field **B** || [-1 1 0] in the lightly doped $Pr_{1.29}La_{0.7}Ce_{0.01}CuO_{4\pm\delta}$ [70], $Nd_{1.975}Ce_{0.025}CuO_4$ [71], Nd_2CuO_4 [55], and Pr_2CuO_4 [68] are gradual and more second-order-like.

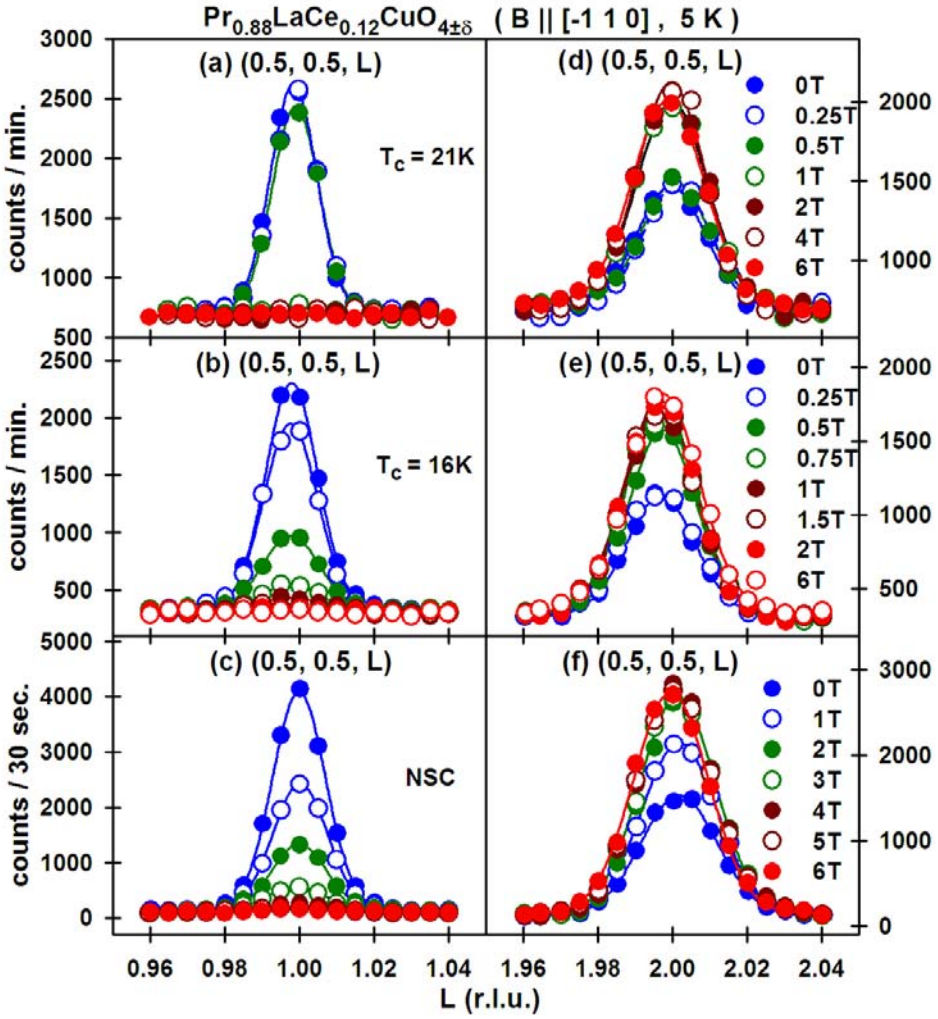

Fig. 3.11 Magnetic scattering around (0.5, 0.5, L) as a function of magnetic field at 5 K for the superconducting and nonsuperconducting samples. (a)-(c) L scans around (0.5, 0.5, 1). (d)-(f) L scans around (0.5, 0.5, 2). The T_c = 21 K sample shows the first-order-like spin-flop transition and the T_c = 16 K and the nonsuperconducting samples display a more gradual second-order-like spin-flop transition. The solid lines are Gaussian fits to the peaks.

To understand how the behavior of spin-flop transition evolves when the superconducting PLCCO is transformed to the antiferromagnetic insulator, we performed similar measurements on another superconductor with lower T_c = 16 K and a nonsuperconductor. The outcome (Fig. 3.11) suggests that the spin-flop transitions become sharper as superconductivity is developed with increasing T_c. This behavior is more clearly shown in the integrated intensities of (0.5, 0.5, 1) and (0.5, 0.5, 2) as a function of increasing field for the three PLCCO samples at 5 K (Fig. 3.12(a)-(c)). The inset in Fig. 3.12(b) shows that a higher Néel temperature T_N requires a larger critical field B_{sp} for the spin-flop transition. Therefore, the critical field B_{sp} decreases with decreasing T_N and reduced Cu^{2+} moment.

From the magnetic structure factor calculations in Table 3.1, we find that the ratio of integrated intensities of (0.5, 0.5, L= even) at the collinear and the noncollinear states is $|F_c(0.5, 0.5, L\text{= even})/F_{nc}(0.5, 0.5, L\text{= even})|^2 = 2$ if the Cu^{2+} and Pr^{3+} moments under a magnetic field are the same as that at a zero-field. Inspection of Fig. 3.11 and 3.12 for (0.5, 0.5, 2) shows that this is indeed the case. Therefore, a moderate magnetic field ($\leq$ 6 T) that causes the spin-flop transition does not induce additional moments on Cu^{2+} and Pr^{3+} sites in the PLCCO samples.

To further determine the effect of a magnetic field on Pr/Cu moments after the spin-flop transition, we measure the temperature dependence of the scattering at (0.5, 0.5, L) (L = 2, 4, 6) for fields just above $\boldsymbol{B}_{sp}$ and at 6 T. This comparison allows us to determine whether the application of additional magnetic field induces Cu/Pr moments in the collinear state of PLCCO after the spin-flop transition. The comparison of integrated intensities at these peaks in Fig. 3.13 shows no appreciable difference between 1.5 T and 6 T data in the temperature range probed. From these, we can conclude that a 6-T in-plane magnetic field does not induce additional Cu/Pr moments for the T_c = 16 K PLCCO sample. This is probably true in all the superconducting samples.

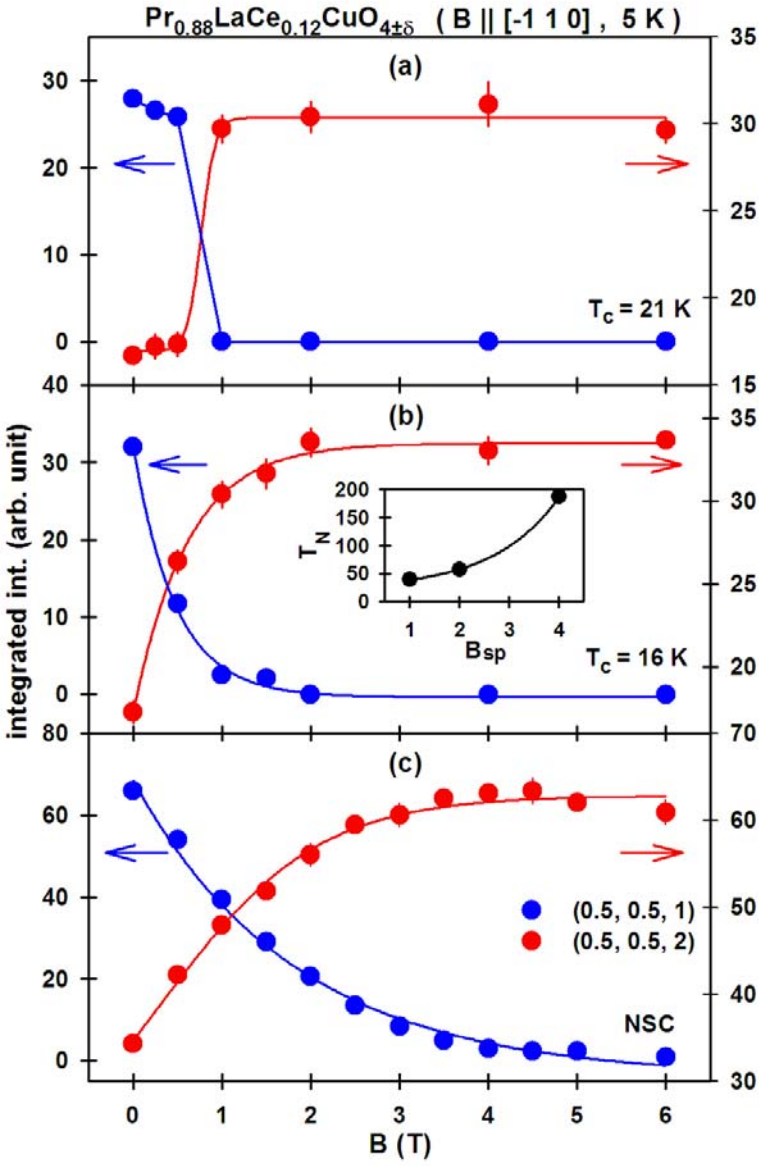

Fig. 3.12 Integrated intensities of (0.5, 0.5, *L*) as a function of a magnetic field for the superconductors and the nonsuperconductor. (a) T_c = 21 K, (b) T_c = 16 K, and (c) nonsuperconducting samples at 5 K. The inset in (b) shows the relationship between Néel temperature and critical field for the spin-flop transition.

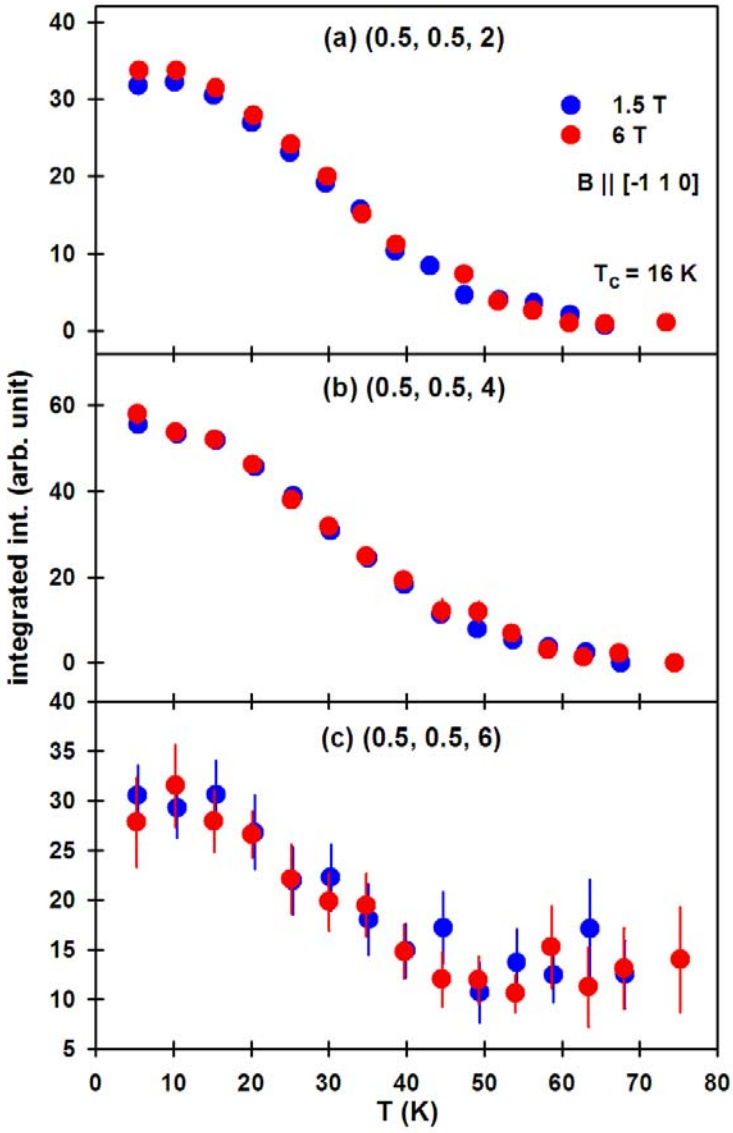

Fig. 3.13 The integrated magnetic intensities of (0.5, 0.5, L) (L = 2, 4, 6) as a function of temperature at 1.5 T and 6 T for the T_c = 16 K PLCCO. The spin-flop transition have occurred above 1.5 T (Fig. 3.12). The negligible changes of the integrated intensities indicate that a 6-T in-plane magnetic field does not affect the Cu^{2+} and Pr^{3+} moment. It transforms the magnetic structure from a noncollinear to a collinear one (Fig. 2.5 in chapter 2).

To see if a larger in-plane magnetic field will affect the Cu/Pr moment, we measured the field-dependence of (0.5, 0.5, 2) and (0.5, 0.5,4) reflections up to 14 T for the T_c = 21 K PLCCO at HMI. The outcome is shown in Fig. 3.14(c)-(e). It clearly indicates that while a 1-T in-plane magnetic field enhances the intensity of (0.5, 0.5, 2) peak due to the spin-flop transition. Increasing the applied magnetic field to 14 T does not induce additional changes in the integrated intensity of (0.5, 0.5, 2) peak at 5 K (Fig. 3.14(c) and (e)). Therefore, a 14-T magnetic field does not alter the Cu/Pr moments within the error of our measurements. This is quite different from the effect of an in-plane magnetic field on $Nd_{1.85}Ce_{0.15}CuO_4$, where the (0.5, 0.5, 2) reflection shows no intensity change and the (0.5, 0.5, 4) intensity decreases under a 7-T magnetic field (Fig. 3.14(a)-(b)) (See chapter 2). For $Nd_{1.85}Ce_{0.15}CuO_4$ case, a 7-T magnetic field **B** || [-1 1 0] not only causes a spin-flop transition, but also induces magnetic moments on the Nd^{3+} sites. The induced Nd^{3+} moments contribute negatively in the magnetic structure factor at these positions (Table 2.3). The significant intensity drop at (0.5, 0.5, 4) compared to that at (0.5, 0.5, 2) under a 7-T magnetic field is because the Nd^{3+} moment contribution is much bigger to the magnetic structure factor at (0.5, 0.5, 4) than at (0.5, 0.5, 2) (Table 2.3). Since PLCCO has negligible field-induced moment contribution from the Pr^{3+}, the field-induced effects here should reveal the inherent Cu^{2+} spin correlations.

3.6 Magnetic field effect on the nonsuperconducting $Pr_{0.88}LaCe_{0.12}CuO_{4\pm\delta}$ and the cubic impurity phase $(Pr,La,Ce)_2O_3$

Since the discovery of a *c*-axis magnetic field-induced effect in $Nd_{1.85}Ce_{0.15}CuO_4$ (chapter 2) [72], there has been much debate concerning the origin of the field-induced effect. While we argue that the observed effects are partially intrinsic to $Nd_{1.85}Ce_{0.15}CuO_4$ [73, 74, 75], Mang *et al.* [60, 69] suggest that all the observed field-induced effect in $Nd_{1.85}Ce_{0.15}CuO_4$ [72] can be

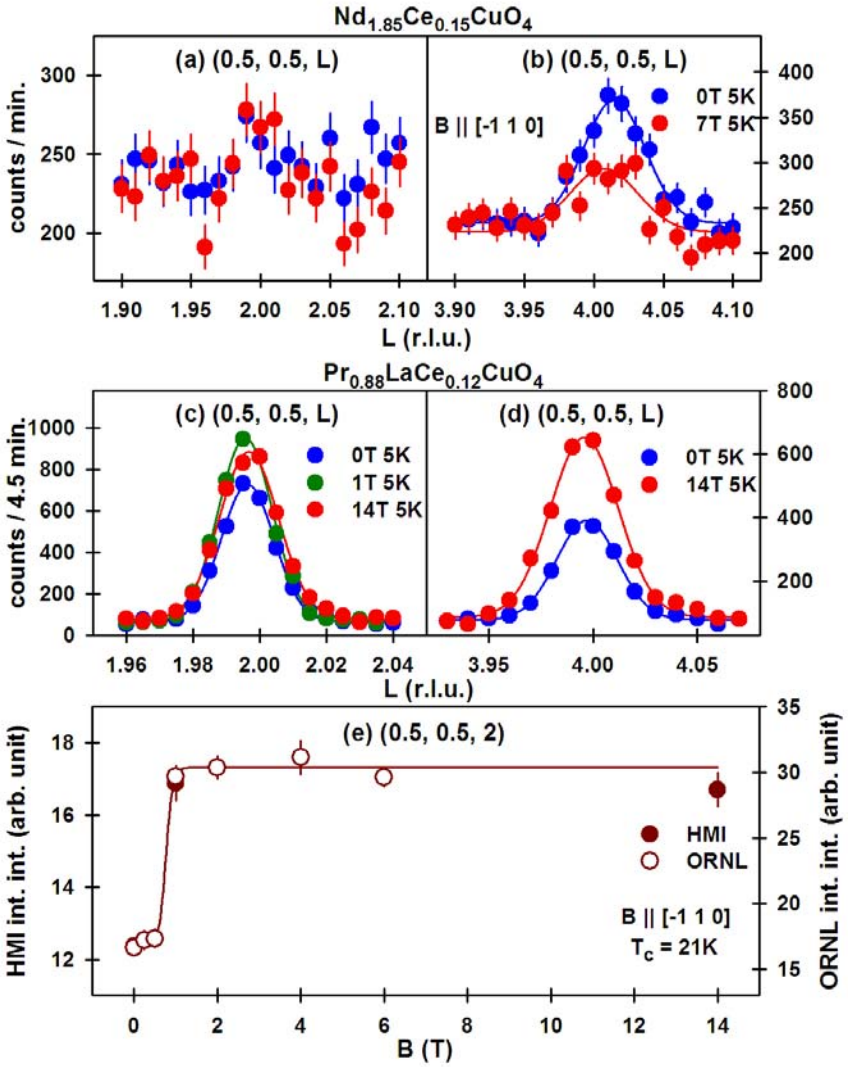

Fig. 3.14 The comparison of the in-plane magnetic field effect on the magnetic Bragg peaks of PLCCO and $Nd_{1.85}Ce_{0.15}CuO_4$ at low temperature. (a)-(b) *L* scans around (0.5, 0.5, 2) and (0.5, 0.5, 4) in $Nd_{1.85}Ce_{0.15}CuO_4$. (c)-(d) *L* scans around (0.5, 0.5, 2) and (0.5, 0.5, 4) in PLCCO. The intensity difference between $Nd_{1.85}Ce_{0.15}CuO_4$ and PLCCO is due to the induced Nd^{3+} moment in $Nd_{1.85}Ce_{0.15}CuO_4$. (e) The integrated intensity of (0.5, 0.5, 2) as a function of a field. Right after the spin-flop transition, the integrated intensity shows no field dependence up to 14 T. This confirms that the Pr^{3+} moment is not induced by a magnetic field up to 14 T.

explained by a paramagnetic scattering from the impurity $(Nd,Ce)_2O_3$ phase. Since there will always be paramagnetic scattering from $(Nd,Ce)_2O_3$ under the influence of a magnetic field in the superconducting $Nd_{1.85}Ce_{0.15}CuO_4$, it is more productive to study the electron-doped superconductors where the impurity phase has no field-induced effect. The superconducting PLCCO is a good candidate because Pr^{3+} in the impurity phase $(Pr,La,Ce)_2O_3$ has a nonmagnetic singlet ground state. To reveal the intrinsic magnetic field effect on Cu^{2+} magnetism in the superconducting PLCCO, one must understand the field-induced effect on the antiferromagnetic order in the nonsuperconducting PLCCO and the impurity $(Pr,La,Ce)_2O_3$.

To determine the effect of a *c*-axis magnetic field on the antiferromagnetic order of the nonsuperconducting PLCCO, we aligned the reoxygenated sample (T_N = 186 K) in the [*H K* 0] scattering plane and applied a magnetic field along a *c*-axis. Figure 3.15(a) and (b) show the radial scans across (0.5, -0.5, 0) and (0.5, -1.5, 0) at a zero and 6-T fields. A magnetic field of 6 T has no effect on either peak at 5 K within the error of the measurements. These results are similar to those in the nonsuperconducting $Nd_{1.85}Ce_{0.15}CuO_4$. Therefore, a 6-T magnetic field along the *c*-axis does not affect the antiferromagnetic structure or induce moments in both the nonsuperconducting PLCCO and $Nd_{1.85}Ce_{0.15}CuO_4$ sample.

We have shown that the peak at (0.5, 0.5, 0) in the nonsuperconducting sample is structural (Fig. 3.5(d)). However, the (0.5, 0.5, 0) peak observed in [*H K* 0] scattering plane is missing in the *L* scan shown Fig. 3.15(c). Figure 3.15(a) and (c) indicate that the peak at (0.5, 0.5, 0) is diffusive structural scattering of PLCCO similar to that seen in the superconducting $Nd_{1.85}Ce_{0.15}CuO_4$ [72]. This structural peak is not coming from the impurity phase $(Pr,La,Ce)_2O_3$. The absence of peak at (0, 0, 2.2) in Fig. 3.15(d) proves that there is no impurity phase in the nonsuperconducting sample.

Next, to measure the field effect on the impurity phase, we aligned the superconducting crystals in the [*H H L*] scattering plane and applied the magnetic field in the [-1 1 0] direction.

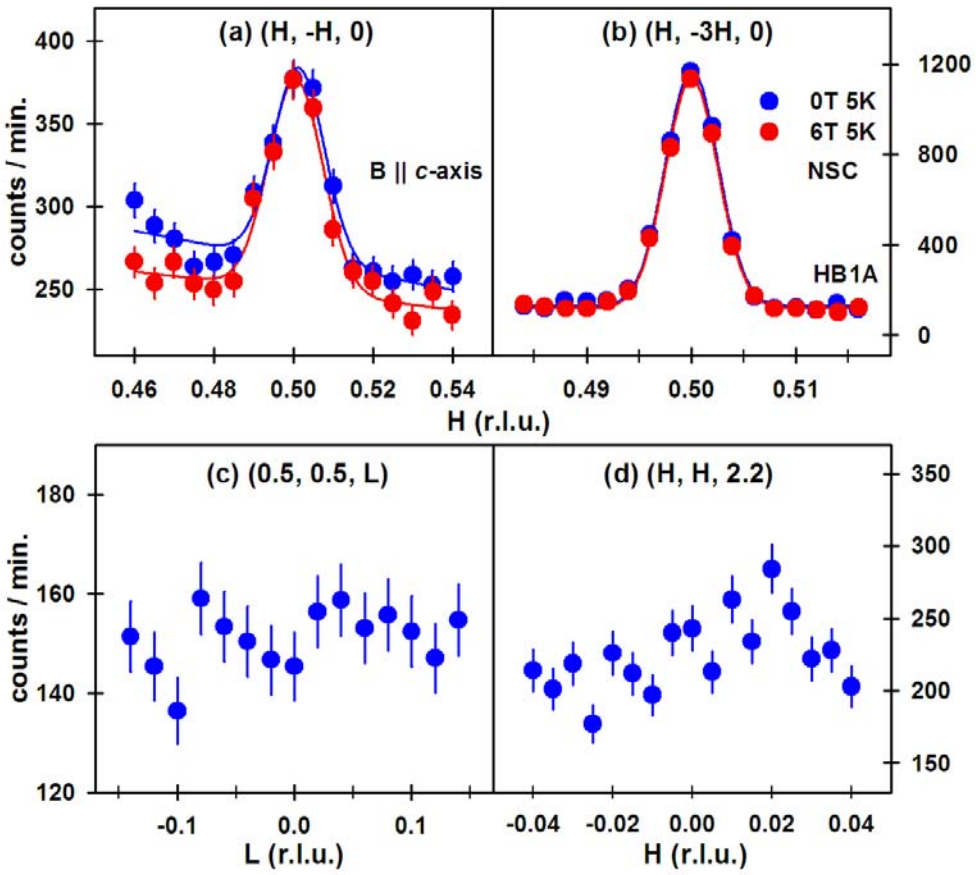

Fig. 3.15 Magnetic field effect on a nonsuperconductor. (a)-(b) Magnetic field dependent scattering around (0.5, -0.5, 0) and (0.5, -0.5, 0) of a nonsuperconducting PLCCO in the [*H K* 0] scattering plane. Radial scans across (a) (0.5, -0.5, 0) and (b) (0.5, -1.5, 0) at 5 K with a zero- and 6-T fields, respectively. The magnetic field is applied along the *c*-axis. The scattering at (0.5, -1.5, 0) is mostly magnetic from the noncollinear structure. (c) The *L* scan of (0.5, 0.5, 0) shows no peak in the [*H H L*] scattering plane. This shows that the peak at (0.5, -0.5, 0) in the [*H K* 0] scattering plane is diffusive structural scattering of PLCCO similar to that seen in the superconducting $Nd_{1.85}Ce_{0.15}CuO_4$. (d) The absence of impurity peak at (0, 0, 2.2) confirms that there is no impurity in the nonsuperconducting PLCCO.

Since $(Pr,La,Ce)_2O_3$ has a cubic crystal structure with lattice parameter ~10 % smaller than the *c*-axis lattice parameter of PLCCO, cubic reflections $(2, 0, 0)_c$ and $(0, 0, 2)_c$ from $(Pr,La,Ce)_2O_3$ can be indexed as (0.5, 0.5, 0) and (0, 0, 2.2) in PLCCO Miller indices, respectively. The relationship of Miller indices between PLCCO and $(Pr,La,Ce)_2O_3$ is described in Fig. 2.14 in chapter 2 using real space and reciprocal space. A magnetic field **B** || [-1 1 0] in the CuO_2 plane of PLCCO is along the [0 1 0] direction of the cubic $(Pr,La,Ce)_2O_3$. Since the impurity phase has cubic symmetry, the magnetic field effect on paramagnetic scattering should be the same for a magnetic field of both [0 1 0] and [0 0 1] direction. Therefore, we can check the *c*-axis magnetic field effect on the impurity by measuring the (0, 0, 2.2) peak with a magnetic field along [-1 1 0].

The field effect on the $(Pr,La,Ce)_2O_3$ impurity phase is measured in the optimally doped and underdoped superconducting PLCCO samples with T_c = 24 K, 21 K, and 16 K. Following previous work on $Nd_{1.85}Ce_{0.15}CuO_4$ in chapter 2, we probe the impurity peak positions $(0, 0, 2)_c$, $(1, 1, 0)_c$, and $(0, 0, 4)_c$ which correspond to PLCCO Miller indices (0, 0, 2.2)/(0.5, 0.5, 0), (0.5, 0, 0), and (0, 0, 4.4), respectively. Figure 3.16 summarizes the outcome around (0, 0, 2.2) for the three superconducting PLCCO samples investigated. The [*H H* 2.2] scans across the impurity position at (0, 0, 2.2) show no observable field-induced effect on the impurity phase up to 14 T. Additional measurements of the temperature dependent scattering around (0, 0, 4.4) (Fig. 3.17(a)) and the *c*-axis field-dependent scattering around (0.5, 0, 0) (Fig. 3.17(b)) on the T_c =21 K sample confirm that the Pr^{3+} ions in $(Pr,La,Ce)_2O_3$ have a nonmagnetic singlet ground state and cannot be polarized by a 14.5-T magnetic field. In contrast, the Nd^{3+} ions in the $(Nd,Ce)_2O_3$ impurity phase can be easily polarized by an applied magnetic field. Therefore, we can avoid the complication of field-induced paramagnetism from the impurity phase by studying PLCCO and the outcome should reveal the intrinsic properties of Cu^{2+} magnetism in the electron-doped superconducting materials.

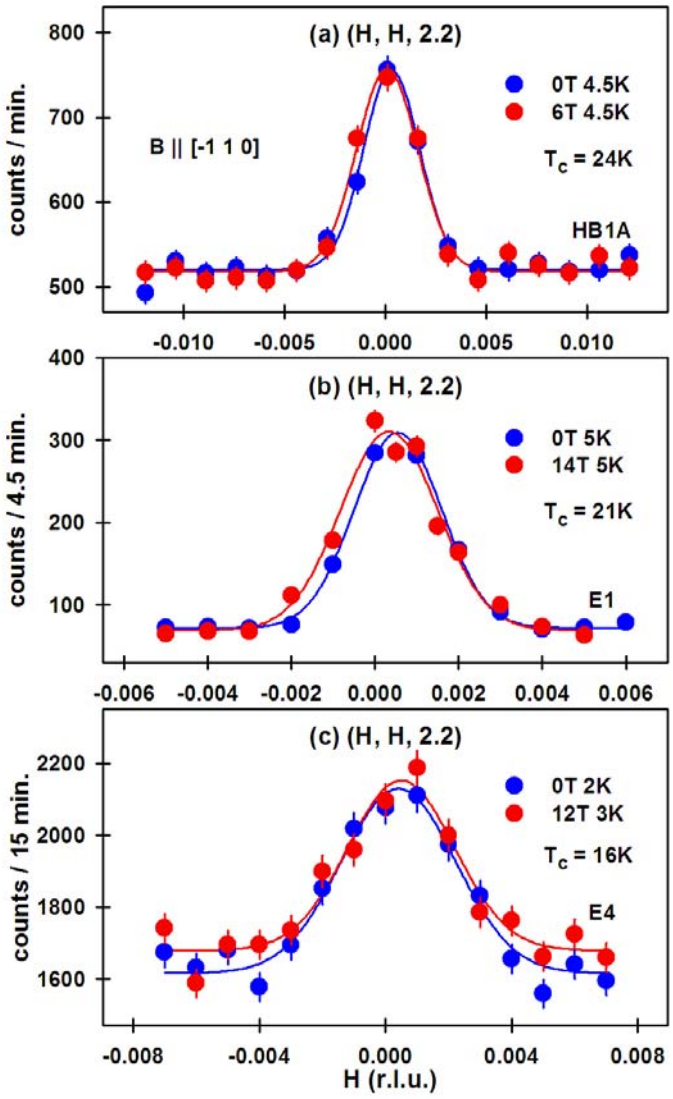

Fig. 3.16 Magnetic field effect on the impurity peak position at (0, 0, 2.2) at low temperature in the superconductors. (a)-(c) scans along the [*H H* 2.2] direction for the T_c = 24 K, 21 K, and 16 K PLCCO, respectively. The magnetic field is applied along the [-1 1 0] direction.

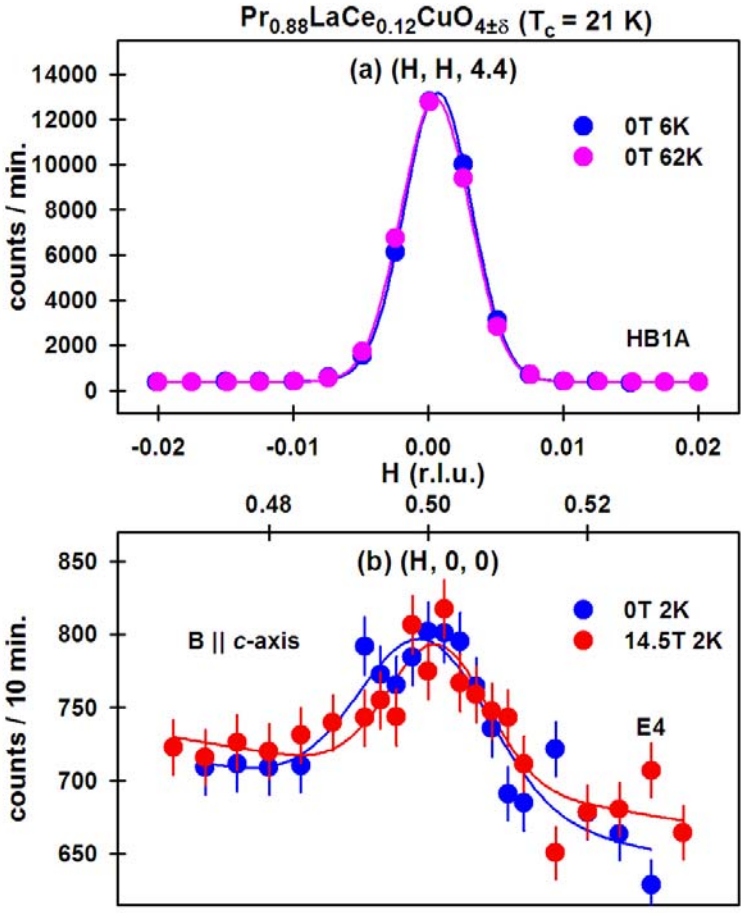

Fig. 3.17 The temperature dependence and the field effect on the impurity peaks in the T_c = 21K sample. (a) [H H 4.4] scan through (0, 0, 4.4) position of impurity peak $(0, 0, 4)_c$ at low and high temperature. The temperature independent scattering indicates that the impurity peak has no magnetic component. (b) Radial [H 0 0] scan across (0.5, 0, 0) of the impurity peak $(1, 1, 0)_c$ at a zero- and 14.5-T c-axis magnetic field. It shows no field-induced effect. This indicates that the impurity phase cannot be polarized by a 14.5-T magnetic field.

3.7 A *c*-axis magnetic field effect on the quasi-2D and 3D antiferromagnetic order in the superconducting $Pr_{0.88}LaCe_{0.12}CuO_{4\pm\delta}$

The existence of quasi-2D antiferromagnetic order in the electron-doped PLCCO in the underdoped regime is very exciting. This is because the quasi-2D antiferromagnetic order in PLCCO is very similar to the quasi-2D SDW in the hole-doped superconductor LSCO. Therefore, determining the role of quasi-2D antiferromagnetic order to superconductivity in the electron-doped superconductors may be very crucial in the theory of high-T_c superconductivity.

In this section, we describe the effect of a *c*-axis aligned magnetic field on the superconducting PLCCO samples. Since the previous section confirmed that the $(Pr,La,Ce)_2O_3$ impurity phase does not respond to an applied magnetic field, any field-induced effect on the superconducting samples must be intrinsic to PLCCO. For the experiment, we align crystals in the [*H K* 0] scattering plane and apply magnetic fields along the *c*-axis. Figure 3.18 shows the radial [*H H* 0] and [*H 3H* 0] scans around (0.5, 0.5, 0) and (0.5, 1.5, 0) positions, respectively for the superconducting T_c = 24 K, 21 K, and 16 K samples. In all cases, we carefully applied magnetic fields above T_c and cooled the samples to below T_c in the magnetic field. For the optimally doped PLCCO (T_c = 24 K), a magnetic field of 6.5 T at 4.5 K does not affect the scattering at (0.5, 0.5, 0) and (0.5, 1.5, 0) (Fig. 3.18(a) and (e)). This is consistent with an earlier report on the overdoped PLCCO (T_c =16 K) [76]. Note that in this case the peaks at both positions arise mostly from the superlattice and the $(Pr,La,Ce)_2O_3$, and there are no static antiferromagnetic orders in the sample (section 3.3.).

The underdoped superconducting samples (T_c = 21 K and 16 K), however, show clear low-temperature field-induced intensity gain at the quasi-2D antiferromagnetic position (0.5, 0.5, 0) (Fig. 3.18(b)-(d)), but not at the 3D antiferromagnetic order position (0.5, 1.5, 0) (Fig. 3.18(f)-(h)). In particular, the field-induced intensity appears to increase with the increasing magnetic field for the T_c = 21 K PLCCO (Fig. 3.18(b) and (c)). Figure 3.19 shows that this field-induced

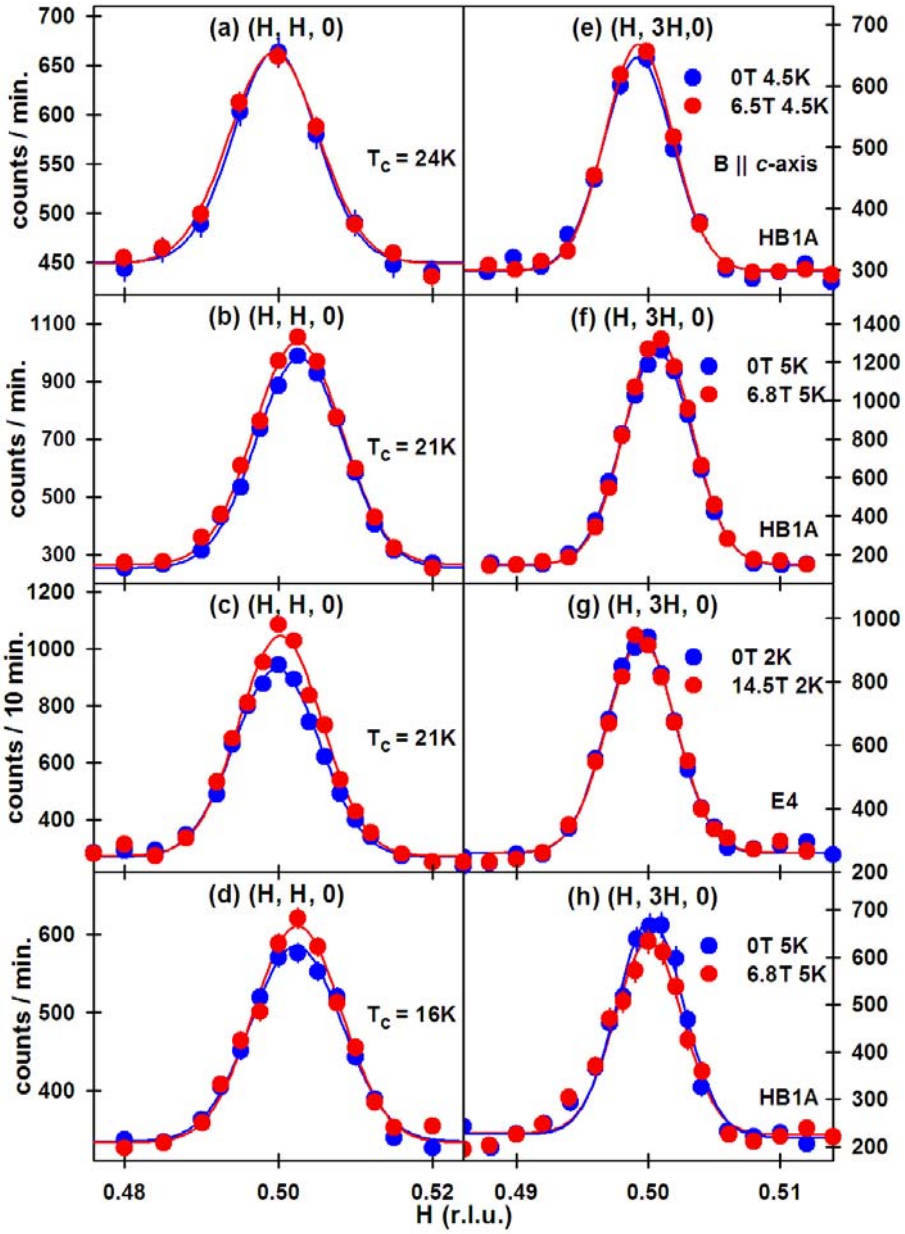

Fig. 3.18 The effect of a *c*-axis magnetic field on various superconducting PLCCO samples at low temperatures. The data below 7 T were taken at HB-1A of HFIR while higher field data were collected on E4 of HMI. The [*H H* 0] scans around (0.5, 0.5, 0) for (a) T_c = 24 K, (b)-(c) 21 K, and d) 16 K PLCCO samples at specified temperatures. e-h) [*H* 3*H* 0] scans around (0.5, 1.5, 0) in the same experimental setup as in (a)-(d).

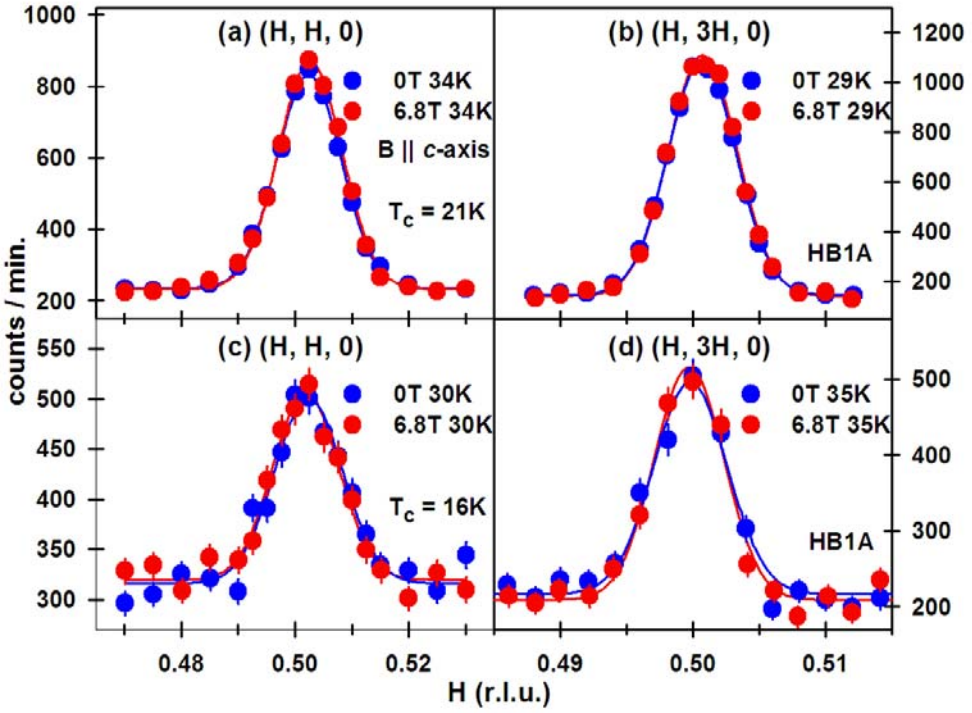

Fig. 3.19 The field dependence of the scattering across (0.5, 0.5, 0) and (0.5, 1.5, 0) at temperatures above T_c and below T_N. (a)-(b) for the T_c = 21 K sample. (c)-(d) for the T_c = 16 K sample. No field-induced effects are observed.

effect disappears in the higher temperatures above T_c but below T_N.

Figure 3.20 shows the temperature dependence of the scattering at (0.5, 0.5, 0) and (0.5, 1.5, 0) for the T_c = 21 K and 16 K samples at the different magnetic fields. For the 3D antiferromagnetic Bragg peak (0.5, 1.5, 0), the intensity simply drops with increasing temperature and shows essentially no difference between field-on and field-off. On the other hand, scattering at (0.5, 0.5, 0) shows a clear low-temperature enhancement under the magnetic field that vanishes at high temperatures. Although most of the field-induced effects occur at temperatures below the zero-field T_c marked by an arrow, we were unable to map out the detailed temperature-field dependence of the effect due to weakness of the signal. The enhancement of quasi-2D antiferromagnetic order by a *c*-axis magnetic field is similar to the field-induced effect on the incommensurate SDW in LSCO [14] and La_2CuO_{4+y} [35, 36].

Finally, we carried out a series of [*H H 0*] and [*H 3H 0*] scans across (0.5, 0.5, 0) and (0.5, 1.5, 0), respectively for the T_c = 21 K sample to determine the low-temperature field-dependence of the scattering. Figure 3.21 shows the integrated intensity of (0.5, 0.5, 0) and (0.5, 1.5, 0) as a function of magnetic field. The integrated intensity of the peak at each magnetic field is computed by fitting the raw data with a Gaussian on a linear background (See Fig. 3.18). The blue circles show the ORNL data taken at 5 K for the magnetic fields up to 6.8 T while the red circles are HMI data at 2 K for the magnetic fields up to 14.5 T. By combining ORNL and HMI data, we find that the field-induced effect at (0.5, 0.5, 0) increases linearly with increasing magnetic field up to 13.5 T and may saturate at higher fields (Fig. 3.21(a)). On the other hand, the 3D residual antiferromagnetic order (0.5, 1.5, 0) peak shows no observable field-induced effect for the magnetic fields up to 14.5 T (Fig. 3.21(b)).

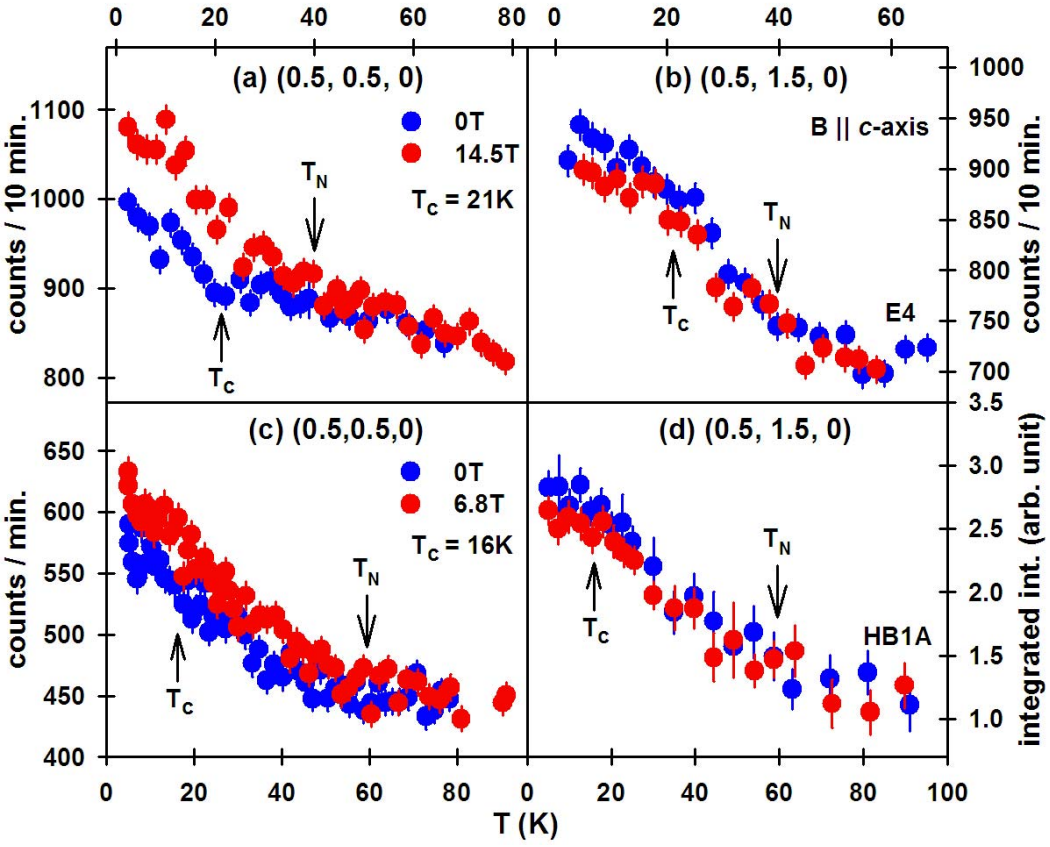

Fig. 3.20 Temperature dependence of the scattering at (0.5, 0.5, 0) and (0.5, 1.5, 0) positions for the underdoped superconductors. (a)-(b) T_c =21 K and (c)-(d) T_c = 16 K samples at a zero- and finite *c*-axis aligned magnetic fields. Clear low-temperature field-induced effects are seen at (0.5, 0.5, 0) but not at (0.5, 1.5, 0) for both the T_c = 21 K and 16 K PLCCO samples.

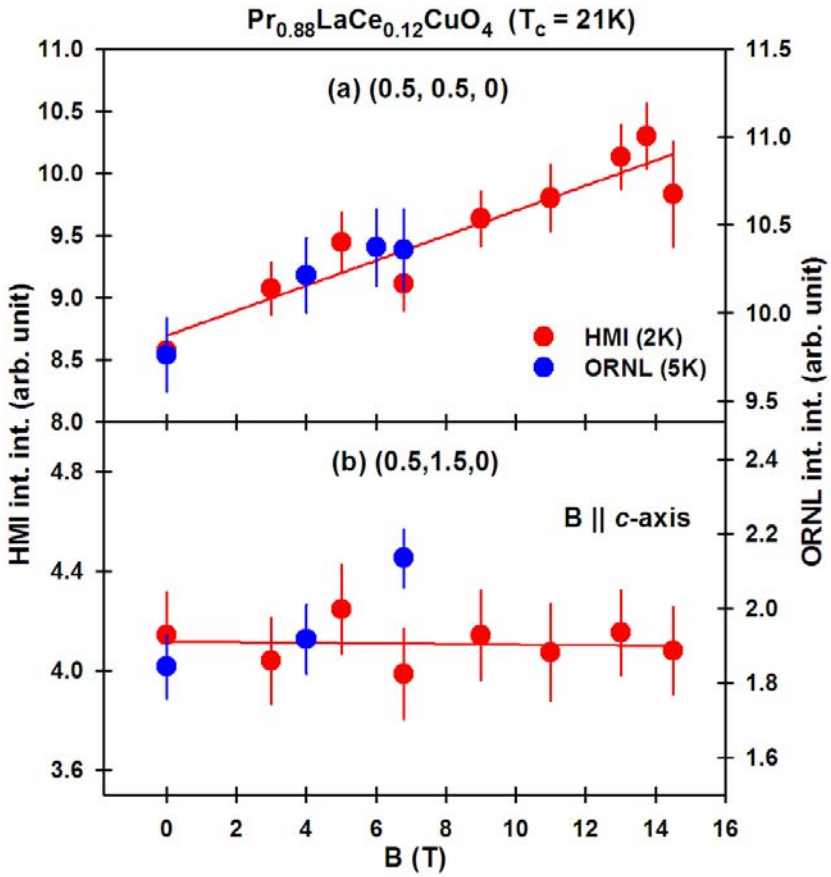

Fig. 3.21 Integrated intensity of (0.5, 0.5, 0) and (0.5, 1.5, 0) as a function of magnetic field. (a) Integrated intensity of (0.5, 0.5, 0) as a function of increasing field. (b) Integrated intensity of (0.5, 1.5, 0) is independent of applied magnetic field up to 14.5 T. Blue circles are data from ORNL at 5 K and red circles are HMI data at 2 K.

3.8 Magnetic field-induced anisotropy on the superconducting $Pr_{0.88}LaCe_{0.12}CuO_{4\pm\delta}$ (T_c = 21 K)

The discovery of a *c*-axis field-induced effect unrelated to the $(Pr,La,Ce)_2O_3$ impurity phase in the underdoped PLCCO suggests that a quasi-2D antiferromagnetic order is competing with superconductivity. However, it cannot prove directly that such effect is coming from the suppression of superconductivity. To determine whether a quasi-2D antiferromagnetism is a competing order to superconductivity in PLCCO, we perform its field directional dependence. This is because high-T_c superconductors are layered materials; a magnetic field aligned along the *c*-axis suppresses superconductivity much more dramatically than the same field parallel to the CuO_2 planes.

Since only the quasi-2D antiferromagnetic order is enhanced by a *c*-axis magnetic field, we focus on the anisotropic field-induced effect at (0.5, 0.5, 0) by comparing its *c*-axis magnetic field-induced effect to that seen in the in-plane one. We aligned a superconducting sample of T_c = 21 K in the [*H H L*] zone and applied a magnetic field along the [-1 1 0] direction. Figure 3.22 shows scans along the [*H H* 0] and the [0.5 0.5 *L*] direction around (0.5, 0.5, 0) at a zero- and 6-T magnetic field. There is no observable field-induced effect, in contrast to the *c*-axis field data across (0.5, 0.5, 0) (Fig. 3.18(b)-(c)). On increasing the in-plane magnetic field to 14 T, we again failed to observe any field-induced effect around (0.5, 0.5, 0) at 5 K (Fig. 3.23(b) and (c)). For comparison, we plot scans around (0.5, 0.5, 0) both a magnetic field along the *c*-axis and the [-1 1 0] directions in Fig. 3.23. It is clear that a *c*-axis aligned magnetic field enhances scattering at (0.5, 0.5, 0) while the same magnetic field parallel to the CuO_2 planes does not. Since a 14-T in-plane magnetic field only induces the spin-flop transition and does not affect the Cu/Pr moments of the residual antiferromagnetic phase, our observation of an anisotropic field effect in the T_c = 21 K PLCCO is the most direct evidence that the enhancement of quasi-2D antiferromagnetic

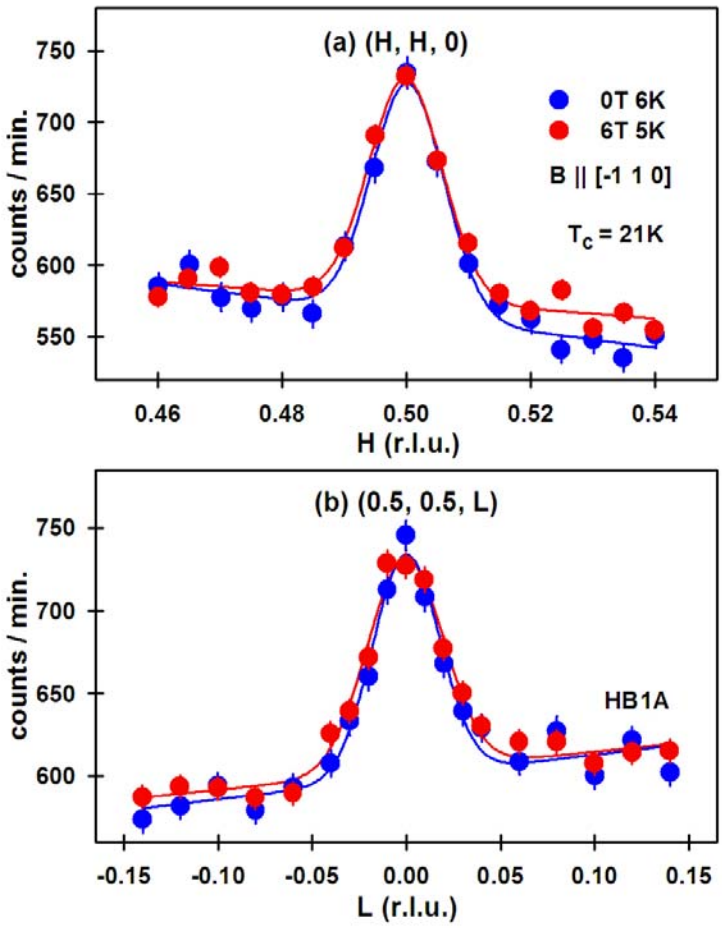

Fig. 3.22 The influence of an in-plane magnetic field on the quasi-2D antiferromagnetic order in the T_c = 21 K PLCCO. (a) [*H H 0*] scan around (0.5, 0.5, 0) for a zero- and 6-T field at 5 K. (b) [0.5, 0.5, *L*] scan around (0.5, 0.5, 0). A 6-T in-plane magnetic field has no observable effect on the quasi-2D antiferromagnetic order at 5 K. The *c*-axis coherence length of (0.5, 0.5, 0) is about 200 Å.

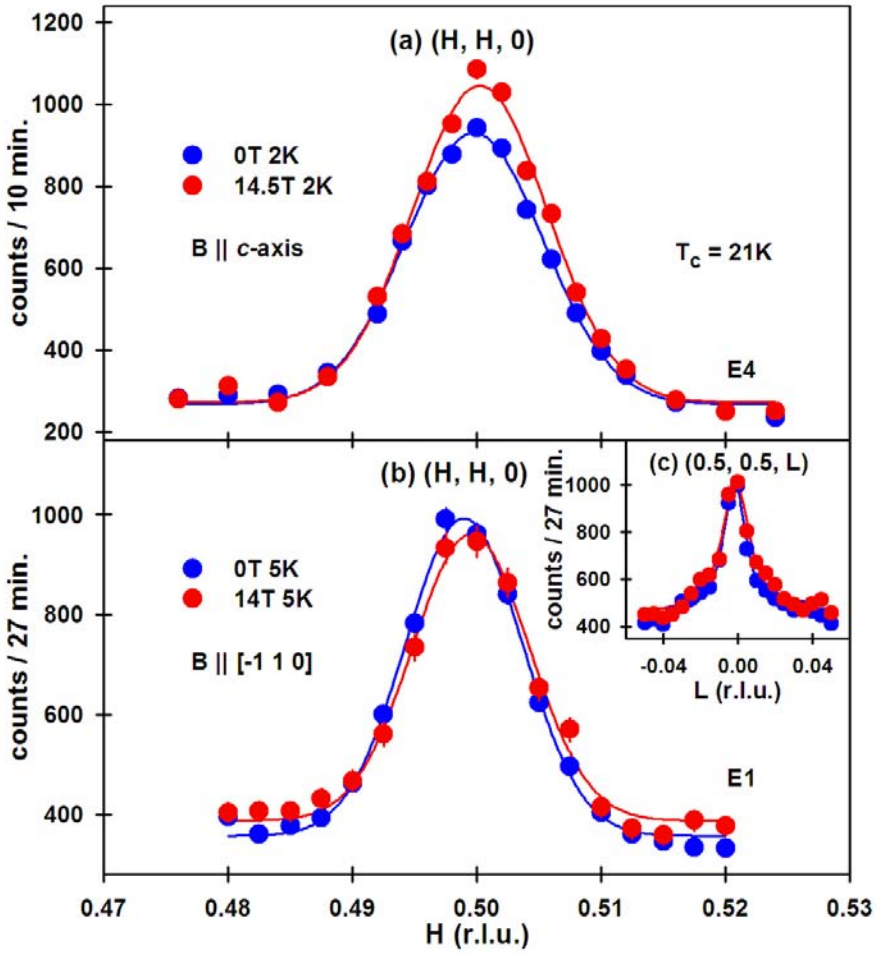

Fig. 3.23 Anisotropic field-induced effect on the quasi-2D antiferromagnetic order of the T_c = 21 K PLCCO. (a) [*H H* 0] scan across (0.5, 0.5, 0) in a zero- and 14.5-T field at 2 K in the [*H K* 0] zone. Magnetic field is applied along a *c*-axis. (b)-(c) [*H H* 0] and [0.5 0.5 *L*] scans across (0.5, 0.5, 0) in a zero- and 14-T field at 5 K. Magnetic field is applied along the [-1 1 0] direction.

order is related to the suppression of superconductivity.

A field-induced effect is present at the (0.5, 0.5, 0) quasi-2D antiferromagnetic position; but, not at the (0.5, 1.5, 0) 3D antiferromagnetic Bragg position. This suggests that Cu^{2+} spins that contribute to the diffusive quasi-2D antiferromagnetism cannot arise from the same Cu^{2+} spins that give the 3D antiferromagnetic moments. While similar field-induced enhancement was also observed in the case of optimally doped $Nd_{1.85}Ce_{0.15}CuO_4$ (chapter 2), there are important differences between PLCCO and $Nd_{1.85}Ce_{0.15}CuO_4$. First, optimally doped PLCCO has no residual antiferromagnetic order while 3D antiferromagnetic order coexists with superconductivity in $Nd_{1.85}Ce_{0.15}CuO_4$ even for the samples with highest T_c. Whether the 3D antiferromagnetic phase coexists with superconductivity macroscopically or microscopically in $Nd_{1.85}Ce_{0.15}CuO_4$ is still an open question. It is not clear why the optimally doped $Nd_{1.85}Ce_{0.15}CuO_4$ has the 3D antiferromagnetic order in coexistence with superconductivity while similar PLCCO does not. In addition, there are no detailed studies on how $Nd_{2-x}Ce_xCuO_4$ is transformed from an antiferromagnetic insulator to an optimally doped superconductor. As a consequence, it is unclear how to compare PLCCO directly with $Nd_{1.85}Ce_{0.15}CuO_4$. Second, a *c*-axis aligned magnetic field on the optimally doped $Nd_{1.85}Ce_{0.15}CuO_4$ not only enhances the magnetic signal at (0.5, 0.5, 0), but also at 3D antiferromagnetic Bragg positions such as (0.5, 1.5, 0) and (0.5, 0.5, 3). For the underdoped PLCCO, a 14-T magnetic field has no observable effect on the 3D antiferromagnetic order at (0.5, 1.5, 0). Finally, a *c*-axis aligned magnetic field enhances the intensity of the Bragg peak at (1, 1, 0) for both the nonsuperconducting and the superconducting $Nd_{1.85}Ce_{0.15}CuO_4$ while a similar field has no observable effect on any nuclear Bragg peaks in the nonsuperconducting and the superconducting PLCCO. This difference must arise from the polarization of the Nd^{3+} ions in $Nd_{1.85}Ce_{0.15}CuO_4$ and therefore is not intrinsic to the physics of electron-doped copper oxides.

3.9 Discussion

We use neutron scattering to study the phase transition of PLCCO from a long-range ordered antiferromagnet to an optimally doped superconductor without the static antiferromagnetic order. In the underdoped regime, we observe the coexistence of the quasi-2D and the 3D antiferromagnetic order in the superconducting state. The 3D antiferromagnetic order has the same noncollinear magnetic structure as that in the parent Pr_2CuO_4 (Fig. 3.3(a)). Since the noncollinear spin structure does not allow the magnetic Bragg scattering at (0.5, 0.5, 0), it is interesting to ask whether the Cu^{2+} spins that give the 3D antiferromagnetic order also contribute to the diffusive quasi-2D scattering.

In one picture, the annealing process necessary to achieve superconductivity in PLCCO may also induce macroscopic oxygen inhomogeneity, giving rise to mesoscopic separation between the superconducting and the antiferromagnetic nonsuperconducting phases. In the antiferromagnetic nonsuperconducting phase, a weak random rotation of the magnetic moment from one plane to another induces a long-range spin order in the plane, but along the *c*-axis one observes simultaneously the 3D Bragg peak and the diffusive 2D scattering. If both the diffusive 2D (0.5, 0.5, 0) and 3D antiferromagnetic (0.5, 1.5, 0) signals are from the same Cu^{2+} spins macroscopically phase separated from the nonmagnetic superconducting regions, one would expect that the application of a *c*-axis aligned magnetic field will have no (or the same) effect on both the 2D and 3D scattering. Instead, we find a clear *c*-axis field-induced effect at (0.5, 0.5, 0) but not at (0.5, 1.5, 0) (section 3.7). Therefore, Cu^{2+} spins contributing to the diffusive 2D scattering cannot arise from the same Cu^{2+} spins giving the 3D antiferromagnetic scattering.

Alternatively, the annealing process may produce local oxygen distribution fluctuations acting as pinning centers for microscopic electronic phase separation. In this case, the quasi-2D antiferromagnetic scattering may arise from weakly correlated CuO_2 layers with the antiferromagnetic order modulation in the matrix of the 3D antiferromagnetic state. The observed

diffusive commensurate antiferromagnetic order in PLCCO is then analogous to the incommensurate 2D SDW in the hole-doped LSCO and La_2CuO_{4+y} [12, 26]. When a *c*-axis magnetic field is applied, the residual 3D antiferromagnetic order is not disturbed but the quasi-2D antiferromagnetic order at (0.5, 0.5, 0) is enhanced at the expense of superconductivity.

We suggest two models of collinear spin structures in Fig. 3.24 to give the magnetic scattering at (0.5, 0.5, 0) as well as (0.5, 1.5, 0). The filled and open circles are basal plane Cu and body-centered Cu, respectively. Model I has spin directions [1 0 0] and [0 1 0], respectively for domain-I and domain-II. Model II with collinear domain-I/II are essentially the same as model I with collinear domain-I/II, except the spin directions are along [1 1 0] and [-1 1 0] directions.

Assuming each collinear model has two equally populated domains as depicted in Fig. 3.24 and negligible Pr^{3+} moment contribution, we calculate the expected magnetic intensities of these two models in Table 3.2. The calculation for both models shows that the quasi-2D magnetic scattering appears mostly at (0.5, 0.5, 0). The calculated intensity at (0.5, 1.5, 0) is about 16 times smaller when we use 2θ value for our experimental condition $E_i = E_f = 13.7$ meV. This is consistent with our observation of a weak (or no) field-induced effect at (0.5, 1.5, 0).

To estimate an effective moment of the quasi-2D antiferromagnetic order, we can use the integrated intensity of (0.5, 0.5, 0) where the only contribution is quasi-2D antiferromagnetism. Even though quasi-2D antiferromagnetism contributes at (0.5, 1.5, 0) position, this position also has the 3D antiferromagnetic contribution. Neutrons are a bulk probe and cannot determine the location of the Cu^{2+} spins that contribute the quasi-2D and 3D antiferromagnetic responses. Therefore, one can only estimate an average Cu^{2+} moment by normalizing the magnetic intensity at (0.5, 0.5, 0) to the weak nuclear (1, 1, 0) reflection. We can estimate the Cu^{2+} moment from the quasi-2D antiferromagnetic peak by the formula $I_{cal}(0.5, 0.5, 0)/I_{cal}(1, 1, 0) = I_{ob}(0.5, 0.5, 0)/I_{ob}(1, 1, 0)$. In our experiment at HMI, we got the magnetic intensity $I_{ob}(0.5, 0.5, 0) = 2.0528$ (3.3411)

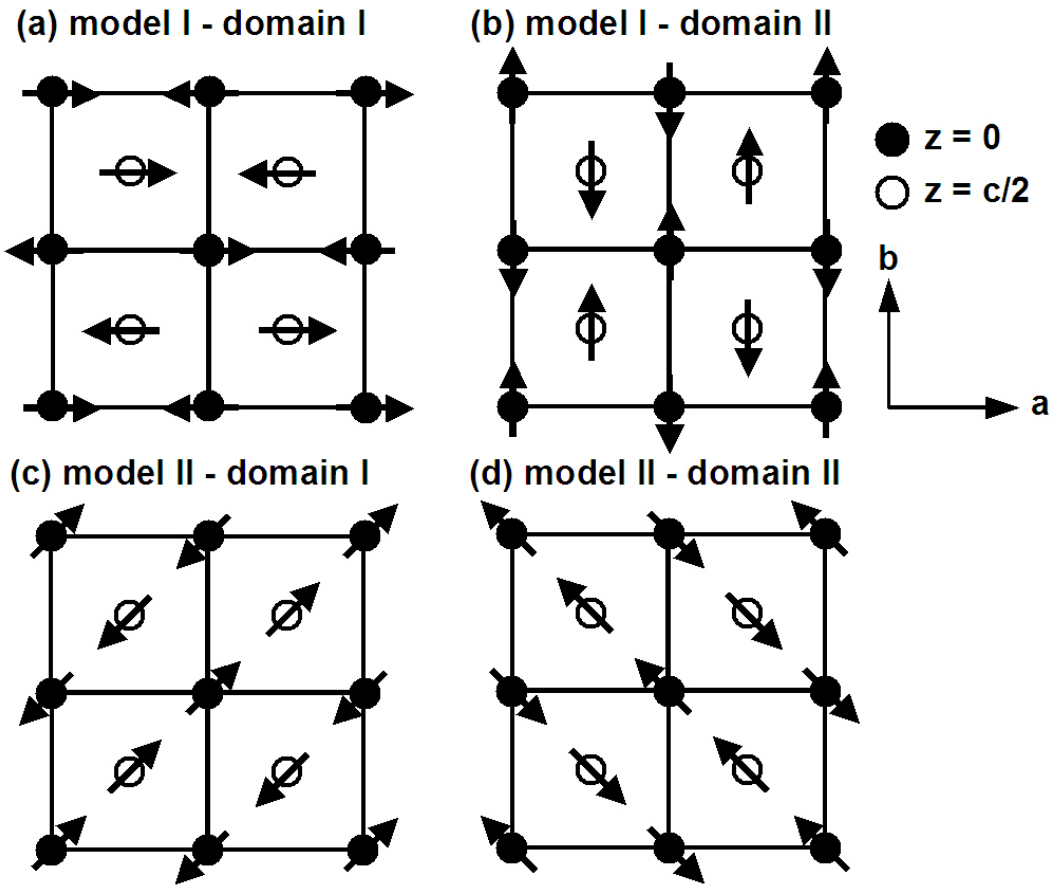

Fig. 3.24 Possible Cu^{2+} magnetic structures responsible for the quasi-2D antiferromagnetic order. (a)-(b) Collinear spin model I, domains I and II. (c)-(d) Collinear spin model II, domains I and II. In the collinear spin structures, the moments are in the *ab*-plane. The closed and open circles represent the z = 0 and z = c/2 CuO_2 planes, respectively. The Pr^{3+} spins are not shown, since the induced moment of Pr^{3+} is negligible in the superconducting PLCCO samples. Here we assumed weak (2 or 3 lattices) spin correlations along the *c*-axis.

Table 3.2 Magnetic neutron scattering intensity calculations for proposed spin structures of $Pr_{0.88}LaCe_{0.12}CuO_{4\pm\delta}$ in Fig. 3.24. The angle θ is the scattering angle for the Bragg peak. The intensity is the average of two domains contribution.

(*H, K, L*)	I_{cal} (model I)	I_{cal} (model II)
(0.5, 0.5, 0)	$\frac{1}{2\sin 2\theta} 32.0\, p^2 (f_{cu} M_{cu} - 0.88 f_{pr} M_{pr})^2$	$\frac{1}{2\sin 2\theta} 64.0\, p^2 (f_{cu} M_{cu} - 0.88 f_{pr} M_{pr})^2$
(0.5, 1.5, 0)	$\frac{1}{2\sin 2\theta} 6.4\, p^2 (f_{cu} M_{cu} - 0.88 f_{pr} M_{pr})^2$	$\frac{1}{2\sin 2\theta} 12.8\, p^2 (f_{cu} M_{cu} - 0.88 f_{pr} M_{pr})^2$

at 0 T (14 T) and the structural intensity $I_{ob}(1, 1, 0) = 4547$. From these values, we obtain Cu^{2+} moment 0.032 μ_B at 0 T and 0.041 μ_B at 14.5T for model I. Model II gives Cu^{2+} moments of 0.022 μ_B at 0 T and 0.028 μ_B at 14.5 T. Therefore, the field-induced enhancement of the Cu^{2+} moment in PLCCO is 0.009 μ_B for model I and 0.006 μ_B for model II. This value is smaller than that of hole-doped LSCO and La_2CuO_{4+y}, [14, 35].

When the as-grown PLCCO is transformed from a long-range ordered antiferromagnet to an optimally doped superconductor by annealing in pure argon, the 3D antiferromagnetic order is degraded and the quasi-2D antiferromagnetic order develops with the appearance of superconductivity. As full superconductivity is obtained with T_c = 24 K, both the static 3D and quasi-2D antiferromagnetic orders vanish. We confirm that the annealing process necessary for producing superconductivity also induces the bixbyite $(Pr,La,Ce)_2O_3$ as an impurity phase. However, in contrast to $(Nd,Ce)_2O_3$ in the superconducting $Nd_{1.85}Ce_{0.15}CuO_4$, a 14-T magnetic field does not polarize Pr^{3+} in $(Pr,La,Ce)_2O_3$. Therefore, this property allows us to study the intrinsic field-induced effect on Cu^{2+} in PLCCO. At optimal doping, a 6.5-T *c*-axis magnetic field does not induce the static antiferromagnetic order due to the presence of a spin gap. For the underdoped materials, a 14-T *c*-axis magnetic field enhances only the quasi-2D antiferromagnetic

order at (0.5, 0.5, 0) but has no observable effect on the 3D residual antiferromagnetic order at (0.5, 1.5, 0). A similar magnetic field applied along the [-1 1 0] direction in the CuO_2 plane only induces the spin-flop transition but has no effect on the quasi-2D antiferromagnetic order. The anisotropy of field-induced effect demonstrates that the enhancement of the quasi-2D antiferromagnetic order is associated with the suppression of superconductivity due to competition.

Fujita *et al.* reported that the magnetic scattering at (0.5, 1.5, 0) is enhanced by a *c*-axis magnetic field in underdoped PLCCO (x = 0.11). While our results for the optimally doped PLCCO are consistent with that for the overdoped one by Fujita *et al*. [76], we cannot confirm their results for the underdoped PLCCO (x = 0.11). In particular, the 3D antiferromagnetic order has no observable field dependence in our underdoped samples. On the other hand, it would also be interesting to check if their x = 0.11 PLCCO sample has field-induced effect at (0.5,0.5,0). At present, it is unclear how to reconcile our results with that of Fujita *et al*. [76]. Perhaps the difference in Ce^{4+} concentration and/or post annealing oxygen treatment plays an important role in determining the properties of these materials. In any case, what is clear is that the underdoped PLCCO has a field-induced effect unrelated to the impurity phase, and such an effect appears to be associated with the suppression of superconductivity [77].

To determine the influence of an applied magnetic field on the residual 3D antiferromagnetic order in the superconducting electron-doped cuprates, one must understand the differences in the field-induced effect between the optimally doped $Nd_{1.85}Ce_{0.15}CuO_4$ and the underdoped PLCCO. The optimally doped $Nd_{1.85}Ce_{0.15}CuO_4$ shows clear *c*-axis field-induced effects at the 3D antiferromagnetic ordering positions such as (0.5, 1.5, 0) and (0.5, 0.5, 3). On the other hand, we were unable to find clear field-induced effects at (0.5, 1.5,0) for the underdoped PLCCO. This difference may arise from the different rare-earth moment

Table 3.3 Magnetic structure factor calculations for the noncollinear spin structure of $Nd_{1.85}Ce_{0.15}CuO_4$ (type-I/III) and PLCCO.

(*H K L*)	$\lvert F \rvert^2$ for $Nd_{1.85}Ce_{0.15}CuO_4$ (type-I/III)	$\lvert F \rvert^2$ for PLCCO
(0.5, 1.5, 0)	$25.6\, p^2\, (f_{cu} M_{cu} + 1.85\, f_{pr} M_{pr})^2$	$25.6\, p^2\, (f_{cu} M_{cu} - 0.88\, f_{pr} M_{pr})^2$
(0.5, 0.5, 3)	$32.0\, p^2\, (f_{cu} M_{cu} + 1.7426\, f_{pr} M_{pr})^2$	$32.0\, p^2\, (f_{cu} M_{cu} - 0.8196\, f_{pr} M_{pr})^2$

contributions to the magnetic scattering. The magnetic structure factor calculation for the noncollinear structure of $Nd_{1.85}Ce_{0.15}CuO_4$ (type-I/III) and PLCCO is compared in Table 3.3. For $Nd_{1.85}Ce_{0.15}CuO_4$, the structure factor calculations show that the induced Nd^{3+} moment from the exchange coupling to the field-induced Cu^{2+} moment contributes constructively to the (0.5, 1.5, 0) and (0.5, 0.5, 3) reflections. On the other hand, the induced Pr^{3+} moment contributes destructively to the Cu^{2+} moment in PLCCO. As a consequence, any field-induced Cu^{2+} moment will reduce slightly the scattering at (0.5, 1.5, 0) for PLCCO because of the negative Pr^{3+} moment contribution (if there is any), but it will induce huge scattering at (0.5, 1.5, 0) and (0.5, 0.5, 3) at low temperature for $Nd_{1.85}Ce_{0.15}CuO_4$ because of the Nd^{3+} moment.

Our results can be thought of as analogous to that in the hole-doped LSCO. When superconductivity first emerges in LSCO with increased Sr-doping, the quasi-2D incommensurate SDW peaks also appear spontaneously to coexist with superconductivity as shown in Fig. 3.1(b) [11, 12, 13]. When LSCO becomes an optimally doped superconductor, the static SDW is replaced by a spin gap and incommensurate spin fluctuations at energies above the gap [27]. A *c*-axis aligned magnetic field that strongly suppresses superconductivity enhances the static SDW order in underdoped LSCO [14, 28] and induces dynamic antiferromagnetism within the gap in the optimally doped LSCO [15]. Very recently, Khaykovich *et al*. report the observation of a

magnetic field-induced transition between magnetically disordered and ordered phases in slightly underdoped LSCO with x=0.144 [78]. Here, the static incommensurate SDW order can be induced directly by a magnetic field from the sample without the zero-field SDW order.

For the electron-doped PLCCO, we also find the simultaneous appearance of the quasi-2D antiferromagnetic order and superconductivity. Except in this case, the quasi-2D antiferromagnetic modulations are commensurate with the underlying lattice. Similar to LSCO, the optimally doped PLCCO does not exhibit the static quasi-2D antiferromagnetic order. When a *c*-axis aligned magnetic field is applied, the quasi-2D antiferromagnetic order is enhanced in the underdoped PLCCO but not in the optimally doped sample. These results are very similar to the hole-doped LSCO, thus suggesting the universality of the magnetic properties in both hole- and electron-doped cuprates. The neutron scattering studies on spin excitations in the optimally and underdoped PLCCO will provide more useful information on the fundamental role of magnetism in the mechanism of high-T_c superconductivity.

3.10 Conclusions

We have systematically investigated the effect of a magnetic field on the electron-doped PLCCO materials from an antiferromagnetic insulator to an optimally doped superconductor. By controlling the annealing temperatures, we obtain PLCCO samples with different T_c's and T_N's. When superconductivity first appears in PLCCO, the quasi-2D antiferromagnetic order is also induced at (0.5, 0.5, 0), and both coexist with the residual 3D antiferromagnetic state. While the annealing process also induces cubic $(Pr,La,Ce)_2O_3$ as an impurity phase similar to $(Nd,Ce)_2O_3$ in the superconducting $Nd_{1.85}Ce_{0.15}CuO_4$, we show that a magnetic field up to 14-T does not induce magnetic scattering in this impurity phase.

To determine whether the antiferromagnetic order is a competing ground state for superconductivity in the electron-doped superconductors, we must first understand the influence

of a magnetic field on the residual 3D antiferromagnetic order in the superconducting and nonsuperconducting PLCCO, without the complication of superconductivity. We confirm that a *c*-axis aligned magnetic field has no effect on the 3D antiferromagnetic order in the nonsuperconducting PLCCO. Because PLCCO is a layered superconductor with highly anisotropic B_{c2}, superconductivity can be dramatically suppressed by a *c*-axis magnetic field but affected much less by the same field in the CuO_2 plane. Utilizing this property, we determine the influence of an in-plane magnetic field on the residual 3D antiferromagnetic order in the superconducting PLCCO. We find that a 14-T field along the [-1 1 0] direction only causes a spin-flop transition but does not induce additional moments on Cu^{2+} and/or Pr^{3+} site in the superconducting PLCCO's. This suggests that the residual antiferromagnetic order in superconducting PLCCO behaves in a similar way as the 3D antiferromagnetic order in the nonsuperconducting materials.

To study the magnetic field effect on the quasi-2D antiferromagnetic modulations in the superconducting PLCCO, we conducted experiments in two ways. First, we aligned the crystal in the [*H K* 0] geometry and applied magnetic field along the *c*-axis. For both T_c = 21 K and 16 K PLCCO samples, the *c*-axis aligned field enhances the quasi-2D antiferromagnetic order at the (0.5, 0.5, 0) position but has no observable effect at the 3D antiferromagnetic order position (0.5,1.5,0). The field-induced enhancement at (0.5, 0.5, 0) increases with increasing magnetic field up to 13.5 T and seems to saturate higher fields for the T_c = 21 K sample. The T_c = 16 K sample also shows a field-induced effect at (0.5, 0.5, 0) for measured fields up to 6.8 T. Second, the crystal was aligned in the [*H H L*] scattering plane and a magnetic field was applied along the [-1 1 0] direction. In this scattering geometry, both [0.5 0.5 *L*] and [*H H* 0] radial scans around (0.5, 0.5, 0) position in the CuO_2 plane show no observable field-induced effect. This anisotropy of a field effect confirms that the enhancement of quasi-2D antiferromagnetism by a *c*-axis field is related to the suppression of superconductivity.

Our field effect results on $Nd_{1.85}Ce_{0.15}CuO_4$ and PLCCO combined with those on the hole-doped superconductors LSCO and La_2CuO_{4+y} strongly suggest that antiferromagnetism is a competing order to superconductivity in high-T_c superconductors. We hope that this universal feature can give a guide to the construction of theory in the physics of high-T_c superconductors.

Chapter 4: Spin-flop transition and the anisotropic magnetoresistance in $Pr_{1.3-x}La_{0.7}Ce_xCuO_4$

4.1 Introduction

High-T_c superconductivity in cuprates emerges when the parent antiferromagnetic insulator is doped with charge carriers, which can be either holes or electrons. Despite this apparent symmetry with respect to doping, it still remains unclear whether the mechanism of superconductivity in both cases is the same. It is generally believed that in the hole-doped cuprates, the superconducting pairing originates from the interplay between the doped holes and antiferromagnetic spin correlations. Indeed, many observations, including a fast suppression of the Néel order by doped holes [79], which result in the "spin-glass" state [79, 80, 81] and a strong tendency to form spin-charge textures or "stripes" [82], point to a very strong coupling between charge and spin degrees of freedom.

The behavior of doped electrons, however, looks much different. Electron doping suppresses the antiferromagnetic order at virtually the same slow rate as the substitution of magnetic Cu^{2+} ions with nonmagnetic Zn^{2+} [83, 84] and does not induce any incommensurability in the spin correlations [85]. This has been taken as evidence that the electrons merely dilute the spin system [79, 83, 84]. Apparently, if the charge transport and spin correlations are actually decoupled in the electron-doped cuprates, the superconducting pairing should have a nonmagnetic origin as well. A recent discovery of magnetic field-induced antiferromagnetic order in the superconducting $Nd_{1.85}Ce_{0.15}CuO_4$ has shown, however, that antiferromagnetism and superconductivity may be closely related in these compounds [72, 73].

To probe the spin-charge coupling, one can determine how the charge transport responds to such relatively weak changes in the spin structure, such as spin-flop transition. In the hole-doped $La_{2-x}Sr_xCuO_4$, for instance, the conductivity changes by up to several times [86, 87]. In this

chapter, we use neutron-scattering and magnetoresistance measurements to study the effect of magnetic field on the spin structure and anisotropic conductivity of the lightly electron-doped $Pr_{1.3-x}La_{0.7}Ce_xCuO_4$ single crystals.

4.2 Sample preparation and experimental setup

High quality $Pr_{1.29}La_{0.7}Ce_{0.01}CuO_4$ single crystals (mosaic < 1º) were grown by the traveling solvent floating zone technique and annealed at ~ 860ºC in pure argon to remove excess oxygen. The partial substitution of Pr^{3+} with La^{3+} was used to stabilize the crystal growth without introducing significant lattice distortions [47].

Neutron-scattering measurements were performed on the BT-2 and SPINS triple-axis spectrometers at the NIST Center for Neutron Research. We label wave vectors $\mathbf{Q} = (q_x, q_y, q_z)$ in units of $Å^{-1}$ and specify the reciprocal space positions $(H, K, L) = (q_x\, a/2\pi, q_y\, a/2\,\pi, q_z\, c/2\,\pi)$ in the reciprocal lattice units (r.l.u.) suitable for the tetragonal unit cell of $Pr_{1.29}La_{0.7}Ce_{0.01}CuO_4$ (space group I4/mmm, a = 3.964 and c = 12.28 Å), where a and c are in-plane and out-of-plane lattice parameters, respectively. In this notation, [100]/[010] and [110]/[110] are along the Cu-O-Cu bond direction and the diagonal Cu- Cu direction, respectively.

Resistivity measurements were carried out by the ac four-probe method on the same crystal used for neutron measurements. It was cut and polished into suitable shapes: 3.1×1×0.45 mm^3 for ρ_{ab} and 1×1×1 mm^3 for ρ_c. The magnetoresistance was measured by sweeping the magnetic field between ±14 T at fixed temperatures stabilized by a capacitance sensor with an accuracy of ~1 mK.

4.3 Neutron scattering study on the field-induced spin structure transition and magnetoresistance of $Pr_{1.29}La_{0.7}Ce_{0.01}CuO_4$

The peculiar spin structure of Pr_2CuO_4 is described in section 3.3. A strong intraplane Cu-Cu exchange drives the antiferromagnetic ordering within the CuO_2 plane, and weak interplane exchange leads to the 3D ordering below Néel temperature $T_N = 250 \sim 285$ K [51, 58, 68]. The body-centered crystal symmetry cancels out all the isotropic exchange interactions from the nearest neighboring planes. Therefore, the 3D ordering in Pr_2CuO_4 is governed by the weak pseudodipolar interactions. The pseudodipolar interaction favors a noncollinear orientation of spins in adjacent planes, alternating along [1 0 0] and [0 -1 0] directions (Fig. 4.1(a)) [51, 52, 58, 68]. A unique feature of the interplane pseudodipolar interaction is that its energy does not change when the spin sublattices of adjacent CuO_2 planes rotate in opposite directions [51, 52, 58]. Such a continuous spin rotation can be induced by a magnetic field parallel to Cu-Cu direction ([-1 1 0] direction). This easily converts the noncollinear structure of Fig. 4.1(a) into a collinear one of Fig. 4.1(b) with spins along the [1 1 0] direction. Note that, while these diagonal directions are the hard spin axes in the noncollinear phase, they become the easy axes in the collinear one.

A perfectly aligned magnetic field **B** || [0 1 0] induces a first-order transition directly to the spin-flop phase where the spin direction is perpendicular to a magnetic field [Fig. 4.1(d)]. Meanwhile, at intermediate field directions, the magnetic field first induces a transition into the collinear phase of Fig. 4.1(c) and then smoothly rotates the spins to align them perpendicular to the magnetic field [58].

We perform the neutron diffraction measurements on $Pr_{1.29}La_{0.7}Ce_{0.01}CuO_4$ to study magnetic structure and field-induced effect on it by applying in-plane magnetic field. We first align the crystal in the [*H H L*] scattering plane and measure several antiferromagnetic positions at (0.5, 0.5, *L*) (*L* = 0, 1, 2, 3, 4) as a function of temperature at a zero-magnetic field. All of these

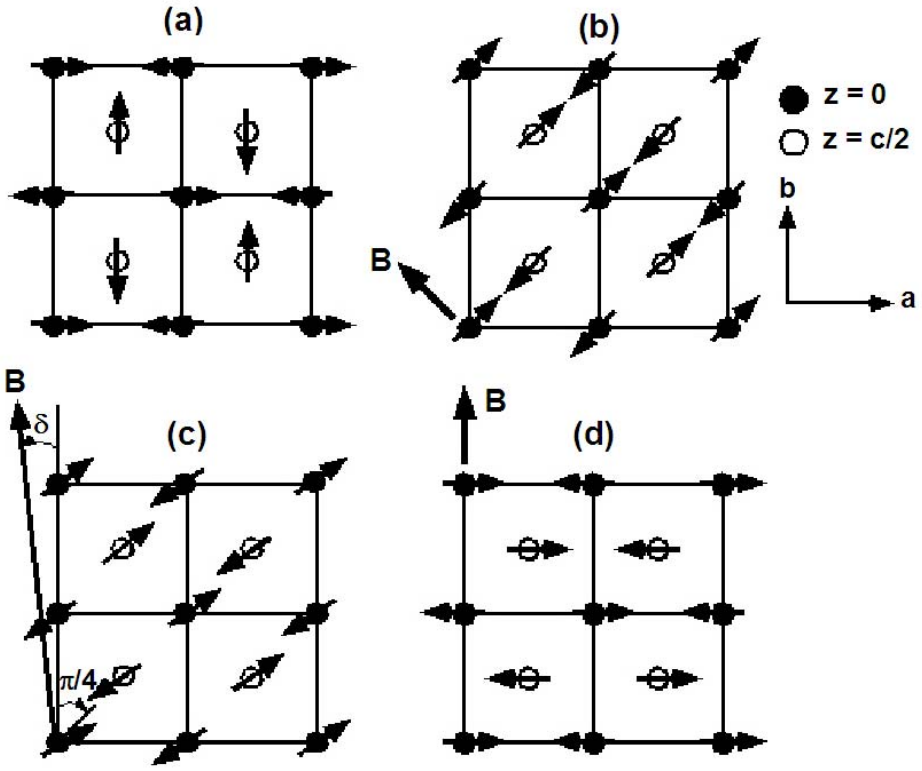

Fig. 4.1 Field-induced transition from the noncollinear Cu^{2+} spin structure to the collinear one in Pr_2CuO_4. (a) Zero-field noncollinear spin structure. (b)-(d) Collinear spin-flop states induced by (b) a magnetic field applied along the [-1 1 0] direction, (c) a magnetic field tilted from the [0 1 0], and (d) a magnetic field along the [0 1 0] direction.

peaks except (0.5, 0.5, 0) show magnetic scattering. The absence of magnetic scattering at (0.5, 0.5, 0) is expected in the noncollinear magnetic structure (See structure factor calculation in Table 3.1). The magnetic integrated intensity comparison of the (0.5, 0.5, *L*) peaks to its magnetic structure factor calculation confirms that our $Pr_{1.29}La_{0.7}Ce_{0.01}CuO_4$ has the same noncollinear structure as in Pr_2CuO_4.

Figure 4.2(a) shows the estimated Cu^{2+} and Pr^{3+} moments as a function of temperature. The ordered moments are estimated by normalizing the magnetic intensities of (0.5, 0.5, *L*) to the weak (1, 1, 0) nuclear Bragg peak. Here we calculate without considering the absorption and extinction effects of a single crystal. Similar to Pr_2CuO_4 [68], the Pr^{3+} ions in $Pr_{1.29}La_{0.7}Ce_{0.01}CuO_4$ can be polarized by the ordered Cu^{2+} moment. Upon cooling below 100 ~ 150 K, the exchange field of the Cu^{2+} spins induces a small ordered moment on the Pr^{3+} ions up to ~ 0.1 μ_B (Fig. 4.2(a)). The Pr^{3+} moment contribution can be clearly seen in the integrated intensities of (0.5, 0.5, 1) and (0.5, 0.5, 3), since Pr^{3+} moment contributes positively at (0.5, 0.5, 1) and negatively at (0.5, 0.5, 3) in magnetic structure factor calculation (Table 3.1). Fig. 4. 2(b) shows the magnetic integrated intensities of (0.5, 0.5, 1) and (0.5, 0.5, 3) peaks. The solid lines are fits using power law $I = I_0(1-T/T_N)^{2\beta}$, describing the behavior of Cu^{2+} spins as a function of temperature. The deviation of data from solid lines below 100 K shows a Pr^{3+} moment contribution. The Néel temperature of $Pr_{1.29}La_{0.7}Ce_{0.01}CuO_4$ is about 229 K somewhat lower than Pr_2CuO_4. This is probably due to a partial substitution of Pr^{3+} with nonmagnetic La^{3+}, as well as doped electrons.

Next, we applied a magnetic field along [-1 1 0] direction to study its effect on the magnetic structure. Figure 4.3 shows the effect of a magnetic field **B** || [-1 1 0] on the (0.5, 0.5, 1) and (0.5, 0.5, 2) magnetic peaks at various temperatures. Upon increasing the magnetic field, the peak intensity of (0.5, 0.5, 1) decreases and disappears with a magnetic field of 2 T (Fig. 4.3(a)). The magnetic peak of (0.5, 0.5, 2) increases with an increasing magnetic field up to 2 T and then

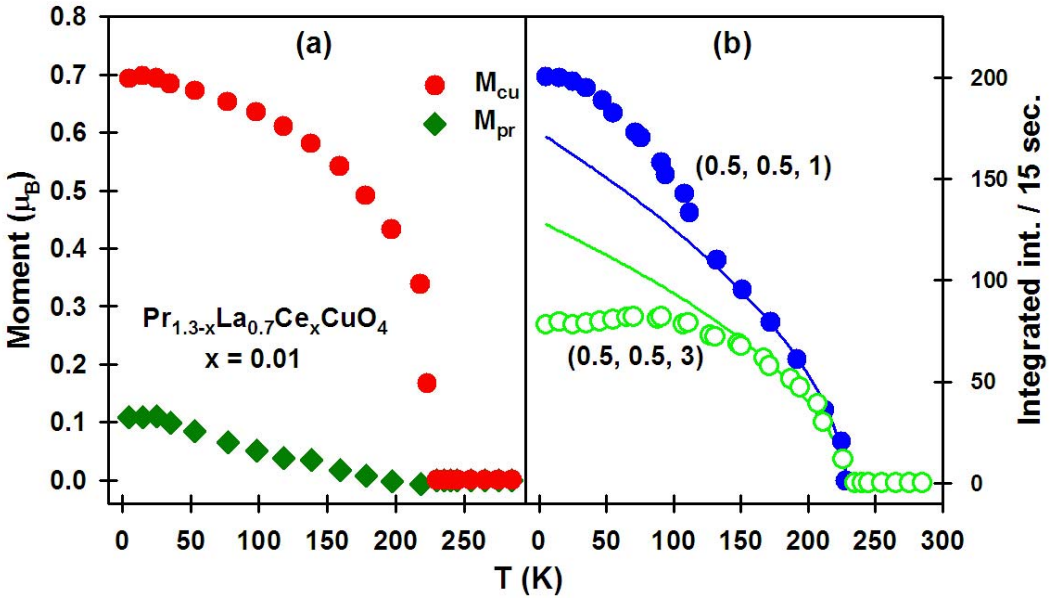

Fig. 4.2 Temperature dependence of moments and integrated intensity. (a) Temperature dependence of Cu^{2+} and Pr^{3+} moments in $Pr_{1.29}La_{0.7}Ce_{0.01}CuO_4$. (b) Integrated magnetic intensities of (0.5, 0.5, 1) and (0.5, 0.5, 3). The solid lines are power law fits describing the temperature dependence of the Cu^{2+} moment. The deviation of data from solid lines at low temperature indicates that the Pr^{3+} moment is induced.

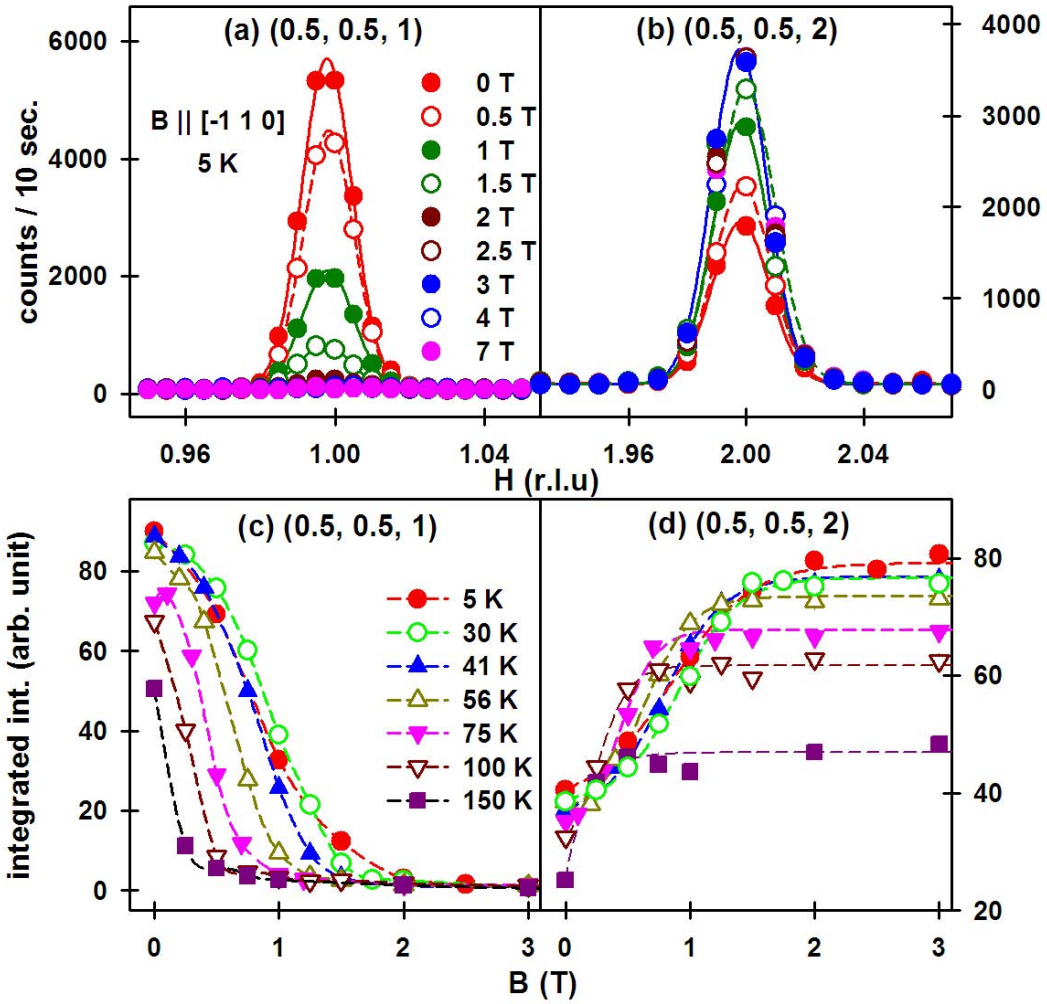

Fig. 4.3 Effect of the magnetic field **B** || [-1 1 0] on (0.5, 0.5, 1) and (0.5, 0.5, 2) magnetic peaks at 5 K. (a)-(b) Radial scans around (0.5, 0.5, 1) and (0.5, 0.5, 2) in different magnetic fields. (c)-(d) Field dependence of integrated intensities of (0.5, 0.5, 1) and (0.5, 0.5, 2) at various temperatures. We note that the critical field for the spin-flop transition in $Pr_{1.29}La_{0.7}Ce_{0.01}CuO_4$ is lower than that in Pr_2CuO_4 [68].

shows no change (Fig. 4.3(b)). This behavior of (0.5, 0.5, 1) and (0.5, 0.5, 2) magnetic intensities under a magnetic field indicates a continuous phase transition from the noncollinear structure to collinear structure. In the collinear spin arrangement shown in Fig. 4.1(b), the magnetic intensity vanishes at (0.5, 0.5, L) with L = odd integers. Figure 4.3(c) and (d) show the integrated intensities of (0.5, 0.5, 1) and (0.5, 0.5, 2) as a function of a magnetic field at different temperatures. It shows that the critical field B_{sp} for the spin-flop transition from a noncollinear to collinear structure increases from less than 0.5 T at 150 K to 2 T at 5 K.

In comparison, the first-order spin flop transition for a magnetic field **B** || [0 1 0] was reported to take place at several times larger fields [58], and a *c*-axis aligned field does not change the noncollinear spin structure [73].

4.4 Field-induced anisotropic magnetoresistance of $Pr_{1.29}La_{0.7}Ce_{0.01}CuO_4$

To study whether the magnetic structure transition induced by a magnetic field affect the in-plane and out-of-plane resistivity, we perform transport measurements under a magnetic field **B** || [-1 1 0]. Figure 4.4 shows the results of in-plane and out-of-plane resistivity measurements. The transport properties of lightly electron-doped $Pr_{1.29}La_{0.7}Ce_{0.01}CuO_4$ differ from those of hole-doped LSCO or $YBa_2Cu_3O_{6+x}$ (YBCO). In contrast to hole-doped cuprates [87, 88, 89], the doping of 1% electrons into the CuO_2 planes appears to be insufficient to induce metallic in-plane conduction in $Pr_{1.29}La_{0.7}Ce_{0.01}CuO_4$, and both ρ_{ab} and ρ_c grow upon cooling below room temperature (Fig. 4.4(a)). It is also worth noting that the lightly doped $Pr_{1.29}La_{0.7}Ce_{0.01}CuO_4$ turns out to be one of the most anisotropic cuprates with $\rho_c / \rho_{ab} \sim 8000$ at room temperature, an order of magnitude larger than LSCO and YBCO [87, 89]. In further contrast to hole-doped cuprates [87, 89], no anomaly is detected at the Néel transition in $Pr_{1.29}La_{0.7}Ce_{0.01}CuO_4$ either in the in-plane or out-of-plane resistivity. At a first glance, this supports the view that the charge motion in the electron-doped $Pr_{1.29}La_{0.7}Ce_{0.01}CuO_4$ is virtually decoupled from spin correlations. Therefore, one

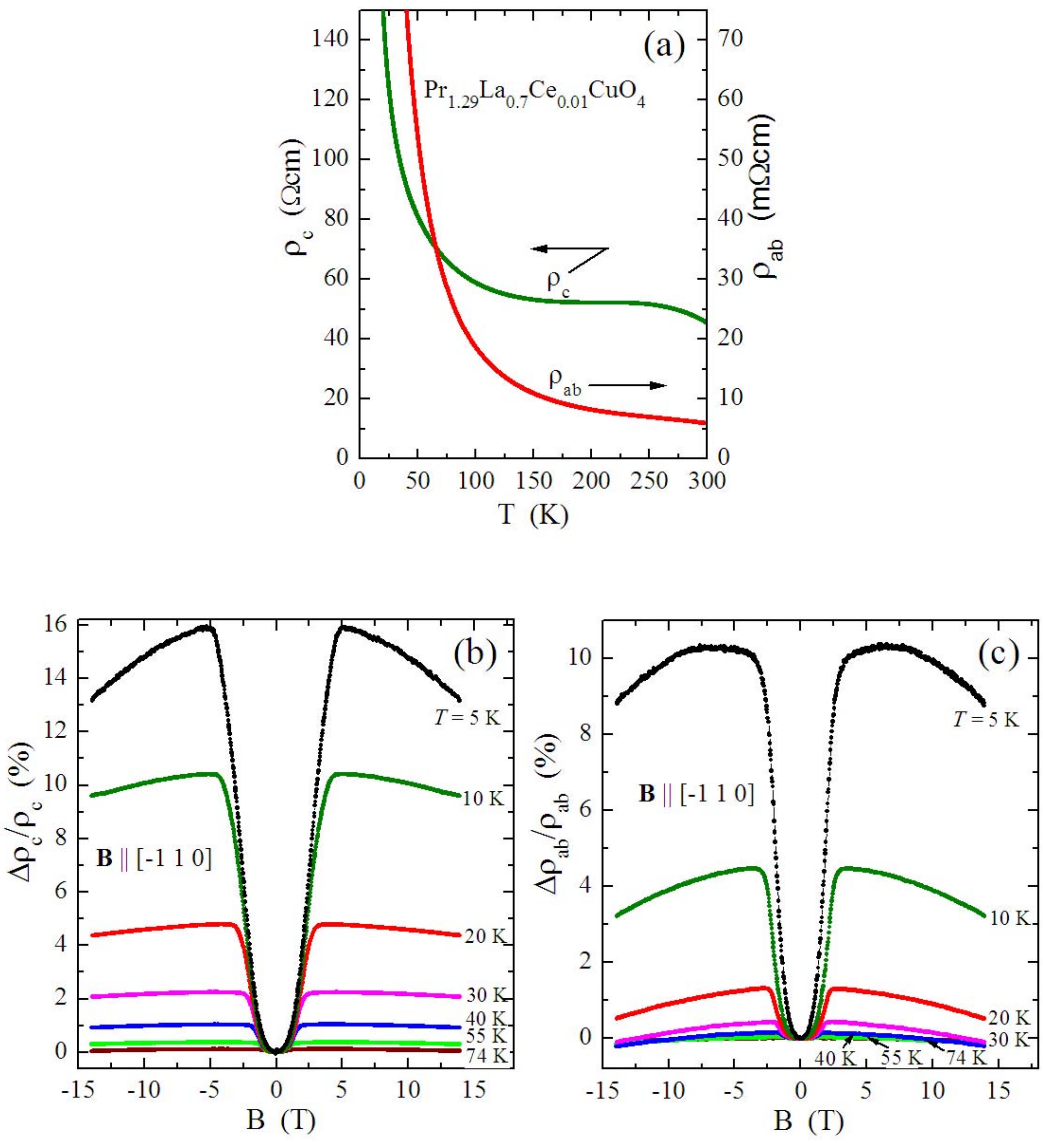

Fig. 4.4 The in-plane magnetic field effect on resistivity. (a) In-plane and out-of-plane resistivity of $Pr_{1.29}La_{0.7}Ce_{0.01}CuO_4$ single crystal. (b)-(c) The magnetoresistance in ρ_c and ρ_{ab} measured for the in-plane magnetic field **B** || [-1 1 0].

would expect the conductivity to ignore the spin reorientation sketched in Fig. 4.1. Surprisingly, the resistivity measurements show that this is not the case, and instead of being field independent, both ρ_{ab} and ρ_c exhibit a considerable increase upon transition into the collinear state [Fig. 4.4(b) and (c)]. We have confirmed that this magnetoresistance is of the spin origin and contains no orbital terms, since no difference was observed in $\Delta\rho_{ab}/\rho_{ab}$ for magnetic fields applied parallel or perpendicular to the current. Moreover, $\Delta\rho_{ab}/\rho_{ab}$ and $\Delta\rho_c/\rho_c$ demonstrate a remarkable similarity both in magnitude and in magnetic field dependence, in spite of the huge resistivity anisotropy. Finally, no magnetoresistance anomaly is observed when a *c*-axis aligned magnetic field is applied. This is consistent with the absence of a magnetic structure change for such magnetic field orientation [73].

The magnetoresistance behavior in Fig. 4.4 is clearly reminiscent of that in LSCO [87]. However, there are two important differences. First is the sign of the anomalous magnetoresistance, which is always positive in $Pr_{1.29}La_{0.7}Ce_{0.01}CuO_4$ but negative in LSCO. Second, the magnetoresistance features in LSCO and YBCO become discernible as soon as the antiferromagnetic order is established, but in $Pr_{1.29}La_{0.7}Ce_{0.01}CuO_4$ they appear at temperatures much lower than T_N (at T < 70~100 K), and quickly gain strength upon decreasing temperature (Fig. 4.4). The latter indicates that some other factors, such as magnetic moments of Pr^{3+} or a structural instability [90], that come into play at low temperature may be relevant to the observed magnetoresistance.

To study how in-plane magnetic fields affect the magnetoresistance with their direction, we apply a magnetic field [-1 1 0] and [0 1 0] directions. The results are in Fig. 4.5. Here we find one more interesting feature. A comparison of the neutron and resistivity data reveals that the spin-flop transition observed by these two probes do not match each other [inset of Fig. 4.5(a)]. One can see that the charge transport ignores the initial spin rotation, and the steepest resistivity variation is observed at B_{sp}, where the collinear structure is established. Although B_{sp} changes

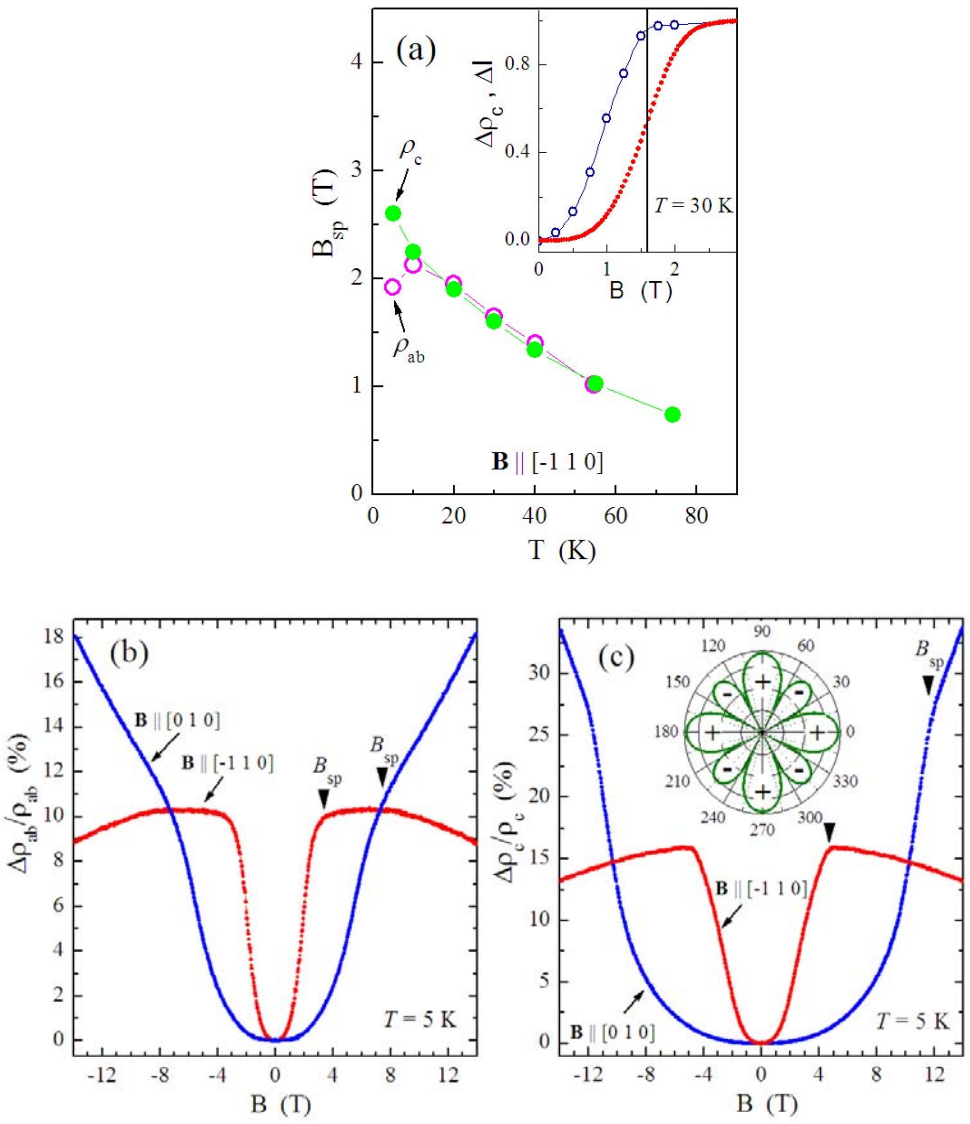

Fig. 4.5 The critical field for the spin-flop transition and the field direction dependence of resistivity. (a) The critical field B_{sp} for spin-flop transition is determined from the peaks in $d\rho_{ab}/dB$ and $d\rho_c/dB$ for a magnetic field along [-1 1 0] direction. In the inset of (a), the field dependence of ρ_c (red filled circle) is compared to that of the (0.5, 0.5, 1) integrated intensity (blue open circle) from neutron scattering. (b)-(c) $\Delta\rho_{ab}/\rho_{ab}$ and $\Delta\rho_c/\rho_c$ for a magnetic field [-1 1 0] and [0 1 0] directions. Inset of (c) The angular dependence of the high field magnetoresistance.

substantially with temperature (Fig. 5(a)), the apparent shift in the transitions holds consistently, with the peak in $d\rho/dB$ roughly coinciding with the end of the transition observed by neutron scattering. As the magnetic field deviates from the [-1 1 0] direction (Fig. 4.1(c)), the spin-flop transition shifts towards higher fields, ultimately reaching $B_{sp} \sim 12$ T for a magnetic field **B** || [0 1 0]. The magnetoresistance behavior for these two magnetic field orientations is compared in Fig. 4.5(b) and (c). For the case of a magnetic field **B** || [0 1 0], the critical field B_{sp} is extremely sensitive to the crystal alignment; just a few degrees tilting of the ρ_{ab} sample in Fig. 4.5(b) notably shifted B_{sp} to low fields, as compared to the better aligned ρ_c sample in Fig. 4.5(c).

It becomes immediately clear from these figures that the steplike increase of the resistivity upon the transition to the collinear state does not make a complete story. Regardless of the magnetic field direction within the *ab*-plane, the resistivity exhibits roughly the same increase at the spin-flop transition, but then (at $B > B_{sp}$) it keeps changing without any sign of saturation (Fig. 4.5(b) and (c)). Even more surprising is that this high magnetic field magnetoresistance changes its sign depending on the magnetic field direction, as is schematically drawn in the inset of Fig. 4.5(c). One can conceive a spin structure upon rotating the high magnetic field within the *ab*-plane in the following way: the spins always keep the collinear arrangement and rotate as a whole, being almost perpendicular to the magnetic field (Fig. 4.1). Our data show that the resistivity goes down as the spin direction approaches one of the two equivalent spin easy axes ([1 1 0] direction) and increases at the spin hard axes ([1 0 0] direction) (inset of Fig. 4.5(c)). Note that the resistivity changes are rather large; $\Delta\rho_{ab}/\rho_{ab}$ reaches $\approx 18\%$ at T = 5 K and exceeds 32% at 2.5 K. This indicates that the magnetic field **B** || [0 1 0] can effectively localize the doped electrons.

Apparently, the fascinating magnetoresistance oscillations in the inset of Fig. 4.5(c) cannot originate from simple ‘‘spin-valve’’ effects. This is because at high magnetic field the spin structure always stays collinear, and all that change is the relative orientation of spins with respect

to the crystal axes. The magnetoresistance may be related to 2D spin fluctuations that were found to survive far above B_{sp}, as manifested in the diffuse neutron scattering [91]. Or it could be due to some unusual coupling of the charge transport with low-energy spin dynamics. Though the exact mechanism of the revealed magnetoresistance features still remains to be understood, what is certain is that the charge carriers in the electron-doped cuprates appear to have a remarkably strong coupling with the spin order, which should play an important role in determining their physical properties.

A similar magnetoresistance features has been observed in $Pr_{1.85}Ce_{0.15}CuO_4$ [92]. This gives evidence that the strong spin-charge coupling survives at much higher electron-doping levels, which are relevant for the superconducting state.

Chapter 5: Doping evolution of the phonon density of states and electron-lattice interaction in $Nd_{2-x}Ce_xCuO_4$

5.1 Introduction

One of the most remarkable properties of high-T_c superconductors is their close proximity to an antiferromagnetic phase. The parent compounds of high-T_c cuprates are antiferromagnetic insulators characterized by a simple doubling of the crystallographic unit cell in the CuO_2 planes [79]. When holes or electrons are doped into these planes, the long-range antiferromagnetic ordered phase is destroyed, and the copper-oxide materials become metallic and superconducting with persistent short-range antiferromagnetic spin correlations (fluctuations). Much effort over the past decade has focused on understanding the nature of the interplay between magnetism and superconductivity [79], mainly because spin fluctuations may contribute a major part of the superconducting condensation energy [93, 94].

On the other hand, the role of phonons in the microscopic mechanism of superconductivity is still largely unknown, even though phonons in cuprates also display a variety of unusual properties [95, 96, 19, 97, 98]. The key question is whether magnetism and electron-electron correlations alone are sufficient to induce electron pairing that leads to superconductivity in high-T_c cuprates, or electron-lattice coupling also plays an important role.

From the analysis of high-resolution angle-resolved photoemission data in conjunction with those from neutron, optics and local structural probes, Shen *et al*. suggested that phonons must also play an essential role in electron pairing in high-T_c cuprates [99]. The key evidence for electron-lattice coupling, they argued [18], is that the kink (or the change of slope) seen in the electronic dispersion of the hole-doped $Bi_2Sr_2CaCu_2O_8$ (Bi2212), $Bi_2Sr_2CuO_6$ (Bi2201), and $La_{2-x}Sr_xCuO_4$ (LSCO) from the angle-resolved photoemission data [100, 101, 102, 103] occurs at an energy (~70 meV) that is very close to the phonon anomalies observed by inelastic neutron

scattering [19, 96, 97]. These phonon anomalies include the break in the dispersion of the oxygen half-breathing mode in $La_{1.85}Sr_{0.15}CuO_4$ [96] and the abrupt development of oxygen lattice vibrations near the doping-induced metal-insulator transition in the generalized phonon density of states (GDOS) of LSCO [19, 104]. Since the change of slope in the electronic dispersion indicates a dramatic drop in the ‘‘quasiparticle’’ scattering rate [99], these observations in the hole-doped superconductors suggest a strong coupling between the quasiparticles and a sharp collective-spin or lattice mode [100, 101, 102, 103]. Although the neutron magnetic resonance [94] could be the collective spin mode coupled to the quasiparticles [103,105], Shen *et al*. argued that electron-lattice interaction is ultimately responsible for the quasiparticle velocity change, and thus is crucial to the high-T_c superconductivity [18, 99]. Furthermore, the dispersion of the electron-doped superconducting $Nd_{1.85}Ce_{0.15}CuO_{4+\delta}$ does not have such a kink. Therefore, the authors [99] predict that the electron-doped materials have much weaker electron-lattice coupling and thus lower T_c's.

If this hypothesis were correct, one would expect the exotic lattice dynamics seen in the hole-doped LSCO [19, 96, 97] to be reduced in the electron-doped $Nd_{2-x}Ce_xCuO_{4+\delta}$. For LSCO, the abrupt development of oxygen lattice vibrations across the doping-induced nonsuperconducting-superconducting transition (NST) was interpreted as evidence of strong electron-lattice coupling in the superconducting cuprates that is not present in the nonsuperconducting materials [19, 104]. Specifically, the lattice mode at ~70 meV in the GDOS is believed to be at least partly comprised of the anomalous Cu-O bond-stretching (oxygen half-breathing) mode [19]. Although GDOS for $Nd_{2-x}Ce_xCuO_{4+\delta}$ with x =0 and 0.15 were studied by Lynn and coworkers [106, 107], no systematic doping dependent measurements has been performed. If the quasiparticle velocity drop seen in the angle-resolved photoemission data of hole-doped cuprates is related to the anomalous lattice vibrational modes, the absence of such a

drop in the electron-doped superconducting $Nd_{2-x}Ce_xCuO_{4+\delta}$ with x = 0.15 would suggest a weak (or no) phonon anomaly in $Nd_{2-x}Ce_xCuO_{4+\delta}$.

In this chapter, we present inelastic neutron scattering measurements of the GDOS in $Nd_{2-x}Ce_xCuO_{4+\delta}$ by changing electron-doping concentrations from the half-filled Mott-insulator (Nd_2CuO_4) to an optimally doped superconductor $Nd_{2-x}Ce_xCuO_{4+\delta}$ (x = 0.15).

5.2 Sample preparation and experimental setup

We prepared the ceramic samples of $Nd_{2-x}Ce_xCuO_{4+\delta}$ with Ce concentrations of x = 0, 0.04, 0.08, 0.09, 0.10, 0.11, 0.12, 0.13, and 0.15 by a conventional solid-state reaction [108]. The as-grown samples have excess oxygen ($\delta > 0$) and are nonsuperconducting. Various annealing procedures were developed to remove the excess oxygen and produce superconductivity. However, the properties of the samples and the resulting electronic phase diagrams are different depending on the details of the annealing procedure used. In the original work of Takagi *et al*. [108], it was found that samples treated in flowing argon at temperatures in excess of 1100°C followed by heating in air at 500°C produced metallic samples with a sharp superconducting transition. However, it was also found that this procedure resulted in some decomposition of the sample as well as probable loss of Cu from the surfaces of the polycrystalline grains [108]. This procedure also results in an electronic phase diagram showing an abrupt NST around x = 0.14 with only half of the superconducting ‘‘dome’’ [108]. This is different from hole-doped LSCO [79]. Therefore, we have followed the annealing procedure developed by Maple’s group [109], where the samples are treated in flowing argon at a temperature of about 900°C. The resulting phase diagram shows a NST around x = 0.12 with the almost complete superconducting dome [109] as compared to the half-dome from Ref. [108].

To characterize the materials, bulk magnetization and resistivity measurements were performed for all the samples. Figure 5.1 shows the doping dependence of the ac susceptibility

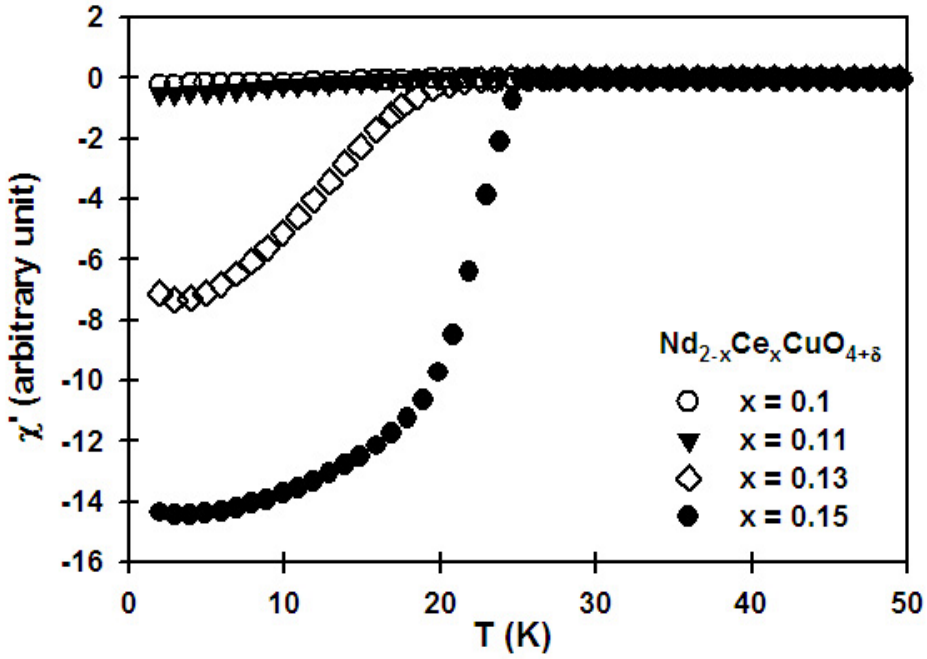

Fig. 5.1 Temperature dependence of the ac magnetic susceptibility χ' (real part) for $Nd_{2-x}Ce_xCuO_{4+\delta}$ powder samples used in the neutron measurement. The background was subtracted using χ' for $x = 0.09$, which shows a Curie-Weiss-like behavior down to the lowest temperature measured. The diamagnetic signal first appears for $x \geq 0.11$.

for x = 0.1, 0.11, 0.13, and 0.15. Superconductivity is clearly seen in $Nd_{2-x}Ce_xCuO_{4+\delta}$ with $x \geq 0.13$, thus confirming that the NST in $Nd_{2-x}Ce_xCuO_{4+\delta}$ occurs around $x \approx 0.12$ [109].

Our experiments were performed on the MARI chopper spectrometer at ISIS facility, Rutherford Appleton Laboratory, UK. The detectors on MARI cover a wide scattering angle from 3° to 135°. For the experiments, we used a Fermi chopper to choose incident beam energy of 110 meV. The energy resolution is between 1 ~ 2% of the incident energy. The powder samples were mounted inside an aluminum sample can on the cold head of a helium closed-cycle refrigerator, and all measurements were performed at T = 30 K. The incident neutron beam size was 5 X 5 cm^2 and the unexposed area of the sample was covered by cadmium sheets. To normalize the scattering from $Nd_{2-x}Ce_xCuO_{4+\delta}$ in an absolute scale, we used the elastic incoherent scattering from vanadium standard. In addition to measurements at MARI, we also collected data on the BT-4 filter analyzer spectrometer at the NIST Center for Neutron Research. To within the error of the measurements, the results of these two experiments are identical.

5.3 Inelastic neutron scattering on phonon density of states in $Nd_{2-x}Ce_xCuO_{4+\delta}$

In an unpolarized neutron experiment, the major difficulty in obtaining the reliable GDOS is to separate phonons from the magnetic scattering. For $Nd_{2-x}Ce_xCuO_{4+\delta}$, the largest magnetic signal originates from single-ion crystalline electric field (CEF) excitations of the Nd^{3+} ions [106, 107]. The CEF excitations of $Nd_{2-x}Ce_xCuO_{4+\delta}$ with x = 0 and 0.15 have been studied in great detail, and their level scheme has peaks around $\hbar\omega$ = 12~16, 20.5, 27, and 93.3 meV at low temperatures [110]. We performed a careful wave vector (**Q**) dependent analysis of the excitation intensities at $\hbar\omega$ = 20.5, 27, and 93.3 meV for 2 $Å^{-1}$ < **Q** <10 $Å^{-1}$. The outcome confirms the earlier results that these three peaks are magnetic in origin and the phonon cut-off energy of $Nd_{2-x}Ce_xCuO_{4+\delta}$ is around 83 meV [107]. We also checked the strength of the multiple scattering and multi-phonon scattering using the Monte Carlo simulation program MSCAT, and found that such

multi-phonon scattering makes monotonic contributions to the total scattering intensity in the energy region of interest.

To reduce the magnetic scattering contribution to the GDOS, we replaced the intensities of the 20.5 and 27 meV peaks with scattering from the highest measured wave vectors (9 $Å^{-1}$ < **Q** <11 $Å^{-1}$). Although this procedure may not eliminate all the magnetic intensity, there are no magnetic contributions to the GDOS for 50 meV ≤ $\hbar\omega$ ≤ 80 meV.

After subtraction of the empty aluminum sample can, multiple and multi-phonon scattering, the single-phonon GDOS with **Q** values integrated from 3 to 11 $Å^{-1}$ were calculated by multiplying $\omega/(n(\omega)+1)$, where $n(\omega)$ is the Bose population factor. The total area of each GDOS was then normalized to 1 over the energy range from 15 to 80 meV. Figure 5.2 shows the GDOS for $Nd_{2-x}Ce_xCuO_{4+\delta}$ with x = 0.0, 0.04, 0.08, 0.10, 0.11, 0.12, 0.13, and 0.15. Consistent with previous measurements on $Nd_{2-x}Ce_xCuO_{4+\delta}$ for x = 0.0 and 0.15 [106, 107], the spectra contains clear peaks at ~36, 42, 48, and 65~70 meV. On moving from an insulator to a metal with increasing Ce concentration, the largest observed effect is the softening and sharpening of the broad ~70-meV phonon band in the undoped Nd_2CuO_4.

We systematically fit the 70-meV phonon band with two Gaussians on a sloping background for various x. The solid lines in Fig. 5.2 show the outcome of the fits. Although the precise functional form of the GDOS for the 70-meV phonon band is not known, the systematic Gaussian fits allow a quantitative determination for the magnitude of the phonon softening. For the undoped Nd_2CuO_4, the 70-meV mode shows a flattish top and can be best fitted by two Gaussians centered at 67 and 71 meV, respectively. On increasing the Ce concentration to x = 0.04, the 71-meV mode softens to 67 meV (6% softening) and shows less of a flattish top.

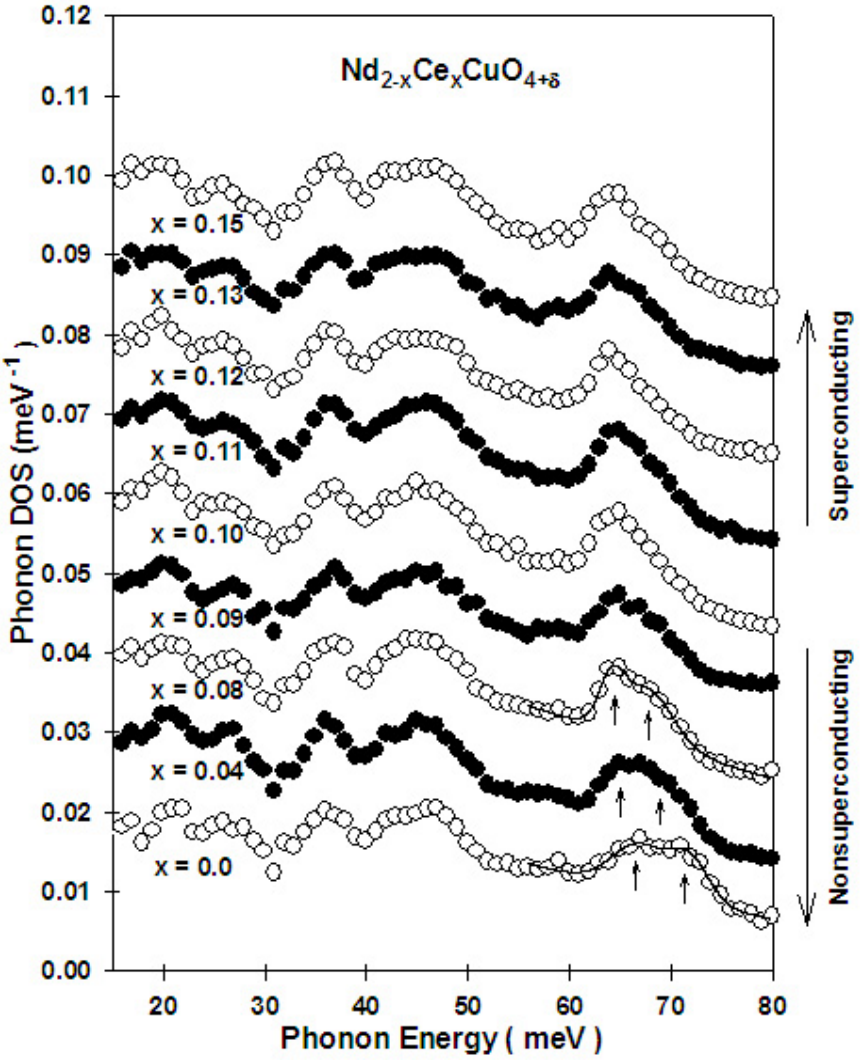

Fig. 5.2 The GDOS of $Nd_{2-x}Ce_xCuO_{4+\delta}$ as a function of x at T = 30 K. Each GDOS is displaced along the vertical axis for clarity, and the solid lines are Gaussian fits discussed in the text. The nonsuperconducting-superconducting transition as a function of x is schematically shown on the right.

Furthermore, the GDOS gains intensity at 65 meV at the expense of the 71-meV peak. At x = 0.08, the GDOS peaks more sharply at 65 meV. On further increasing x and across the NST at x = 0.12, the GDOS show essentially no change from that for x = 0.08 to within the error of the measurements.

Figure 5.3 shows comparison plots of the GDOS at various x. For $Nd_{2-x}Ce_xCuO_{4+\delta}$ with $0.0 \leq x \leq 0.08$, the 70-meV phonon band shows significant softening while all other modes display no visible change with increasing x (Fig. 5.3(a) and (b)). The GDOS for $0.08 \leq x \leq 0.15$ (Fig. 5.3(c) and (d)) overlap completely in the probed energy range 15 meV $\leq \hbar\omega \leq$ 80 meV, and show no changes across the NST.

To understand the atomic displacement patterns of the phonon modes contributing to the 70-meV band in Nd_2CuO_4, we consider the experimentally determined phonon dispersion curves [111]. For Nd_2CuO_4, the highest energy phonon bands are around 70 meV [111]. These include the highest energy in-plane Cu-O bond-stretching mode with Δ_1 symmetry at **Q** = (0.5, 0, 0) (the oxygen half-breathing mode) along the [ζ 0 0] direction, the out-of-plane (*c*-axis-polarized) oxygen breathing mode with Λ_1 symmetry along [0 0 ζ], and the in-plane oxygen breathing mode with Σ_1 symmetry at **Q** = (0.5, 0.5, 0) along [ζ ζ 0]. Figure 5.4 shows the oxygen displacement patterns for these three modes. Since these three modes are at ~70 meV in the dispersion curves [111], the 70-meV peak in the GDOS of Nd_2CuO_4 must consist, at least partially, of these modes. As a consequence, the electron doping-induced softening in $Nd_{2-x}Ce_xCuO_{4+\delta}$ must also occur in these modes.

In a very recent inelastic X-ray scattering study of longitudinal optical phonons in $Nd_{2-x}Ce_xCuO_{4+\delta}$ with x = 0.14, d'Astuto *et al*. discovered anomalous phonon softening in the two highest longitudinal branches associated with the Cu-O bond-stretching and out-of-plane oxygen

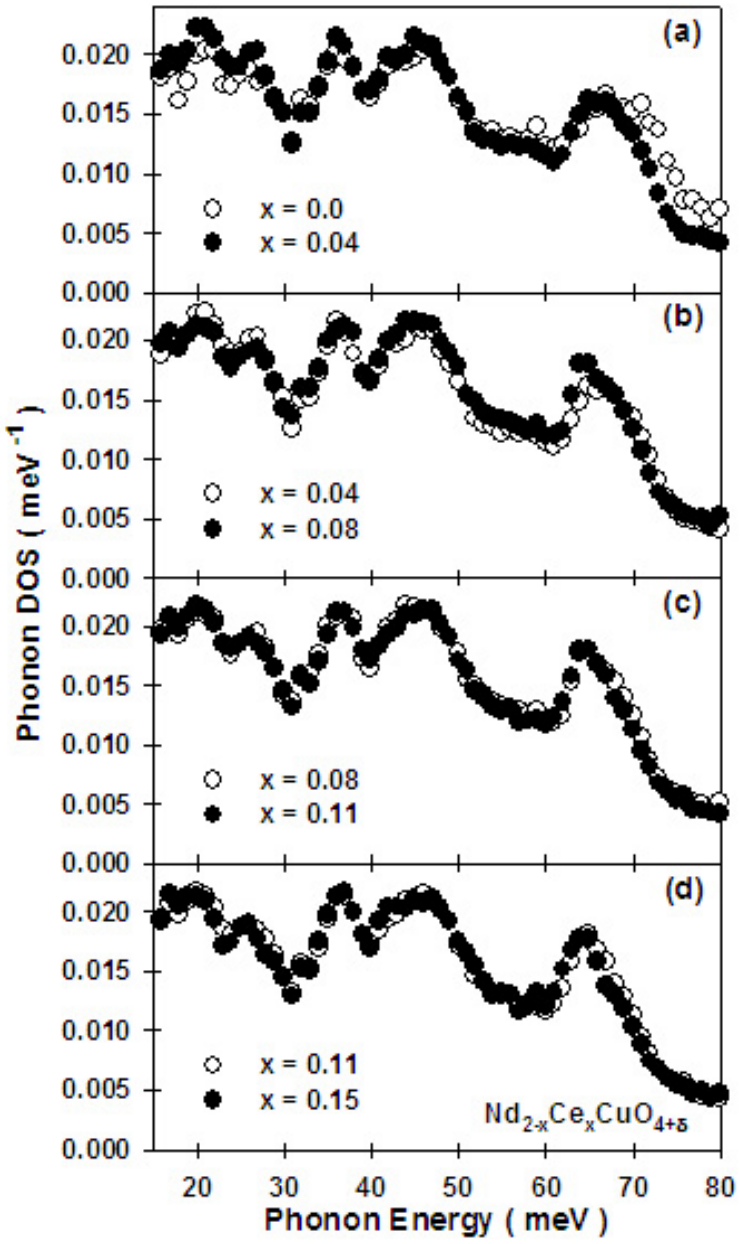

Fig. 5.3 Comparison of the GDOS of $Nd_{2-x}Ce_xCuO_{4+\delta}$ as a function of electron-doping level x. The GDOS of $Nd_{2-x}Ce_xCuO_{4+\delta}$ for (a) x = 0 and 0.04, (b) x = 0.04 and 0.08, (c) x = 0.08 and 0.11, and (d) x = 0.11 and 0.15.

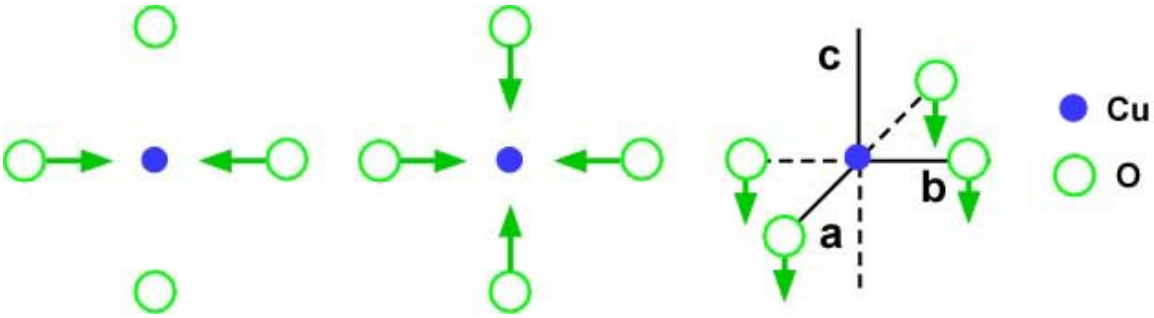

Fig. 5.4 Oxygen vibration modes. Half-breathing mode (left), breathing mode (middle), and out-of-plane vibration mode (right).

vibrations [112]. By comparing their data on $Nd_{2-x}Ce_xCuO_{4+\delta}$ with undoped Nd_2CuO_4, the authors concluded that strong electron-phonon coupling is also present in electron-doped $Nd_{2-x}Ce_xCuO_{4+\delta}$. From their work [112], it becomes clear that the significant softening of the 70-meV phonon band with x in Fig. 5.2 and 5.3 is mostly due to a softening of the oxygen half-breathing and out-of-plane vibration modes.

For hole-doped LSCO, the oxygen half-breathing modes display an anomalous behavior [96, 97], and show up as lattice modes in the superconducting side of the phase diagram across the NST [19]. While the oxygen half-breathing modes also exhibit an anomalous behavior [112] and soften with increasing electron doping, our results indicate that most of the softening occurs within the first few percent of Ce doping in the nonsuperconducting regime, and therefore is not associated with the electron-doping induced NST in $Nd_{2-x}Ce_xCuO_{4+\delta}$.

For hole-doped cuprates, previous investigations established a clear correlation between superconducting properties of the materials and special features of the phonon spectrum. While such a correlation is seen as anomalous phonon modes across the NST in LSCO [19], systematic

studies of the GDOS in $YBa_2Cu_3O_{6+x}$ showed that the phonon cut-off energy softens across the NST and is closely related to T_c [95]. In general, these phonon anomalies are related to the dielectric screening properties of metals, and thus suggest a strong electron-lattice coupling in the superconductivity of the hole-doped materials. This is particularly evident in $YBa_2Cu_3O_{6+x}$ where the cut-off energy of the GDOS does not decrease with increasing oxygen content x (in the nonsuperconducting $YBa_2Cu_3O_{6+x}$) until the material becomes superconducting with $x \leq 0.4$ (see Fig. 41 of Ref. [95]). Although phonon softening is also observed in the electron-doped $Nd_{2-x}Ce_xCuO_{4+\delta}$, our data indicate that most of the softening occurs in the nonsuperconducting regime and is not directly related to the NST. Therefore, it becomes clear that the electron-lattice coupling in the electron-doped $Nd_{2-x}Ce_xCuO_{4+\delta}$ is different from that in the hole-doped materials.

It is interesting to compare our results with that of the angle-resolved photoemission on $Nd_{2-x}Ce_xCuO_{4+\delta}$. In principle, the strong electron-lattice coupling and large softening of the optical oxygen vibration modes in $Nd_{2-x}Ce_xCuO_{4+\delta}$ with $x = 0.04$ should reveal themselves as distinctive features in the angle-resolved photoemission spectra [99]. If the kink in the electronic band dispersion in the hole-doped materials is due to the anomalous softening of the 70-meV oxygen half-breathing mode [99], its absence in the electron-doped $Nd_{2-x}Ce_xCuO_{4+\delta}$ would suggest no softening of such oxygen modes in $Nd_{2-x}Ce_xCuO_{4+\delta}$. Clearly, this is inconsistent with the results of Ref. [112] and the present work. On the other hand, if the kink in the angle-resolved photoemission spectra is not related to the softening of the 70-meV modes but to the changes of such modes across the hole- (electron-) induced NST, our data would be consistent with a weaker electron-lattice coupling in $Nd_{2-x}Ce_xCuO_{4+\delta}$ and a phonon origin for the drop in the ‘‘quasiparticle’’ scattering rate in the hole-doped cuprate superconductors [99]. An unambiguous test of this idea will require a comparison of the neutron data with the doping dependence of the electronic structure of $Nd_{2-x}Ce_xCuO_{4+\delta}$. Although systematic angle-resolved photoemission investigations were carried out very recently on $Nd_{2-x}Ce_xCuO_{4+\delta}$ [113], the evolution of the

electronic dispersions across the metal-insulator transition or NST is unavailable and therefore cannot be compared yet with the neutron results.

Chapter 6: Conclusion

The discovery of high temperature superconductivity in cuprates has produced intensive work to understand the mechanism of superconductivity in these materials. In both conventional superconductors and high temperature superconductors, it is now accepted that the electrons form Cooper pairs by overcoming the Coulomb repulsive force between them. The attractive force binding the Cooper pairs together is the electron-phonon coupling in conventional low temperature superconductors and it is explained well by BCS theory. However, the electron-phonon coupling alone cannot explain high transition temperature in cuprates. Therefore, people have been searching for other possibilities that are responsible for the pairing in high temperature superconductivity.

One of the candidates is magnetism, since all of the high temperature cuprates have antiferromagnetic insulator in their parent compounds. Another candidate is the electron-phonon coupling. Although it may not be responsible completely, it may contribute partly. Consequently, we have studied these two properties in electron-doped $Nd_{2-x}Ce_xCuO_4$ and $Pr_{1-x}LaCe_xCuO_{4\pm\delta}$.

Our study on magnetism in the electron-doped materials is motivated by the discovery of the 2D incommensurate spin density waves (SDW) in the hole-doped $La_{2-x}Sr_xCuO_4$ and La_2CuO_{4+y} in the superconducting regime. This coexisting SDW with superconductivity is enhanced by a *c*-axis magnetic field above T_c of zero-field, but not by an *ab*-plane magnetic field. These results strongly indicate that the enhancement of SDW is from the suppression of superconductivity, and thus the antiferromagnetic order coexisting with superconductivity also competes with superconductivity. To check if this is fundamental feature of cuprates, we perform comprehensive neutron scattering studies on the electron-doped $Nd_{2-x}Ce_xCuO_4$ and $Pr_{1-x}LaCe_xCuO_{4\pm\delta}$ materials.

The parent compound Nd_2CuO_4 has a noncollinear magnetic structure, and it has phase transitions as a function of temperature; type-I (75 K < T < 275 K), type-II (30 K < T < 75 K), and type-III (T < 30 K) phases. An as-grown nonsuperconducting sample has the type-I/III phase. The *c*-axis magnetic field does not affect the antiferromagnetic order or magnetic structure in the Nd_2CuO_4 parent and as-grown $Nd_{1.85}Ce_{0.15}CuO_4$ samples.

For an optimally doped superconducting $Nd_{1.85}Ce_{0.15}CuO_4$ sample (T_c = 25 K), we find that a 3D commensurate antiferromagnetic order coexists with superconductivity. It orders with the same magnetic structure seen in the as-grown sample, but with much lower Néel temperature. The antiferromagnetic order is enhanced by a *c*-axis magnetic field. Meanwhile, the *ab*-plane magnetic field induces the spin-flop transition from the noncollinear structure to the collinear one. This result supports that the antiferromagnetic order is a competing order in electron-doped superconductors.

Although the enhancement of antiferromagnetic order by a *c*-axis magnetic field in the superconducting $Nd_{1.85}Ce_{0.15}CuO_4$ is very encouraging, there is one problem in this system. The annealing process that is required to achieve superconductivity also induces the cubic $(Nd,Ce)_2O_3$ as an impurity phase. $(Nd,Ce)_2O_3$ is lattice matched with $Nd_{1.85}Ce_{0.15}CuO_4$ in the CuO_2 plane. Since Nd^{3+} in $(Nd,Ce)_2O_3$ has a magnetic ground state, a *c*-axis magnetic field on $Nd_{1.85}Ce_{0.15}CuO_4$ also induces paramagnetic scattering from the $(Nd,Ce)_2O_3$ at the antiferromagnetic positions, such as (0.5, 0.5, 0).

To resolve this impurity problem, we applied a magnetic field along a *c*-axis and probed the *L* direction using a horizontal field magnet. This is because the lattice mismatch of the impurity along *c*-axis gives incommensurate peak in $Nd_{1.85}Ce_{0.15}CuO_4$ along *L* direction, for example (0.5, 0.5, *L*) *L* = 2.2, 4.4, and so on. The antiferromagnetic peak (0.5, 0.5, 3) is enhanced by a *c*-axis magnetic field, while the peak (0.5, 0.5, 4.4) that is coming from the impurity reflection $(2, 0, 4)_c$ is not affected by the same magnetic field. These results clearly demonstrate

that the *c*-axis magnetic field effect in superconducting $Nd_{1.85}Ce_{0.15}CuO_4$ is a generic property and not an impurity effect.

To study the inherent magnetic property of Cu^{2+} that is free from rare earth moment contribution, we study another electron-doped $Pr_{1-x}LaCe_xCuO_{4\pm\delta}$ system. We can resolve the impurity problem in this system, because the Pr^{3+} has a nonmagnetic ground state. First, we studied the evolution of magnetism and superconductivity from the phase boundary region to full superconducting region in the phase diagram at a zero-field by using different annealing temperature to control magnetism and superconductivity. We find that a quasi-2D antiferromagnetic order coexists with superconductivity and the 3D antiferromagnetic order in underdoped region. The 2D and 3D antiferromagnetism disappears in the optimally doped sample. We also find that the induced Pr^{3+} moment that is negligible in the superconducting sample makes a contribution in the nonsuperconducting sample at low temperature. In addition, the Néel temperature is decreasing with increasing T_c and disappears when the maximum T_c is achieved. This suggests that the electron-doped superconductors are close to a quantum critical point, where the delicate energetic balance between competing phases leads to microscopic inhomogeniety. The existence of a quasi-2D antiferromagnetic order in the underdoped superconductors is very similar to the SDW in $La_{2-x}Sr_xCuO_4$.

When a magnetic field is applied along the [-1 1 0] direction parallel to the CuO_2 plane, it transforms the noncollinear spin structure to a collinear one, so-called ``spin-flop'' transition. This spin-flop transition is continuous and second-order-like in the parent and nonsuperconducting $Pr_{1-x}LaCe_xCuO_{4\pm\delta}$, but gradually changes to be first-order-like with increasing doping levels and the appearance of superconductivity. This in-plane field does not induce the quasi-2D antiferromagnetic order or polarize the Pr^{3+} moment up to 14T.

On the other hand, a *c*-axis aligned magnetic field enhances the quasi-2D antiferromagnetic order at (0.5, 0.5, 0) in the underdoped $Pr_{1-x}LaCe_xCuO_{4\pm\delta}$, but has no effect on

the 3D antiferromagnetic order in the nonsuperconducting and superconducting samples. Since the same field along the [-1 1 0] direction has no effect on (0.5, 0.5, 0) and $(Pr,La,Ce)_2O_3$ impurity positions, we conclude that the *c*-axis field-induced effect is intrinsic to $Pr_{1-x}LaCe_xCuO_{4\pm\delta}$ and arises from the suppression of superconductivity.

In conclusion, our field effect results on $Nd_{1.85}Ce_{0.15}CuO_4$ and $Pr_{1-x}LaCe_xCuO_{4\pm\delta}$ combined with those on the hole-doped superconductors $La_{2-x}Sr_xCuO_4$ and La_2CuO_{4+y} strongly suggest that the antiferromagnetic order is a competing order to superconductivity in high temperature superconductors.

For the hole-doped cuprates, it is believed that the superconducting pairing is related to the coupling between doped charge carriers and antiferromagnetic spin fluctuations. Fast suppression of antiferromagnetism in the hole-doped cuprates is one of the evidence for this coupling. However in the electron-doped case the antiferromagnetic order is very robust up to high doping levels. This seems to suggest that charges and spins are decoupled in the electron-doped cuprates. On the other hand, the magnetic field effects on $Nd_{1.85}Ce_{0.15}CuO_4$ and $Pr_{1.88}LaCe_{0.12}CuO_{4\pm\delta}$ clearly show that antiferromagnetism and superconductivity is related.

To probe the spin-charge coupling, we measure how resistivity changes with a small spin structure change, such as a spin-flop transition. We find that the spin-flop transition induced by an *ab*-plane magnetic field in the lightly electron-doped $Pr_{1.29}LaCe_{0.01}CuO_4$ affects significantly both in-plane and out-of-plane resistivity. However, a *c*-axis magnetic field does not induce the magnetoresistance anomaly. This is consistent with the absence of a spin-flop transition for such magnetic field direction. This anisotropic magnetoresistance effect suggests that there is spin-charge coupling in the electron-doped cuprates as well as in the hole-doped ones.

The electron-phonon coupling is observed in several hole-doped materials by angle-resolved photoemission and neutron scattering. The kink in dispersion curve of these materials around ~70 meV occurs at an energy of new oxygen lattice mode near the metal-insulator

transition in the hole-doped $La_{2-x}Sr_xCuO_4$. This motivated us to study the evolution of the generalized phonon density of states (GDOS) in electron-doped $Nd_{2-x}Ce_xCuO_4$. We found that a few percent of electron doping softens the highest phonon branch of 70 meV and GDOS shows no change across the nonsuperconducting-superconducting transition. These results indicate that the electron-lattice coupling in the electron-doped superconductors is different from that in the hole-doped superconductors.

I hope that our work on magnetism and electron-phonon coupling in electron-doped superconductors has made a contribution to the body of knowledge that can explain the physics of high temperature superconductivity.

References

1. H. Kamerlingh Onnes, Akad. van Wetenschappen (Amsterdam) 14(113), 818 (1911).

2. W. Meissner and R. Ochsenfeld, Naturwiss. 21, 787 (1933).

3. J. Bardeen, L. N. Cooper, and J.R. Schrieffer, Phys. Rev. 106, 162 (1957); 108, 1175 (1957).

4. J. G. Bednorz and K. A. Müller, Z. Phys. B 64, 189 (1986).

5. M. K. Wu, J. R. Ashburn, C. J. Torng, P. H. Hor, R. L. Meng, L. Gao, Z. J. Huang, Y. Q. Wang, and C. W. Chu, Phys. Rev. Lett. 58, 908 (1987).

6. A. Schilling, M. Cantoni, J. D. Guo, and H. R. Ott, Nature 363, 56 (1993).

7. B. Keimer, N. Belk, R. J. Birgeneau, A. Cassanho, C. Y. Chen, M. Greven, M. A. Kastner, A. Aharony, Y. Endoh, R. W. Erwin, and G. Shirane, Phys. Rev. B 46, 14034 (1992).

8. S. Wakimoto, G. Shirane, Y. Endoh, K. Hirota, S. Ueki, K. Yamada, R. J. Birgeneau, M. A. Kastner, Y. S. Lee, P. M. Gehring, and S. H. Lee, Phys. Rev. B 60, R769 (1999).

9. S. Wakimoto, R. J. Birgeneau, M. A. Kastner, Y. S. Lee, R. Erwin, P. M. Gehring, S. H. Lee, M. Fujita, K. Yamada, Y. Endoh, K. Hirota, and G. Shirane. Phys. Rev. B 61, 3699 (2000).

10. M. Matsuda, M. Fujita, K. Yamada, R. J. Birgeneau, Y. Endoh, and G. Shirane, Phys. Rev. B 65, 134515 (2002).

11. M. Fujita, K. Yamada, H. Hiraka, P. M. Gehring, S. H. Lee, S. Wakimoto, and G. Shirane, Phys. Rev. B 65, 064505 (2002).

12. H. Kimura, K. Hirota, H. Matsushita, K.Yamada, Y. Endoh, S-H Lee, C. F. Majkrzak, R. Erwin, M. Greven, Y. S. Lee, M. A. Kastner, and R. J. Birgeneau, Phys. Rev. B 59, 6517 (1999).

13. T. Suzuki, T. Goto, K. Chiba, T. Shinoda, T. Fukase, H. Kimura, K. Yamada, M. Ohashi, and Y. Yamaguchi, Phys. Rev. B 57, 3229 (1998).

14. B. Lake, H. M. Ronnow, N. B. Christensen, G. Aeppli, K. Lefmann, D. F. McMorrow, P. Vorderwisch, P. Smeibidl, N. Mangkorntong, T. Sasagawa, M. Nohara, H. Takagi, and T. E. Mason, Nature 415, 299 (2002).

15. B. Lake, G. Aeppli, K. N. Clausen, D. F. McMorrow, K. Lefmann, N. E. Hussey, N. Mangkorntong, N. Nahara, H. Takagi, and T. E. Mason, Science 291, 1759 (2001).

16. Shou-Cheng Zhang, Science 275, 1089 (1997).

17. Daniel P. Arovas, A. J. Berlinsky, C. Kallin, and Shou-Cheng Zhang, Phy. Rev. Lett. 79, 2871 (1997).

18. A. Lanzara, P. V. Bogdanov, X. J. Zhou, S. A. Kellar, D. L. Feng, E. D. Lu, T. Yoshida, H. Eisaki, A. Fujimori, K. Kishio, J.-I. Shimoyama, T. Noda, S. Uchida, Z. Hussain, and Z.-X. Shen, Nature 412, 510 (2001).

19. R. J. McQueeney, J. L. Sarrao, P. G. Pagliuso, P.W. Stephens, and R. Osborn, Phys. Rev. Lett. 87, 077001 (2001).

20. Z.-X. Shen, A. Lanzara, S. Ishihara, and N. Nagaosa, cond-mat/0108381 (unpublished).

21. Stephen W. Lovesey, The Theory of Neutron Scattering from Condensed Matter (Volumes I and II), Oxford University Press, New York (1986).

22. G. L. Squires, Introduction to the Theory of Thermal Neutron Scattering, Dover Publications, INC. (1996).

23. G. Shirane, S. M. Shapiro, and J. M. Tranquada, Neutron Scattering with a Triple-Axis Spectrometer: Basic Techniques, Cambridge University Press (2002).

24. S. Sachdev and S.-C. Zhang, Science 295, 452 (2002).

25. B. G. Levi, Physics Today 57, 24 (2004).

26. Y. S. Lee, R. J. Birgeneau, M. A. Kastner, Y. Endoh, S. Wakimoto, K. Yamada, R. W. Erwin, S.-H. Lee, and G. Shirane, Phy. Rev. B 60, 3643 (1999).

27. K. Yamada, C. H. Lee, K. Kurahashi, J. Wada, S. Wakimoto, S. Ueki, H. Kimura, Y. Endoh, S. Hosoya, G. Shirane, R. J. Birgeneau, M. Greven, M. A. Kastner, and Y. J. Kim, Phys. Rev. B 57, 6165 (1998).

28. S. Katano, M. Sato, K. Yamada, T. Suzuki, and T. Fukase, Phy. Rev. B 62, R14677 (2000).

29. B. Lake, K. Lefmann, N. B. Christensen, G. Aeppli, D. F. McMorrow, P. Vorderwisch, P. Smeibidl, N. Mangkorn-tong, T. Sasagawa, M. Nohara, H. Takagi, (unpublished).

30. Y. Zhang, E. Demler, and S. Sachdev, Phys. Rev. B 66, 094501 (2002).

31. D.-H. Lee, Phys. Rev. Lett. 88, 227003 (2002).

32. Y. Chen and C. S. Ting, Phys. Rev. B 65, 180513 (2002).

33. S. A. Kivelson, D.-H. Lee, E. Fradkin, and O. Oganesyan, Phys. Rev. B 66, 144516 (2002).

34. J. Zhu, I. Martin, and A. Bishop, Phys. Rev. Lett. 89, 067003 (2002).

35. B. Khaykovich, Y. S. Lee, R. W. Erwin, S.-H. Lee, S. Wakimoto, K. J. Thomas, M. A. Kastner, and R. J. Birgeneau, Phy. Rev. B 66, 014528 (2002).

36. B. Khaykovich, R. J. Birgeneau, F. C. Chou, R. E. Erwin, M. A. Kastner, S.-H. Lee, Y. S. Lee, P. Smeibidl, P. Vorderwisch, and S. Wakimoto, Phys. Rev. B 67, 054501 (2003).

37. R. I. Miller, R. F. Kiefl, J. H. Brewer, J. E. Sonier, J. Chakhalian, S. Dunsiger, G. D. Morris, A. N. Price, D. A. Bonn, W. H. Hardy, and R. Liang, Phys. Rev. Lett. 88, 137002 (2002).

38. V. F. Mitrovic, E. E. Sigmund, M. Eschrig, H. N. Bachman, W. P. Halperin, A. P. Reyes, P. Kuhns, and W. G. Moulton, Nature 413, 501 (2001).

39. V. F. Mitrovic, E. E. Sigmund, W. P. Halperin, A. P. Reyes, P. Kuhns, and W. G. Moulton, Phy. Rev. B 67, 220503(R) (2003).

40. Y. Hidaka and M. Suzuki, Nature (London) 338, 635 (1989).

41. P. Fournier, P. Mohanty, E. Maiser, S. Darzens, T. Venkatesan, C. J. Lobb, G. Czjzek, R. A. Webb, and R. L. Greene, Phys. Rev. Lett. 81, 4720 (1998).

42. Y. Wang, S. Ono, Y. Onose, G. Gu, Y. Ando, Y. Tokura, S. Uchida, and N. P. Ong, Science 299, 86 (2003).

43. Y. Tokura, H. Takagi, and S. Uchida, Nature 337, 345 (1989).

44. H. Takagi, S. Uchida, and Y. Tokura, Phys. Rev. Lett. 62, 1197 (1989).

45. J. S. Kim and D. R. Gaskell, Physica C 209, 381 (1993).

46. K. Kurahashi, H. Matsushita, M. Fujita, and K. Yamada, J. Phys. Soc. Jpn. 71, 910 (2002).

47. M. Fujita, T. Kubo, S. Kuroshima, T. Uefuji, K. Kawashima, K. Yamada, I. Watanabe, and K. Nagamine, Phys. Rev. B 67, 014514 (2003).

48. Y. Onose, Y. Taguchi, K. Ishizaka, and Y. Tokura, Phys. Rev. Lett. 87, 217001 (2001).

49. R. W. Hill, Cyril Proust, Louis Taillefer, P. Fournier, and R. L. Greene, Nature 414, 711 (2001).

50. S. Skanthakumar, J. W. Lynn, J. L. Peng, and Z. Y. Li, Phys. Rev. B 47, 6173 (1993).

51. D. Petitgrand, S. V. Maleyev, Ph. Bourges, and A. S. Ivanov, Phys. Rev. B 59, 1079 (1999).

52. R. Sachidanandam, T. Yildirim, A. B. Harris, Amnon Aharony and O. Entin-Wohlman Phys. Rev. B 56, 260 (1997).

53. S. Skanthakumar, H. Zhang, T. W. Clinton, W-H. Li, J. W. Lynn, Z. Fisk, and S-W. Cheong, Physica C 160, 124 (1989).

54. J.W. Lynn and S. Skanthakumar, in Handbook on the Physics and Chemistry of Rare Earths, edited by K. A. Gschneidner, Jr., L. Eyring, and M. B. Maple (Elsevier, Amsterdam 2001), Vol 31, p. 315.

55. S. Skanthakumar, J. W. Lynn, J. L. Peng, and Z. Y. Li, J. Appl. Phys. 73, 6326 (1993).

56. K. Yamada, K. Kurahashi, Y. Endoh, R. J. Birgeneau, and G. Shirane, J. Phys. Chem. Solids 60, 1025 (1999).

57. T. Uefuji, T. Kubo, K. Yamada, M. Fujita, K. Kurahashi, I. Watanabe, and K. Nagamine, Physica C 357-360, 208 (2001).

58. V. P. Plakhty, S. V. Maleyev, S. V. Gavrilov, F. Bourdarot, S. Pouget, and S. N. Barilo, Europhys. Lett., 61, 534 (2003).

59. K. Kurahashi, H. Matsushita, M. Fujita, and K. Yamada, J. Phys. Soc. Jpn. 71, 910 (2002).

60. P. K. Mang, S. Larochelle, and M. Greven, Nature 426, 139 (2003).

61. R. M. Moon, W. C. Koehler, H. R. Child, and L. J. Raubenheimer, Phys. Rev. 176, 722 (1968).

62. X. F. Sun, Y. Kurita, T. Suzuki, Seiki Komiya, and Yoichi Ando, Phys. Rev. Lett. 92, 047001 (2004).

63. Wu Jiang, J. L. Peng, Z. Y. Li, and R. L. Greene, Phys. Rev. B 47, 8151 (1993).

64. P. G. Radaelli, J. D. Jorgensen, A. J. Schultz, J. L. Peng, and R. L. Greene, Phys. Rev. B 49, 15322 (1994).

65. A. Nath, N. S. Kopelev, V. Chechersky, J. L. Peng, R. L. Greene, O. Boem-hoan, M. I. Larkin, and J. T. Markert, Science 265, 73 (1994).

66. G. Riou, P. Richard, S. Jandl, M. Poirier, P. Fournier, V. Nekvasil, S. N. Barilo, and L. A. Kurnevich, Phys. Rev. B 69, 024511 (2004).

67. P. Richard, G. Riou, I. Hetel, S. Jandl, M. Poirier, and P. Fournier, Phys. Rev. B 70, 064513 (2004).

68. I. W. Sumarlin, J. W. Lynn, T. Chattopadhyay, S. N. Sarilo, D. I. Zhigunov, and J. L. Peng, Phys. Rev. B 51, 5824 (1995).

69. P. K. Mang, S. Larochelle, A. Mehta, O. P. Vajk, A. S. Erickson, L. Lu, W. J. L. Buyers, A. F. Marshall, K. Prokes, and M. Greven, Phys. Rev. B 70, 094507 (2004).

70. A. N. Lavrov, H. J. Kang, Y. Kurita, T. Suzuki, Seiki Komiya, J. W. Lynn, S.-H. Lee, Pengcheng Dai, and Yoichi Ando, Phys. Rev. Lett. 92, 227003 (2004).

71. S. L. Li, S. D. Wilson, D. Mandrus, B. R. Zhao, Y. Onose, Y. Tokura, and Pengcheng Dai, Phys. Rev. B 71, 054505 (2005).

72. H. J. Kang, Pengcheng Dai, J. W. Lynn, M. Matsuura, J. R. Thompson, Shou-Cheng Zhang, D. N. Argyriou, Y. Onose, and Y. Tokura, Nature 423, 522 (2003).

73. M. Matsuura, Pengcheng Dai, H. J. Kang, J. W. Lynn, D. N. Argyriou, K. Prokes, Y. Onose, and Y. Tokura, Phys. Rev. B 68, 144503 (2003).

74. M. Matsuura, Pengcheng Dai, H. J. Kang, J. W. Lynn, D. N. Argyriou, Y. Onose, and Y. Tokura, Phys. Rev. B 69, 104510 (2004).

75. H. J. Kang, Pengcheng Dai, J. W. Lynn, M. Matsuura, J. R. Thompson, Shou-Cheng Zhang, D. N. Argyriou, Y. Onose, and Y. Tokura, Nature 426, 140 (2003).

76. M. Fujita, M. Matsuda, S. Katano, and K. Yamada, Phys. Rev. Lett. 93, 147003(2004).

77. Han-Dong Chen, Congjun Wu, and Shou-Cheng Zhang, Phys. Rev. Lett. 92, 107002 (2004).

78. B. Khaykovich, S. Wakimoto, R. J. Birgeneau, M. A. Kastner, Y. S. Lee, P. Smeibidl, P. Vorderwisch, and K. Yamada, cond-mat/0411355 (unpublished).

79. M. A. Kastner, R. J. Birgeneau, G. Shirane, and Y. Endoh, Rev. Mod. Phys. 70, 897 (1998).

80. Ch. Niedermayer, C. Bernhard, T. Blasius, A. Golnik, A. Moodenbaugh, and J. I. Budnick, Phys. Rev. Lett. 80, 3843 (1998).

81. A. N. Lavrov, Yoichi Ando, Seiki Komiya, and I. Tsukada, Phys. Rev. Lett. 87, 017007 (2001).

82. J.M. Tranquada, B. J. Sternlieb, J. D. Axe, Y. Nakamura, and S. Uchida, Nature 375, 561 (1995).

83. B. Keimer, A. Aharony, A. Auerbach, R. J. Birgeneau, A. Cassanho, Y. Endoh, R. W. Erwin, M. A. Kastner, and G. Shirane, Phys. Rev. B 45, 7430 (1992).

84. G.M. Luke, L. P. Le, B. J. Sternlieb, Y. J. Uemura, J. H. Brewer, R. Kadono, R. F. Kiefl, S. R. Kreitzman, and T. M. Riseman, C. E. Stronach, M. R. Davis, S. Uchida, H. Takagi, Y. Tokura, Y. Hidaka, T. Murakami, J. Gopalakrishnan, A. W. Sleight, M. A. Subramanian, E. A. Early, J. T. Markert, M. B. Maple, and C. L. Seaman, Phys. Rev. B 42, 7981 (1990).

85. K. Yamada, K. Kurahashi, T. Uefuji, M. Fujita, S. Park, S.-H. Lee, and Y. Endoh, Phys. Rev. Lett. 90, 137004 (2003).

86. T. Thio, T. R. Thurston, N. W. Preyer, P. J. Picone, M. A. Kastner, H. P. Jenssen, D. R. Gabbe, C. Y. Chen, R. J. Birgeneau, and Amnon Aharony, Phys. Rev. B 38, 905 (1988).

87. Y. Ando, A. N. Lavrov, and Seiki Komiya, Phys. Rev. Lett. 90, 247003 (2003).

88. Y. Ando, A. N. Lavrov, Seiki Komiya, Kouji Segawa, and X. F. Sun, Phys. Rev. Lett. 87, 017001 (2001).

89. A. N. Lavrov, Yoichi Ando, Kouji Segawa, and J. Takeya, Phys. Rev. Lett. 83, 1419 (1999).

90. V. P. Plakhty, A.B. Stratilatov, and S. Beloglazov, Solid State Commun. 103, 683 (1997).

91. D. Petigrand, A. S. Ivanov, and S. V. Maleyev, Appl. Phys. A 74, S853 (2002)

92. P. Fournier, M.-E. Gosselin, S. Savard, J. Renaud, I. Hetel, P. Richard and G. Riou, cond-mat/0309144

93. E. Demler and S. C. Zhang, Nature (London) 396, 733 (1998).

94. P. Dai, H. A. Mook, S. M. Hayden, G. Aeppli, T. G. Perring, R. D. Hunt, and F. Doğan, Science 284, 1344 (1999); P. Dai, H. A. Mook, G. Aeppli, S. M. Hayden, and F. Doğan, Nature (London) 406, 965 (2000).

95. For a review, see L. Pintschovius and W. Reichardt, in Neutron Scattering in Layered Copper-Oxide Superconductors, edited by A. Furrer, Physics and Chemistry of Materials with Low-Dimensional Structures Vol. 20 (Kluwer, Dordrecht, 1998), p. 165.

96. R. J. McQueeney, Y. Petrov, T. Egami, M. Yethiraj, G. Shirane, and Y. Endoh, Phys. Rev. Lett. 82, 628 (1999).

97. L. Pintschovius and M. Braden, Phys. Rev. B 60, R15 039 (1999).

98. H. A. Mook and F. Dog˘an, Nature (London) 401, 145 (1999).

99. Z.-X. Shen, A. Lanzara, S. Ishihara, and N. Nagaosa, cond-mat/0108381 (unpublished).

100. T. Valla, A. V. Fedorov, P. D. Johnson, and S. L. Hulbert, Phys. Rev. Lett. 83, 2085 (1999).

101. P. V. Bogdanov, A. Lanzara, S. A. Kellar, X. J. Zhou, E. D. Lu, W. J. Zheng, G. Gu, J.-I. Shimoyama, K. Kishio, H. Ikeda, R. Yoshizaki, Z. Hussain, and Z. X. Shen, Phys. Rev. Lett. 85, 2581 (2000).

102. A. Kaminski, M. Randeria, J. C. Campuzano, M. R. Norman, H. Fretwell, J. Mesot, T. Sato, T. Takahashi, and K. Kadowaki, Phys. Rev. Lett. 86, 1070 (2001).

103. P. D. Johnson, T. Valla, A. V. Fedorov, Z. Yusof, B. O. Wells, Q. 064506-4 Li, A. R. Moodenbaugh, G. D. Gu, N. Koshizuka, C. Kendziora, Sha Jian, and D. G. Hinks, Phys. Rev. Lett. 87, 177007 (2001).

104. While the doping concentrations for the MIT and nonsuperconducting-superconducting transition (NST) in LSCO are assumed to be the same ($x \approx 0.05 \sim 0.06$) in Ref. 8 recent results [Y. Ando, A. N. Lavrov, S. Komiya, K. Segawa, and X. F. Sun, Phys. Rev. Lett. 87, 017001 (2001)] suggested that the MIT in LSCO occurs at a lower x. Since the doping level for MIT is not conclusively established for any cuprates, we associate the observed phonon anomalies in LSCO with the doping-induced NST, not with the doping induced MIT.

105. M. R. Norman, H. Ding, J. C. Campuzano, T. Takeuchi, M. Randeria, T. Yokoya, T. Takahashi, T. Mochiku, and K. Kadowaki, Phys. Rev. Lett. 79, 3506 (1997).

106. J.W. Lynn, I.W. Sumarlin, D. A. Neumann, J. J. Rush, J. L. Peng, and Z. Y. Li, Phys. Rev. Lett. 66, 919 (1991).

107. I. W. Sumarlin, J. W. Lynn, D. A. Neumann, J. J. Rush, C.-K. Loong, J. L. Peng, and Z. Y. Li, Phys. Rev. B 48, 473 (1993).

108. Y. Tokura, H. Takagi, and S. Uchida, Nature (London) 337, 345 (1989); H. Takagi, S. Uchida, and Y. Tokura, Phys. Rev. Lett. 62, 1197 (1989).

109. C. C. Almasan and M. B. Maple, in Chemistry of High Temperature Superconductors, edited by C. N. R. Rao ~World Scientific, Singapore, (1991), p. 205.

110. A. T. Boothroyd, S. M. Doyle, D. Paul, and R. Osborn, Phys. Rev. B 45, 10 075 (1992).

111. L. Pintschovius, N. Pyka, W. Reichardt, A. Yu. Rumiantsev, N. L. Mitrofanov, A. S. Ivanov, G. Collin, and P. Bourges, Physica B 174, 323 (1991).

112. M. d'Astuto, P. K. Mang, P. Giura, A. Shukla, P. Ghigna, A. Mirone, M. Braden, M. Greven, M. Krisch, and F. Sette, Phys. Rev. Lett. 88, 167002 (2002).

113. N. P. Armitage, F. Ronning, D. H. Lu, C. Kim, A. Damascelli, K. M. Shen, D. L. Feng, H. Eisaki, Z.-X. Shen, P. K. Meng, N. Kaneko, M. Greven, Y. Onose, Y. Taguchi, and Y. Tokura, Phys. Rev. Lett. 88, 257001 (2002).

Vita

Hye Jung Kang was born in Chinju, Korea on April 1, 1970. She went to Gyeongsang National University, Korea and received a B.S. in physics in 1993 and a M.S. in physics in 1995. She taught physics for 4 years in Gyeongsang National University, Korea. She enrolled in graduate program in physics at the University of Tennessee, Knoxville in August 1999 and received the Doctor of Philosophy in Physics in May 2005.